Transport and Coherent Backscattering of Bose-Einstein Condensates in Mesoscopic Systems

Dissertation

zur Erlangung des Doktorgrades
der Naturwissenschaften (Dr. rer. nat.)
der Naturwissenschaftlichen Fakultät II - Physik
der Universität Regensburg

vorgelegt von

Michael Hartung

aus Regenstauf

2009

Das Promotionsgesuch wurde am 15. Januar 2009 eingereicht.
Das Promotionskolloquium fand am 13. März 2009 statt.

Die Arbeit wurde von PD Dr. Peter Schlagheck angeleitet.

Prüfungsausschuß:

Vorsitzender:	Prof. Dr. Christian Schüller
1. Gutachter:	PD Dr. Peter Schlagheck
2. Gutachter:	Prof. Dr. Matthias Brack
Weiterer Prüfer:	Prof. Dr. Andreas Schäfer

Contents

CHAPTER 1

Introduction

The foundation for the realization of a Bose-Einstein condensate has been set already in 1924 by S. N. Bose and A. Einstein with the description of the *Bose-Einstein statistics* [1–3] which determines that a single particle quantum state can be occupied by an arbitrary number of identical particles with the corresponding particles being called *bosons*. This is in contrast to fermions which obey the Pauli exclusion principles, such that two identical particles cannot occupy the same quantum state. Later it was realized that particles with half-integer spin are fermions and particles with integer spin obey Bose-Einstein statistics. Albert Einstein recognized that an ensemble of identical bosons can experience a phase transition, the *Bose-Einstein condensation*, where the energetically lowest single quantum state is occupied macroscopically. This phase transition describes a crossover from a thermal ensemble of particles to a quantum gas with long range coherence which takes place at the critical temperature. This critical temperate for atomic vapors is understood in terms of the de Broglie wave length, which arises due to the particle-wave duality associated with matter. The condensate is formed as soon as the temperature is reduced such that the mean particle distance in the dilute gas is comparable to de Broglie wave length of the atoms, and the waves of the single atoms start to overlap. In this case a macroscopic wave function emerges which takes the role of an order parameter of the condensate. This new state of the matter has triggered many scientific projects and opened a new fascinating field. Furthermore, it allows to address fundamental quantum mechanical questions.

On the way towards the experimental realization of a Bose-Einstein condensate many experimental difficulties had to be overcome. One important step was the demonstration of laser cooling [4], where the thermal motion of neutral atoms is reduced by employing the Doppler shift with a laser beam near an atomic resonance. But also techniques like evaporative cooling and magneto-optical traps [5] were developed. Nowadays temperatures even in the nano-Kelvin regime can be obtained. Therefore, it

took until 1995 for the first realization of a Bose-Einstein condensate in a dilute atomic vapor in ^{87}Rb and ^{23}Na [6, 7] and in condensates with weak attractive interactions – compared to weak repulsive ones before – in ^{7}Li [8]. The direct observation of a matter wave with imaging techniques was possible for the first time due to the macroscopic size of the condensate. The large number of atoms and the long coherence length of the condensate makes the Bose-Einstein condensate a versatile tool to study matter wave phenomena. After the first observation of a condensate the field exploded, and many groups are now involved with research on the properties of Bose-Einstein condensates.

The high accuracy and high flexibility in the control of parameters in the experiments with Bose-Einstein condensates allow to study new phenomena, but also to address open questions, which have originally occurred in a different context. For example, it is possible to mimic condensed matter physics [9] with an optical periodic lattice which is created by a standing wave formed by counter propagating laser beams in all three spatial directions. Such an optical lattice has no defects or dislocations, which are encountered in the solid state context. This setup makes it for example possible to study the transition between the Mott insulator state and the superfluid state [10]. In the Mott insulating state each atom is confined to a potential minimum for a large laser intensity, whereas for a shallow potential a phase coherent wave function extends over the whole lattice. This transition is clearly observed in the momentum distribution, which can be measured after a free expansion of the condensate with absorption imaging. The analogy to condensed matter can be extended by the usage of ultra cold Fermi gases [11, 12], which allows to explore the BEC-BCS crossover [13], where the bosons are molecules consisting of two bound fermionic atoms. Of importance in this context is a Feshbach resonance [14], which is mediated via a molecular bound state, and allows to tune the s-wave scattering length, even from positive to negative, just by changing the external magnetic field. This provides a powerful tool to study interaction effects in these dilute gases, where the interaction strength is proportional to the s-wave scattering length. Such effects induced by interaction can also be studied in transport properties. The transport process can be realized with experimental setups which create a continuous flow of Bose-Einstein condensates, like atom-lasers [15–17]. Another experimental technique to investigate transport physics are so-called *atom chips* [18], where the magnetic field, which arises from wires on a micro-fabricated chip forms a waveguide for the atoms. With this chip technology transport through arbitrary formed potentials can be studied [19, 20]. In such a quasi one-dimensional waveguide above a microchip fragmentation of the Bose-Einstein condensate was observed, which was then explained by inhomogeneities in the wire resulting in a disorder potential for the condensate [19, 21–23].

The observation of fragmentation enhanced the investigation in Anderson localization in the community of Bose-Einstein condensates. In 1958 P. W. Anderson showed that diffusion is totally suppressed in some disorder potential [24, 25]. The unambigu-

ous experimental identification of Anderson localization is quite difficult. For example in solid state systems the electron-electron interaction modifies the localization effect. After several attempts [26–28] it was possible just recently, namely in 2008, to demonstrate the Anderson scenario with Bose-Einstein condensates [29, 30] experimentally. In one experiment a speckle disorder potential was employed, which is created by illuminating a diffusive plate with a laser [29, 31] and in the other one a bichromatic disorder lattice [30] was used, where in both cases the potential is controlled very well. Theoretical studies concentrated on the expansion process [32] of the condensate as well as on the scattering perspective [19, 20]. Complementary studies were focused on localization properties of Bogoliubov quasi-particles [33, 34], on dipole oscillations in presence of disorder [35, 36], as well as on the realization of Bose glass phases [37, 38].

The phenomenon of Anderson localization is addressed as well in optical disordered systems, with a controversial discussion about the unambiguous signatures [39–41], and the experimental research is still in progress [41–43]. Already in the regime of weak localization the phenomenon of coherent backscattering is observed [44–46]. It was shown in 1985 independently by M. van Albada and A. Lagendijk [44], and also by P. Wolf and G. Maret [45] that by illuminating a random media with a phase coherent laser beam, an increase of the angular resolved back-scattered intensity is observed by a factor of two in exactly backward direction. This arises due to the constructive interference of time reversed scattering paths. This effect is found in astrophysics [47–49] and in acoustic systems [50, 51] as well. Recently coherent backscattering with light scattering in a cloud of cold atoms was studied [52–55]. They were thought as good candidates to explore multiple scattering effects also in the strongly localized regime, since resonant scattering of identical particles can be exploited to increase the scattering cross section. Furthermore cold atoms allow to investigate nonlinear scattering effects due to the saturation of the intra-atomic transition, where the nonlinear systems are still an open and interesting field. But in the experiments with cold atoms complexity is added due inelastic scattering [56–58], thermal motion [52] and polarization phenomena [55].

In this work we introduce the phenomenon of coherent backscattering to matter waves, especially to a Bose-Einstein condensate scattering in a disorder potential, which can be created by optical means and is very well controlled. In particular we include nonlinear effects based on the Gross-Pitaevskii equation in our description, which arise due to the atom-atom interaction in the condensate. As already mentioned earlier, the interaction strength can be tuned via Feshbach resonances with an external magnetic field, which allows for controlled experimental research on nonlinear effects. Our setup should provide a clean situation, since the coherence of the atomic wave function in the mean-field regime is well preserved in the presence of the nonlinearity compared to scattering with light from cold atoms [53], as explained above, at least for very low temperatures where depletion can be neglected. We show that the interaction effects

give rise to substantial modifications of the coherent backscattering scenario.

Outline of the thesis

- In CHAPTER 2 we explain the basic concepts of this thesis. We begin with a derivation of the Gross-Pitaevskii equation from the many-body Hamiltonian, where the condensate wave function arises from the macroscopic occupation of the single particle ground state. We are especially interested in the coherent transport through a quasi two-dimensional system and deduce the corresponding effective Gross-Pitaevskii equation in reduced dimensions to describe time-dependent dynamics. Then we describe the principles to apply mesoscopic potentials to the atoms with optical and magnetic fields.

- The methods to solve the two-dimensional Gross-Pitaevskii equation are explained in CHAPTER 3. We show an approach to simulate an open system numerically in order to describe the scattering approach. This can be obtained by including a source term in the Gross-Pitaevskii equation and by introducing absorbing boundary conditions, which are especially capable to absorb two-dimensional waves. At the end we apply the numerical apparatus to a multi-slit potential, and also to a quasi one-dimensional double barrier potential. In the latter case we compare the scattering approach to decaying quasi-bound states.

- The linear transport in two-dimensional disorder potentials is the topic of CHAPTER 4. We describe correlated disorder potentials with a Gaussian correlation function and speckle disorder potentials. We give an analytical derivation of the scattering mean free path and the transport mean free path in Boltzmann approximation but also with weak localization corrections. We relate those mean free paths with our numerical simulations and find, depending on the parameters, agreement or deviations which we discuss.

- CHAPTER 5 is devoted to coherent backscattering. First we explain the fundamental ideas and then the applicability to Bose-Einstein condensates. We include the atom-atom interaction on the mean-field level and show with our numerical approach that the scenario of coherent backscattering is substantially modified. Then we present a diagrammatic approach to nonlinear coherent backscattering, which was developed very recently [59], compare it with our results and give further details. For intermediate strength of the nonlinearity we find time-dependent behavior. Finally, we study the statistical properties of the intensity distribution.

- In CHAPTER 6 we give a summary of the main results in this thesis in form of a short overview. Additionally we discuss questions which can be addressed on the basis of this thesis.

CHAPTER 2

Basic concepts

2.1 Mean-field theory for condensates

This section is devoted to the derivation of the mean-field description of Bose-Einstein condensates, which leads to the Gross-Pitaevskii equation. Here we especially concentrate on a potential geometry, which effectively restricts the Bose-Einstein condensate to two dimensions. In this derivation of the Gross-Pitaevskii equation we mainly follow Ref. [60] and also the text books [61, 62]. To this end we start with the many-body Hamiltonian for N interacting bosons in an external potential $V(\mathbf{r})$:

$$\begin{aligned}\hat{H} &= \int d\mathbf{r}\ \hat{\Psi}(\mathbf{r})\left[-\frac{\hbar^2}{2m}\nabla^2 + V(\mathbf{r})\right]\hat{\Psi}(\mathbf{r}) \\ &\quad + \frac{1}{2}\int d\mathbf{r}d\mathbf{r}'\ \hat{\Psi}^\dagger(\mathbf{r})\hat{\Psi}^\dagger(\mathbf{r}')U(\mathbf{r}-\mathbf{r}')\hat{\Psi}(\mathbf{r}')\hat{\Psi}(\mathbf{r})\end{aligned} \tag{2.1}$$

The bosonic field operators $\hat{\Psi}^\dagger(\mathbf{r})$ and $\hat{\Psi}(\mathbf{r})$ create and annihilate a particle at position $\mathbf{r}$. $U(\mathbf{r}-\mathbf{r}')$ is the two-body inter-particle potential. In the remaining part of this work we consider a dilute gas of bosonic atoms, which allows us to neglect three-body or many-body collisions. We apply the following ansatz, where the field operator can be written in terms of single particle wave functions Ψ_α:

$$\hat{\Psi}(\mathbf{r}) = \sum_\alpha \Psi_\alpha(\mathbf{r})a_\alpha \tag{2.2}$$

Here $a^\dagger$ and a are bosonic creation and annihilation operators, which satisfy the following relations in Fock-space:

$$a_\alpha^\dagger \, |n_0, n_1, \ldots, n_\alpha, \ldots\rangle = \sqrt{n_\alpha + 1} \, |n_0, n_1, \ldots, n_\alpha + 1, \ldots\rangle, \tag{2.3}$$

$$a_\alpha \, |n_0, n_1, \ldots, n_\alpha, \ldots\rangle = \sqrt{n_\alpha} \, |n_0, n_1, \ldots, n_\alpha - 1, \ldots\rangle \, , \tag{2.4}$$

where n_α are the occupation numbers of atoms in the single particle states α, and therefore the eigenvalues of the number operator $\hat{n}_\alpha = a_\alpha^\dagger a_\alpha$. The creation and annihilation operators $a^\dagger$ and a fulfill the bosonic commutation relations

$$[a_\alpha, a_\beta^\dagger] = \delta_{\alpha,\beta}, \quad [a_\alpha, a_\beta] = 0, \quad [a_\alpha^\dagger, a_\beta^\dagger] = 0. \tag{2.5}$$

The key characteristic for Bose-Einstein condensation is that the ground state is macroscopically populated. The occupation number N_0 of the single particle ground state gets very large and especially in the thermodynamic limit $N \to \infty$ the ratio N/N_0 remains finite. In this limit the states with to N_0 and $N_0 + 1 \simeq N_0$ correspond to the same physical configuration and therefore the creation and annihilation operators of the ground state can be treated as complex numbers $a_0^\dagger = a_0 = \sqrt{N_0}$ [1]. Consequently we can write for the field operator $\hat{\Psi}(\mathbf{r})$ in the case of a homogeneous Bose-Einstein condensate in a potential V:

$$\hat{\Psi}(\mathbf{r}) = \sqrt{N_0/V} + \hat{\Psi}'(\mathbf{r}). \tag{2.6}$$

The first term on the right hand side corresponds to the macroscopically populated ground state with zero momentum and the perturbation $\hat{\Psi}'(\mathbf{r})$. A theory for these excitations for interacting Bose-Einstein condensates was developed by Bogoliubov [62]. The above ansatz can be generalized to the nonuniform and time-dependent case:

$$\hat{\Psi}(\mathbf{r}, t) = \Phi(\mathbf{r}, t) + \hat{\Psi}'(\mathbf{r}, t). \tag{2.7}$$

Here $\Phi(\mathbf{r}, t)$ is a complex wave function that is defined as the expectation value of the field operator $\Phi(\mathbf{r}, t) = \langle \Psi(\mathbf{r}, t) \rangle$. Hence the density $n_0(\mathbf{r}, t)$ of the condensate is given by the modulus squared of the *wave function of the condensate*:

$$n_0(\mathbf{r}, t) = |\Phi(\mathbf{r}, t)|^2. \tag{2.8}$$

This condensate wave function has also a well defined phase, and is a classical field, which is interpreted as the order parameter of the condensate. Now we want to derive

[1] See Y. Castin and R. Dum [63] for a derivation of the Gross-Pitaevskii equation with a well-defined number of particles.

the time evolution for this order parameter. To this end we write down the Heisenberg equation for the many-body Hamiltonian:

$$\begin{aligned} i\hbar\frac{\partial}{\partial t}\hat{\Psi}(\mathbf{r},t) &= [\hat{\Psi},\hat{H}] \\ &= \left[-\frac{\hbar^2\nabla^2}{2m}+V(\mathbf{r})+\int d\mathbf{r}'\ \hat{\Psi}^\dagger(\mathbf{r}',t)U(\mathbf{r}'-\mathbf{r})\hat{\Psi}(\mathbf{r}',t)\right]\hat{\Psi}(\mathbf{r},t)\ . \end{aligned} \tag{2.9}$$

We continue with approximating the two-body interaction potential with a delta function. This is a good approximation for low densities, where the inter-particle distance is much larger than the range of the binary collision potential. An additional constraint arising from this approximation is the low temperature limit, because at low energies only the s-wave scattering is effective. We can therefore write

$$V(\mathbf{r}'-\mathbf{r}) = U_0\delta(\mathbf{r}'-\mathbf{r})\ , \tag{2.10}$$

where U_0 is the effective interaction strength characterized by the s-wave scattering length a_s:

$$U_0 = \frac{4\pi\hbar^2 a_s}{m}. \tag{2.11}$$

With this simplifications we arrive at the *Gross-Pitaevskii equation* for the condensate wave function:

$$\left(-\frac{\hbar^2}{2m}\nabla^2+V(\mathbf{r})+U_0|\Phi(\mathbf{r},t)|^2\right)\Phi(\mathbf{r},t) = i\hbar\frac{\partial}{\partial t}\Phi(\mathbf{r},t). \tag{2.12}$$

This Gross-Pitaevskii equation allows us to describe the macroscopic behavior of a system, especially the time-dependent and non-uniform behavior. This is only valid where the s-wave scattering is a good approximation, namely in the low density limit, and additionally in the regime of low temperatures, much below the critical temperature, in order to neglect the thermal cloud of atoms.

Gross-Pitaevskii equation in two dimensions

In the following we consider a Bose-Einstein condensate which is effectively confined to two dimensions. We assume a potential in the z-direction which can be created for example by optical means (see next section), and which restricts the dynamics to a two-dimensional plane. To this end we derive an effective two-dimensional Gross-Pitaevskii equation. This description is valid in the mean-field regime which is characterized by $a_s^3 n_{3D} \ll 1$ [64], where n_{3D} and in the following n_{2D} is the density in three or two

dimensions, respectively. The condition for the validity of the mean-field description translates to two dimension as follows:

$$n_{2D} a_s^2 \ll \frac{a_\perp}{a_s} \,, \tag{2.13}$$

where $a_\perp$ characterizes the transversal width of the confinement. We especially focus on those potentials in the two-dimensional plane, which vary slow on the length scale of the transverse confinement. This allows us to suppose that in the transverse direction the ground state is realized, and that this ground state adjusts to the adiabatic potential variations. The derivation is analog to Ref. [65] for one-dimensional waveguides. The starting point for this derivation is the Gross-Pitaevskii equation in three dimensions:

$$\left(-\frac{\hbar^2}{2m}\nabla^2 + V(\mathbf{r}) + U_0 |\Phi(\mathbf{r},t)|^2 \right) \Phi(\mathbf{r},t) = i\hbar \frac{\partial}{\partial t} \Phi(\mathbf{r},t). \tag{2.14}$$

We consider now a Bose-Einstein condensate which propagates in this two-dimensional waveguide and define the in transverse direction integrated density:

$$n(x,y,t) = \int dz \, |\Phi(x,y,z,t)|^2. \tag{2.15}$$

Below we assume that the dynamics in transverse direction is much faster than in the xy-plane. This leads to the limit of adiabatic wave dynamics and justifies the following ansatz:

$$\Phi(\mathbf{r},t) = \psi(x,y,t)\ \phi(z, n(x,y,t)). \tag{2.16}$$

Here $\psi(x,y,t)$ is the wave function in the two-dimensional plane, and $\phi(z,n)$ is the transverse ground state. Note that $\phi(z,n)$ depends on the time and on the coordinates in the plane due to the density n. We impose the following normalization condition onto the transverse wave function:

$$\int dz \, |\phi(z,n)|^2 = 1. \tag{2.17}$$

This also implies that the in plane density is given by $n(x,y,t) = |\psi(x,y,t)|^2$. The adiabatic regime is described by the following conditions:

$$\frac{\partial}{\partial t}\phi \simeq 0, \qquad \frac{\partial}{\partial x}\phi \simeq 0, \qquad \frac{\partial}{\partial y}\phi \simeq 0 \,. \tag{2.18}$$

We implement these conditions using an adiabatic potential, which means that $V(x,y,z)$ changes only slowly in the xy-plane on the length scale $a_\perp$, which characterizes the width of the waveguide in z-direction. Here we consider especially a potential of the form:

$$V(x,y,z) = V_\parallel(x,y) + V_\perp(z;x,y) \,, \tag{2.19}$$

where the confining potential $V_\perp(z;x,y)$ depends only in a parametric way on x and y. Now we insert the ansatz Eq. 2.16 into the Gross-Pitaevskii equation Eq. 2.14 and find:

$$i\hbar\phi\,\frac{\partial}{\partial t}\psi(x,y) = -\frac{\hbar^2}{2m}\phi\left(\frac{\partial^2}{\partial x^2}+\frac{\partial^2}{\partial y^2}+V_\perp\right)\psi + \psi\left[-\frac{\hbar^2}{2m}\frac{\partial^2}{\partial z^2}+V_\parallel+U_0|\psi|^2|\phi|^2\right]\phi. \tag{2.20}$$

Here we identify the term in the square brackets as the effective Hamiltonian in the transverse z-direction. Of course a Hamilton operator has to be linear, but we interpret the term $U_0|\psi|^2|\phi|^2$ as an effective potential, and we use the term 'effective Hamilton operator' instead. Since we assume the transverse wave function to be an eigenstate, we can write:

$$\epsilon(n(x,y,t))\,\phi = \left[-\frac{\hbar^2}{2m}\frac{\partial^2}{\partial z^2}+V_\perp(z;x,y)+U_0 n(x,y,t)|\phi|\right]\phi. \tag{2.21}$$

The eigenenergy ϵ depends due to the density n on the coordinates on the xy-plane.

For the wave equation in the xy-plane we arrive at:

$$i\hbar\frac{\partial}{\partial t}\psi(x,y) = \left[-\frac{\hbar^2}{2m}\left(\frac{\partial^2}{\partial x^2}+\frac{\partial^2}{\partial y^2}\right)+V_\parallel(x,y)+\epsilon(n(x,y,t))\right]\psi(x,y). \tag{2.22}$$

This is just the final result for the effective Gross-Pitaevskii equation reduced to two dimensions, where we assumed an adiabatic potential, which means that V changes only slowly on length scales compared to the transverse width $a_\perp$ of the confinement. Furthermore we assumed that the transverse wave function is in the ground state.

Harmonic confinement in transverse direction

In the following we restrict to an harmonic potential confining in transverse direction. In this case we can derive analytical expressions for the transverse energy $\epsilon(n)$ in the limit of low densities and in the high density limit (Thomas-Fermi regime). Additionally we give an analytical formula which interpolates between both regimes. Finally we show that plane waves are solutions to the two-dimensional Gross-Pitaevskii equation in the low density limit with a modified dispersion relation.
Consequently we consider a harmonic potential in z-direction:

$$V_\perp(z;x,y) = \frac{1}{2}m\,\omega_\perp^2(x,y)\,z^2. \tag{2.23}$$

Here we allow for an explicit dependence of the harmonic oscillator frequency $\omega_\perp(x,y)$ on x and y.

We start with the discussion of the transverse ground state energy in the perturbative limit which is characterized by the condition $na_s a_\perp \ll 1$ (see Eq. 2.25 below). For vanishing atom-atom interaction strength the Gaussian profile of the wave function in the harmonic oscillator looks like:

$$\phi_0(z) = (\sqrt{\pi}a_\perp)^{-1/2}\, \mathrm{e}^{-z^2/2a_\perp^2}\ , \tag{2.24}$$

where $a_\perp = \sqrt{\hbar/m\omega_\perp}$ is the harmonic oscillator length. The first order correction to the ground state energy is then calculated to

$$\begin{aligned} \epsilon(n) &= \frac{1}{2}\hbar\omega + U_0 n\langle\phi|\ |\phi|^2\ |\phi\rangle = \frac{1}{2}\hbar\omega + \frac{\hbar^2}{2m}4\sqrt{2\pi}\frac{a_s}{a_\perp}n \\ &= \frac{1}{2}\hbar\omega + \hbar\omega 2\sqrt{2\pi}na_s a_\perp\ , \end{aligned} \tag{2.25}$$

where we used the definition of Eq. 2.11 of the s-wave scattering length:

$$U_0 = 4\pi\hbar^2 a_s/m. \tag{2.26}$$

In the opposite limit, i.e. for high densities $na_s a_\perp \gg 1$ we can use the Thomas-Fermi approximation [60] to find an analytical expression for the ground state energy $\epsilon(n)$. To this end we neglect the kinetic energy in comparison to the potential energy and the interaction energy. In this limit the condensate wave function in z-direction can be written in the following way:

$$\phi_{TF}(z) = \frac{1}{\sqrt{U_0 n}}\ \sqrt{\epsilon(n) - V_\perp(z)}\ \ \Theta(\epsilon(n) - V_\perp(z)). \tag{2.27}$$

The ground state energy in the Thomas-Fermi approximation is as follows:

$$\epsilon_{TF}(n) = \frac{1}{2}\hbar\omega(6\pi na_s a_\perp)^{2/3}. \tag{2.28}$$

The expression below for the ground state energy $\epsilon(n)$ can be used to interpolate between the perturbative limit Eq. 2.25 and the Thomas-Fermi regime Eq. 2.28. It reduces to Eq. 2.25 in the small density limit and to Eq. 2.28 in the high density limit ($na_s a_\perp \gg 1$) :

$$\epsilon(n) = \frac{1}{2}\hbar\omega\left(1 + 12\sqrt{2\pi}(na_s a_\perp) + 36\pi^2(na_s a_\perp)^2\right)^{1/3}. \tag{2.29}$$

Finally we have reached an effective Gross-Pitaevskii equation for a system which is confined to two dimensions. In the third direction we assumed a harmonic confinement. Additionally we derived analytical expressions for the transverse ground state energy in the low and the high density regime, and also an interpolation formula between these

two regimes.
In the next lines we want to figure out that plane waves are solutions to the Gross-Pitaevskii equation :

Now we consider the perturbative limit ($na_s a_\perp \ll 1$). Furthermore we assume a constant potential. In this case the Gross-Pitaevskii equation for quasi two dimensions is given by:

$$i\hbar\frac{\partial}{\partial t}\psi(x,y,t) = \left[-\frac{\hbar^2}{2m}\left(\frac{\partial^2}{\partial x^2}+\frac{\partial^2}{\partial y^2}\right)+\frac{1}{2}\hbar\omega_\perp+\frac{\hbar^2}{2m}g|\psi|^2\right]\psi(x,y,t)\ , \tag{2.30}$$

where we define the dimensionless interaction strength $g = 4\sqrt{2\pi}a_s/a_\perp$. Now we use the ansatz

$$\psi(x,y,t) = \sqrt{n}\ \mathrm{e}^{i(k_x x+k_y y)-i\mu t/\hbar}, \tag{2.31}$$

and we see that plane waves are solutions to this Gross-Pitaevskii equation but with a modified dispersion relation:

$$\mu = \frac{\hbar^2}{2m}\left(|\mathbf{k}|^2+gn\right)+\frac{1}{2}\hbar\omega_\perp. \tag{2.32}$$

In the following we neglect this constant potential offset $\hbar\omega_\perp/2$ since it can be absorbed by a redefinition of the chemical potential.

2.2 Optical and magnetic potentials

In this section we want to describe methods to create traps for condensates. A potential that acts on neutral atoms has to be applied. In the following two techniques which base on two different physical effects are presented: First we present a potential caused by applying an optical field where the Stark effect is the underlying mechanism and then we present a second possibility, by applying a magnetic field which takes advantage from the Zeeman effect.

Optical potentials

In the context of Bose-Einstein condensates optical potentials are very often used, since they allow to create a rich variety of potential landscapes. The interaction between the light field and the atom is described in the dipole approximation with the following Hamilton operator:

$$H = -\hat{\mathbf{d}}\cdot\boldsymbol{\mathcal{E}}. \tag{2.33}$$

The expectation value of the dipole operator is proportional to the electrical field:

$$\langle \hat{\mathbf{d}} \rangle = \alpha \, \boldsymbol{\mathcal{E}} \, , \tag{2.34}$$

where we introduced the polarizability α of the atom. We consider now an atom in an oscillating laser field $\boldsymbol{\mathcal{E}}(t) = \boldsymbol{\mathcal{E}}_0 \cos(\omega t)$. Initially the atom is in the ground state $|g\rangle$, and can be excited to the states $|e\rangle$. In this case the polarizability α depends on the laser frequency and is given by [61]:

$$\alpha(\omega) = \sum_e |\langle e|\hat{\mathbf{d}} \cdot \boldsymbol{\mathcal{E}}/\mathcal{E}_0|g\rangle|^2 \left(\frac{1}{E_e - E_g + \hbar\omega} + \frac{1}{E_e - E_g - \hbar\omega} \right). \tag{2.35}$$

In the particular situation where the laser frequency ω is close to the resonance frequency $\omega_L = (E_{\tilde{e}} - E_g)/\hbar$ between the ground state $|g\rangle$ and the excited state $|\tilde{e}\rangle$ the contribution from this transition is dominant and the polarizability can be approximated to:

$$\alpha(\omega) \approx \frac{|\langle \tilde{e}|\hat{\mathbf{d}} \cdot \boldsymbol{\mathcal{E}}/\mathcal{E}_0|g\rangle|^2}{\hbar\omega_L - \hbar\omega} \, . \tag{2.36}$$

Now we can combine Eq. 2.33 and Eq. 2.34 and find for the energy shift in the atom due to the external applied oscillating laser field:

$$\Delta V(\mathbf{r}) = -\frac{1}{2} \, \alpha(\omega) \, \langle \boldsymbol{\mathcal{E}}^2(\mathbf{r}, t) \rangle_t . \tag{2.37}$$

Note that this energy shift of the atom depends on the intensity, and since this intensity can be position dependent the laser field effectively introduces a potential landscape for the atoms. In this way lasers can be used to model potential geometries.

From Eq. 2.36 and Eq. 2.37 we see that the sign of the potential depends on the laser frequency ω in comparison to the resonance frequency ω_L, since the polarizability changes the sign at the resonance frequency ω_L. In the case of a red detuned laser beam, that means $\omega < \omega_L$, the maxima of the intensity correspond to potential minima. Here the atoms are trapped in regions with high laser intensity. In the opposite case of a blue detuned laser beam, i. e. $\omega > \omega_L$, the maxima of the intensity correspond to potential maxima.

A red detuned laser beam was e. g. used to create a one-dimensional waveguide for a Bose-Einstein condensate [15]. There a laser was focussed to form a narrow tube. Due to the dipole forces the atoms were trapped in the center of the laser beam at the maximum of the laser intensity.

Another potential geometry can be realized with two counter propagating laser beams. Those form a stationary standing wave, which results in a lattice potential.

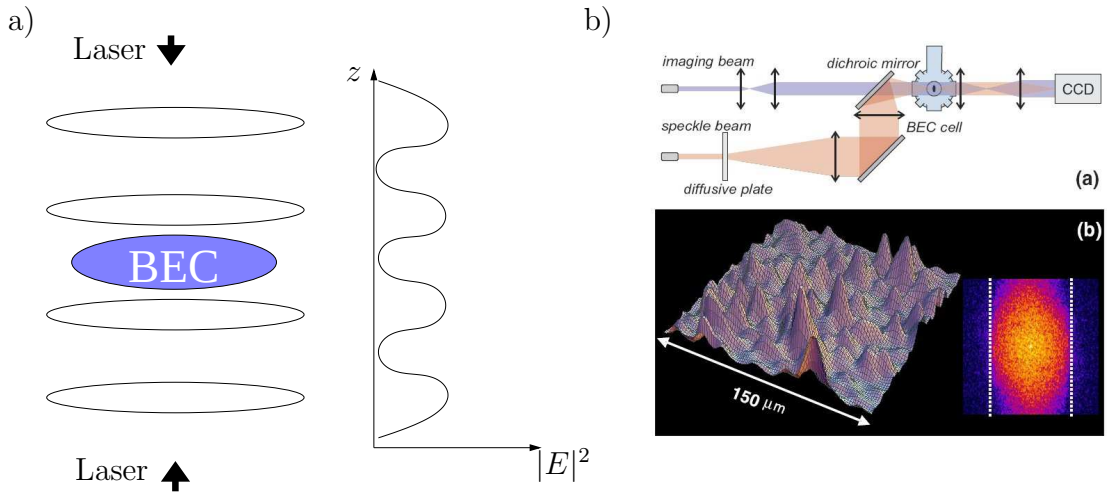

Figure 2.1: a) A two-dimensional confinement potential for a condensate can be realized with an optical lattice potential in z-direction. This is created with two counter propagating laser beams. b) Optical setup as it is used in the experiment by J. E. Lye et al. to realize a disorder potential by optical means. A laser illuminates a diffusive plate. The resulting interference pattern is then imaged onto the region of the condensate. The lower left figure shows the speckle potential in real space and its Fourier transform in the lower right figure. (The picture is taken from Lye et al. [31].)

With this setup atoms can be confined to a two-dimensional plane for high enough laser intensity. This setup is sketched in Fig. 2.1 a.

A disorder potential for Bose-Einstein condensates can be created by illuminating a diffusive plate with a laser. The resulting speckle pattern is then imaged to the experimental region, which introduces a disorder potential to the condensate wave function [31]. Here the correlation length of the speckle pattern and the intensity is well known. This method allows to create disorder in a controlled manner in contrast to other systems, where the disorder is not known a priory. This experimental setup is shown in Fig. 2.1 b. Another experimental technique we mention here allows to confine atoms with acoustooptic deflectors with a fast moving blue detuned laser beam to an arbitrary potential geometry like billiard boundaries [66]. The periodic deflection of the laser beam along an arbitrary path is much faster than the typical velocities of the atoms. Therefore the atoms experience effectively a static potential.

Magnetic potentials

Neutral atoms with a magnetic moment μ_b can be trapped with magnetic fields. The energy shift due to the Zeeman effect, which is in good approximation linear in the

Figure 2.2: a) The potential for neutral atoms arising due to the Zeeman effect. Only states with a negative magnetic moment can be trapped, which are called *low field seekers*, because local magnetic maxima cannot be realized. b) A three wire configuration with a local minimum in the magnetic field is shown, which forms a one-dimensional waveguide.

magnetic field, is determined by [61, 67]

$$V_{HFS} = g_F \mu_b m_F B \ , \tag{2.38}$$

where m_F is the quantum number of the total angular momentum in direction of the magnetic field, g_F is the Landé factor. For a negative magnetic moment $g_F m_F$ the atoms tend to higher magnetic fields and the corresponding states are called *high field seekers*. In the opposite case of a positive magnetic moment the atoms experience a force to the minimum of the magnetic field, those states are called *low field seekers*. Since it is not possible to create magnetic fields with a local maximum at least for a current free region (shown in [68]), we look for magnetic potentials with a local minimum and therefore low field seekers are considered. Additionally a field configuration is desirable, where the magnetic field does not vanish at the minimum of the trap, because otherwise the magnetic moment is not aligned to the field and spin flip processes can occur. In the case of a spin flip the atom then experiences a maximum of the potential and is expelled from the trap leading to losses of atoms. The potential situation is depicted in Fig. 2.2 a. A minimum of the magnetic field can be achieved for example with a three wire configuration shown in Fig. 2.2 b, which creates an elongated quasi one-dimensional waveguide in the direction of the wire. Such a setup has also been successfully mounted on a micro fabricated chip [18].

CHAPTER 3

Transport through two-dimensional systems

The current chapter is focused on the transport of Bose-Einstein condensates through systems confined to two dimensions. In the third direction we assume a strong confinement forcing the condensate to remain in the transverse ground state. We analyze the time-dependent dynamics of the condensate subject to a scattering potential. Therefore we develop our numerical approach to study scattering effects.

The confinement to two dimensions can be realized as discussed in the previous chapter with two reverse propagating laser beams in the transverse direction forming a static lattice potential. The transverse potential minimum where the Bose-Einstein condensate is transferred to, can be approximated as a harmonic potential, character-

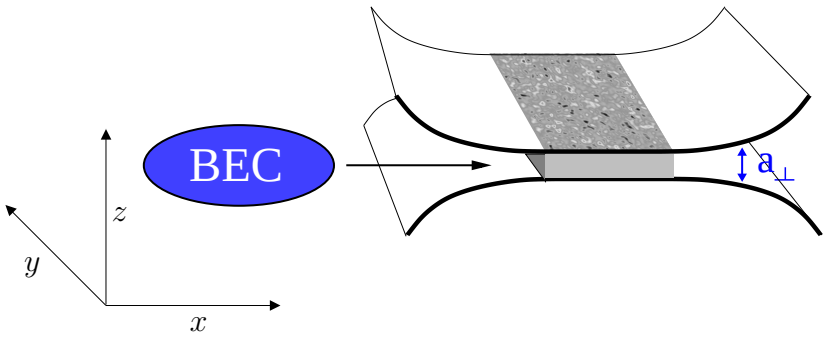

Figure 3.1: Schematic setup of the system under investigation. A Bose-Einstein condensate is transferred into the two-dimensional wave guide with transverse extent $a_\perp$ where it is exposed to a scattering potential.

ized by the oscillator length $a_\perp(\mathbf{r}) = \sqrt{\hbar/[m\omega_\perp(\mathbf{r})]}$. We assume that the oscillator length is either independent or only adiabatically dependent on the position $\mathbf{r}$. In the mean-field approximation the dynamics of the condensate is well described with the two-dimensional Gross-Pitaevskii equation ($\mathbf{r} = (x, y)$) as given in Eq. 2.30:

$$i\hbar\frac{\partial}{\partial t}\Psi(\mathbf{r},t) = \left(-\frac{\hbar^2}{2m}\Delta + V(\mathbf{r}) + \frac{\hbar^2 g(\mathbf{r})}{2m}|\Psi(\mathbf{r},t)|^2\right)\Psi(\mathbf{r},t). \tag{3.1}$$

The strength of the atom-atom interaction is given by the dimensionless quantity $g(\mathbf{r}) = 4\sqrt{2\pi}a_s/a_\perp(\mathbf{r})$, where a_s is the s-wave scattering length.

With this setup it is now possible to study the expansion process of Bose-Einstein condensates in different potential geometries like lattice potentials, cavities or disorder potentials. In the latter case experiments were performed in one-dimensional wave guides in order to investigate the regime of Anderson localization[26–31]. A Bose-Einstein condensate is created in a three-dimensional harmonic trap where the ground state wave function is either Gaussian-shaped in the weakly interacting regime or shaped like an inverted parabola in the Thomas-Fermi regime [62]. The condensate is then transferred to the wave guide and the expansion process can be analyzed. One disadvantage of such a situation is that the initial wave packet has a broad spread in momentum and the interesting quantities like the localization length depend on the $\mathbf{k}$-vector. Consequently the interpretation of the experimental results gets more complex [32].

The approach we have chosen is to investigate scattering processes with a fixed incident $\mathbf{k}$-vector [19, 69]. Experimentally this could be achieved by feeding a broad wave packet (small momentum spread) into the wave guide (see Fig. 3.1) or in one-dimensional wave guides with the technique of atom lasers [15–17]. This method might be also extended to two-dimensional systems. In the analytical and numerical implementation we add an inhomogeneous source term to the Gross-Pitaevskii equation which describes the coupling from a reservoir of Bose-Einstein condensate to the wave guide (see Fig. 3.2). This approach was introduced for one-dimensional systems in Ref. [69]. The Gross-Pitaevskii equation with source term reads:

$$i\hbar\frac{\partial}{\partial t}\Psi(\mathbf{r},t) = \left(-\frac{\hbar^2}{2m}\Delta + V(\mathbf{r}) + \frac{\hbar^2 g(x)}{2m}|\Psi(\mathbf{r},t)|^2\right)\Psi(\mathbf{r},t) + S(\mathbf{r},t)\,\mathrm{e}^{-i\mu t/\hbar}. \tag{3.2}$$

In the following we use a source $S(\mathbf{r},t) = S_0(t)\phi_S(y)\delta(x - x_0)$ that emits along a line at position x_0 with a transverse intensity profile $\phi_S(y)$. Furthermore $\mu = \hbar^2k^2/2m$ is the chemical potential of the BEC in the reservoir.

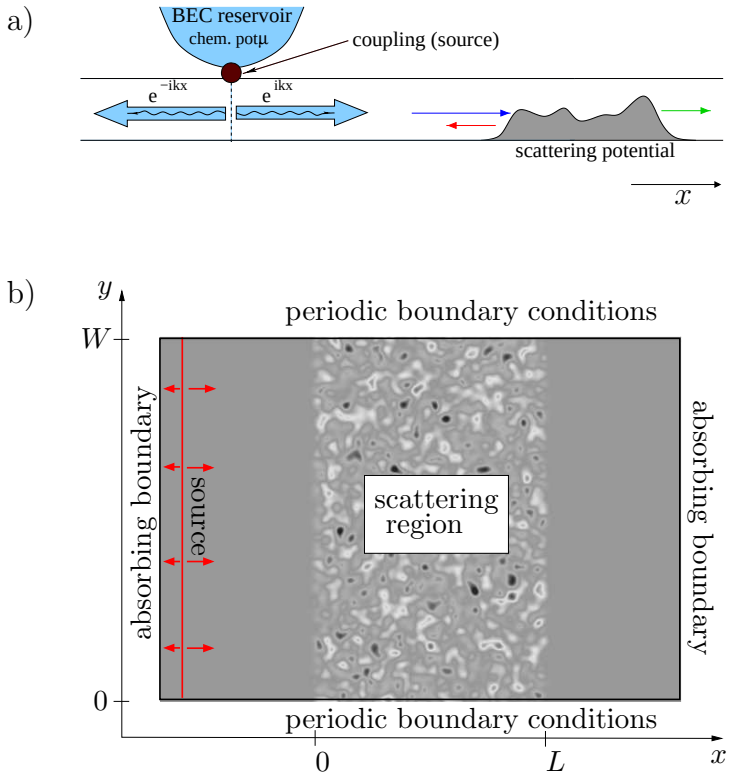

Figure 3.2: In the upper figure the coupling mechanism of a reservoir of Bose-Einstein condensate to a wave guide is shown schematically. The δ-like source at position x_0 emits a plane wave $e^{\pm ikx}$ to the left and right side with $\mu = \hbar^2 k^2/2m$. In the lower figure the setup of the two-dimensional simulation region is shown. The source emits plane waves along the x-direction. Absorbing boundaries are implemented at the left and right boundary, and periodic boundaries are used at the top and bottom.

3.1 Numerical integration scheme for the Gross-Pitaevskii equation

Below we derive a numerical integration scheme for the time-dependent Gross-Pitaevskii equation with the following properties: First off all the method should be applicable to the nonlinear wave equation. In order to couple the condensate into the simulation region with a specified wave vector we need to include the source term. The next demand for the numerical setup is that at the boundaries of the simulation region in x-direction approaching waves are absorbed with high efficiency. Whereas in the y-direction we want to implement periodic boundary conditions. Last but not least the numerical method should be accurate, especially the norm of the wave function has to be conserved (without absorbing boundaries and source term).

First we start to discuss an integration method for a linear Hamilton system excluding the nonlinearity, but with a time-dependent potential. Later we take the nonlinearity into account by replacing the potential $V(\mathbf{r},t)$ by an effective potential $V_{\text{eff}}(\mathbf{r},t) = V(\mathbf{r}) + g|\Psi(\mathbf{r},t)|^2$.
The inhomogeneous Schrödinger equation reads as follows:

$$i\hbar\frac{\partial}{\partial t}\Psi(x,y,t) = H(t)\Psi(x,y,t) + S(x,y,t)\mathrm{e}^{-i\mu t} \tag{3.3}$$

where $H(t) = T_x + T_y + V(t) + D_x$ and T_x, T_y are operators for the kinetic energy in x and y direction respectively, V is the potential and D_x is an operator describing the absorbing boundaries. With the ansatz $\Psi(\mathbf{r},t) = \Phi(\mathbf{r},t)\exp(-i\mu/\hbar)$ it is possible to split off the trivial time-dependence: $i\hbar\frac{\partial}{\partial t}\Phi = (H(t)-\mu)\,\Phi + S(t)$. With the definitions $\tilde{H}(t) = H(t) - \mu = \tilde{T_x} + T_y + V(t)$ and $\tilde{T_x} = T_x + D_x - \mu$ we get:

$$i\hbar\frac{\partial}{\partial t}\Phi = \tilde{H}(t)\Phi + S(t) \tag{3.4}$$

Integrating this equation results in:

$$\Phi(t) = \mathcal{T}\mathrm{e}^{-\frac{i}{\hbar}\int_{t_0}^{t}\tilde{H}(t')dt'}\Phi(t_0) - \frac{i}{\hbar}\int_{t_0}^{t}\mathcal{T}\mathrm{e}^{-\frac{i}{\hbar}\int_{t'}^{t}\tilde{H}(t'')dt''}S(t')dt' \tag{3.5}$$

where $\Phi(t_0)$ is the initial wave function and $\mathcal{T}$ is the time-ordering operator.

To obtain the propagation term $\Phi(t+\Delta)$ we execute following steps: First we solve the initial value problem, that means we propagate the Eq. 3.5 one time step $\Delta/2$ starting from the initial wave function $\Phi(t)$. Then we repeat this backward in time starting from the wave function $\Phi(t+\Delta)$ and expressing $\Phi(t+\frac{\Delta}{2})$ (final value problem). Furthermore we can apply the trapezoidal rule to approximate the above equation for the initial and final value problem:

$$\int_{x_1}^{x_2} f(x)dx \approx \frac{1}{2}(f(x_1)+f(x_2))(x_2-x_1) \tag{3.6}$$

This approximation is valid for small time steps Δ, and yields by eliminating $\Phi(t+\Delta/2)$ a higher order integration scheme. By merging the two expressions for $\Phi(t+\frac{\Delta}{2})$ we get the final result (Eq. 3.9) $\Phi(t)$.

Step $t \to t+\frac{\Delta}{2}$:

$$\Phi(t+\frac{\Delta}{2}) = \mathcal{T}\mathrm{e}^{-\frac{i}{\hbar}\int_0^{\Delta/2}\tilde{H}(t+\tau)d\tau}\Phi(t) - \frac{i}{\hbar}\int_0^{\Delta/2}\mathcal{T}\mathrm{e}^{-\frac{i}{\hbar}\int_\tau^{\Delta/2}\tilde{H}(t+\tau')d\tau'}S(t+\tau)d\tau$$

Step $t+\Delta \to t+\frac{\Delta}{2}$:

$$\Phi(t+\frac{\Delta}{2}) = \mathcal{T}\mathrm{e}^{+\frac{i}{\hbar}\int_0^{\Delta/2}\tilde{H}(t+\Delta-\tau)d\tau}\Phi(t+\Delta) + \frac{i}{\hbar}\int_0^{\Delta/2}\mathcal{T}\mathrm{e}^{+\frac{i}{\hbar}\int_\tau^{\Delta/2}\tilde{H}(t+\Delta-\tau')d\tau'}S(t+\Delta-\tau)d\tau$$

Applying the trapezoidal rule to the above equation for the initial and final value problem and merging the two equations we find:

$$\begin{aligned}\Phi(t+\frac{\Delta}{2}) &\approx \mathrm{e}^{-\frac{i}{\hbar}(\tilde{H}(t)+\tilde{H}(t+\Delta/2))\frac{\Delta}{4}}\Phi(t) - \frac{i\Delta}{4\hbar}\left(\mathrm{e}^{-\frac{i}{\hbar}(\tilde{H}(t)+\tilde{H}(t+\Delta/2))\frac{\Delta}{4}}S(t)+S(t+\frac{\Delta}{2})\right)\\ &\approx \mathrm{e}^{\frac{i}{\hbar}(\tilde{H}(t+\Delta/2)+\tilde{H}(t+\Delta))\frac{\Delta}{4}}\Phi(t+\Delta)\\ &\quad +\frac{i\Delta}{4\hbar}\left(\mathrm{e}^{+\frac{i}{\hbar}(\tilde{H}(t+\Delta/2)+\tilde{H}(t+\Delta))\frac{\Delta}{4}}S(t+\Delta)+S(t+\frac{\Delta}{2})\right).\end{aligned}$$

To abbreviate the above equation we define the following short notation, which is also for small time steps Δ a good approximation. For now it is just an abbreviation, as we can can later come back to the original formula:

$$\tilde{H}(t+\Delta/4) \approx \frac{1}{2}[\tilde{H}(t)+\tilde{H}(t+\Delta/2)] \qquad \text{and} \tag{3.7}$$

$$\tilde{H}(t+3\Delta/4) \approx \frac{1}{2}[\tilde{H}(t+\Delta/2)+\tilde{H}(t+\Delta)]. \tag{3.8}$$

With this we end up at the final propagation scheme:

$$\begin{aligned}\Phi(t+\Delta) = \mathrm{e}^{-\frac{i}{\hbar}\tilde{H}(t+\frac{3}{4}\Delta)\Delta/2}\Big[\mathrm{e}^{-\frac{i}{\hbar}\tilde{H}(t+\frac{1}{4}\Delta)\Delta/2}\left(\Phi(t)-\frac{i\Delta}{4\hbar}S(t)\right)\\ -\frac{i\Delta}{2\hbar}S(t+\Delta/2)\Big]-\frac{i\Delta}{4\hbar}S(t+\Delta).\end{aligned} \tag{3.9}$$

In this formulation one has to apply the propagation step onto the two-dimensional wave function as a whole, which is usually time consuming. Therefore in order to implement this scheme efficiently we have to make further approximations. We can split the propagation into several effective one-dimensional problems. Therefore we use the split-operator technique:

$$\mathrm{e}^{-i\tilde{H}(t)\tau/\hbar} \approx \mathrm{e}^{-i\tilde{T}_x\tau/\hbar}\,\mathrm{e}^{-iT_y\tau/\hbar}\,\mathrm{e}^{-iV(t)\tau/\hbar} \approx \mathrm{e}^{-iV(t)\tau/\hbar}\,\mathrm{e}^{-iT_y\tau/\hbar}\,\mathrm{e}^{-i\tilde{T}_x\tau/\hbar} \tag{3.10}$$

The symmetrization of the split-operator technique results according to the Baker-Campbell-Hausdorff formula [67] to a higher order integration scheme. Applying this method to the propagation step the final result is

$$\begin{aligned}\Phi(t+\Delta) = \mathrm{e}^{-\frac{i}{\hbar}V(t+\frac{3}{4}\Delta)\Delta/2}\mathrm{e}^{-\frac{i}{\hbar}T_y\Delta/2}\mathrm{e}^{-\frac{i}{\hbar}T_x\Delta/2}\\ \left[\mathrm{e}^{-\frac{i}{\hbar}T_x\Delta/2}\mathrm{e}^{-\frac{i}{\hbar}T_y\Delta/2}\mathrm{e}^{-\frac{i}{\hbar}V(t+\frac{1}{4}\Delta)\Delta/2}\left(\Phi(t)-\tfrac{i\Delta}{4\hbar}S(t)\right)-\tfrac{i\Delta}{2\hbar}S(t+\Delta/2)\right]\\ -\tfrac{i\Delta}{4\hbar}S(t+\Delta).\end{aligned} \tag{3.11}$$

In this way every step is effectively one-dimensional. This improves the scaling of the execution time of the code with system size quite a lot. The above formula is complicated, and for clarity we write this equation again in a more descriptive way ($\hbar=1$):

$$\begin{array}{rcl} \Phi(t+\Delta) & = & \underset{\uparrow}{\mathrm{e}^{-iV\,\Delta/2}}\ \underset{\uparrow}{\mathrm{e}^{-iT_y\,\Delta/2}}\ \underset{\uparrow}{\mathrm{e}^{-i\tilde{T}_x\,\Delta/2}}\ \underset{\uparrow}{\mathrm{e}^{-i\tilde{T}_x\,\Delta/2}}\ \underset{\uparrow}{\mathrm{e}^{-iT_y\,\Delta/2}}\ \underset{\uparrow}{\mathrm{e}^{-iV\,\Delta/2}}\ \Phi(t). \\ & & \quad -\frac{i\Delta}{4}S \qquad\qquad -\frac{i\Delta}{2}S \qquad\qquad -\frac{i\Delta}{4}S \end{array} \tag{3.12}$$

In the following we use two different integration schemes for the x- and y-direction. In the y-direction we use a Fourier propagation method, since it intrinsically implements periodic boundary conditions, and in x-direction we employ the Crank-Nicolson integration scheme, which allows to incorporate absorbing boundaries at the left and right side of the simulation region.

3.2 Fourier Propagation

In this section we explain the details of the propagation along the y-direction method by employing the Fourier transformation to calculate T_y. For simplicity we neglect the source term here. The inclusion of the source term will be described later on. First of all we define the Fourier transformation of the wave function in y-direction:

$$\Phi(k_y) = \mathcal{F}\Phi(y) = \frac{1}{W}\int_0^W \mathrm{e}^{-ik_y y}\Phi(y)\,dy \tag{3.13}$$

$$\Phi(y) = \mathcal{F}^{-1}\Phi(k_y) = \sum_{k_y} \mathrm{e}^{ik_y y}\Phi(k_y)\ . \quad \text{with} \quad k_y = n\frac{2\pi}{W}, \quad n\in\mathbb{Z}\ , \tag{3.14}$$

where W is the width of the two-dimensional system (see Fig. 3.2). The idea of the Fourier method here is to apply a transformation in a way that the kinetic operator in y-direction gets diagonal. Then the propagation of a time step is just a multiplication with a complex number. Applying a Fourier transformation to the kinetic energy operator has the desired effect:

$$\bar{T}_y = \mathcal{F}\,T_y\,\mathcal{F}^{-1} = \mathcal{F}\left(-\frac{\hbar^2}{2m}\frac{\partial^2}{\partial y^2}\right)\,\mathcal{F}^{-1} = \frac{\hbar^2 k_y^2}{2m}\ . \tag{3.15}$$

Therefore we can write a propagation step of the wave function in the following way:

$$\mathrm{e}^{-iT_y\,\Delta/2\hbar} \rightarrow \mathcal{F}^{-1}\,\mathrm{e}^{-i\bar{T}_y\,\Delta/2\hbar}\,\mathcal{F}\ . \tag{3.16}$$

This means we first apply a Fourier transformation, multiply the wave function with a complex number and then apply a back transformation. In principle this has to be

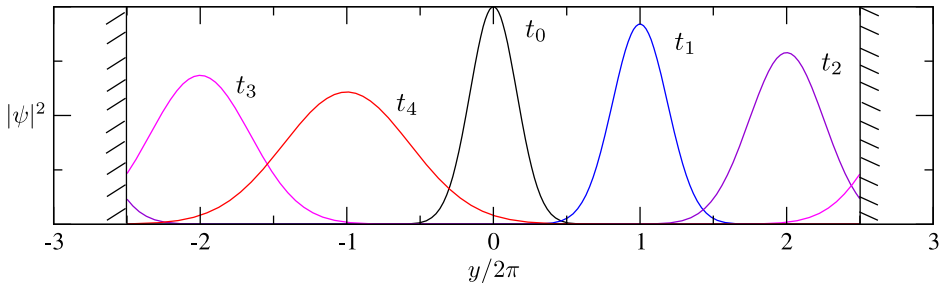

Figure 3.3: Demonstration of the periodic boundary conditions with the Fourier propagation method. A Gaussian wave packet with initial velocity is positioned on the simulation region. It propagates to the boundary and then enters from the other boundary.

done twice during one propagation step Δ, because the kinetic energy operator $\mathrm{e}^{-iT_y\,\Delta/2}$ appears twice in one propagation step (second line of Eq. 3.17). But we can omit the second Fourier transformation (see third line of Eq. 3.17) by applying the propagation in x-direction, because the operator $\tilde{T}_x$ is invariant under Fourier transformation. To this end we apply $\tilde{T}_x$ not on the wave function $\Phi(x, \boldsymbol{y}, t)$ but instead on the partially Fourier transformed wave function $\Phi(x, \boldsymbol{k_y}, t)$, which is in addition advantageous as explained later on.

$$\begin{aligned}
\Phi(t+\Delta) &= \mathrm{e}^{-iV\,\Delta/2\hbar}\,\mathrm{e}^{-iT_y\,\Delta/2\hbar}\,\mathrm{e}^{-i\tilde{T}_x\,\Delta/\hbar}\,\mathrm{e}^{-iT_y\,\Delta/2\hbar}\,\mathrm{e}^{-iV\,\Delta/2\hbar}\,\Phi(t) \\
&= \mathrm{e}^{-iV\,\Delta/2\hbar}\,\boldsymbol{\mathcal{F}}^{-1}\,\mathrm{e}^{-i\bar{T}_y\,\Delta/2\hbar}\,\boldsymbol{\mathcal{F}}\,\mathrm{e}^{-i\tilde{T}_x\,\Delta/\hbar}\,\boldsymbol{\mathcal{F}}^{-1}\,\mathrm{e}^{-i\bar{T}_y\,\Delta/2\hbar}\,\boldsymbol{\mathcal{F}}\,\mathrm{e}^{-iV\,\Delta/2\hbar}\,\Phi(t) \\
&= \mathrm{e}^{-iV\,\Delta/2\hbar}\,\boldsymbol{\mathcal{F}}^{-1}\,\mathrm{e}^{-i\bar{T}_y\,\Delta/2\hbar}\,\mathrm{e}^{-i\tilde{T}_x\,\Delta/\hbar}\,\mathrm{e}^{-i\bar{T}_y\,\Delta/2\hbar}\,\boldsymbol{\mathcal{F}}\,\mathrm{e}^{-iV\,\Delta/2\hbar}\,\Phi(t) \qquad (3.17)
\end{aligned}$$

The method of the Fourier transformation has the advantage that the desired periodic boundary condition is already implemented intrinsically. A demonstration of this property is illustrated in Fig. 3.3. A Gaussian wave packet $\psi(y,t)$ with initial velocity is positioned on the simulation region:

$$\psi(y,t) = \mathrm{e}^{-y^2/2+ik_y}\ . \qquad (3.18)$$

The wave packet propagates to the right boundary and enters from the left hand side again. During the propagation the wave packet spreads of course.

3.3 Finite Difference Approximation

In this section we describe the integration scheme in x-direction with the method of finite differences. For the moment we neglect the absorbing boundaries and the

source term. As explained already we can apply to every k_y point a one-dimensional propagation along the x-direction. Here we approximate the time evolution of the unitary operator $\mathrm{e}^{-\frac{i}{\hbar}\tilde{T}_x\,\Delta}$ with the Crank-Nicolson integration scheme [65, 69–71].

$$\mathrm{e}^{-\frac{i}{\hbar}\tilde{T}_x\,\Delta}\,\Phi(x,k_y,t) \approx \frac{1}{1+\frac{i\Delta}{2\hbar}\tilde{T}_x}\left(1-\tfrac{i\Delta}{2\hbar}\tilde{T}_x\right)\,\Phi(x,k_y,t)\;. \tag{3.19}$$

Note that this approximated time evolution operator in Eq. 3.19 is unitary and conserves the norm of the wave function. Furthermore it is of order $\mathcal{O}(\Delta^2)$ in the time step Δ. This implicit integration scheme for the wave function reads then

$$\left(1+\frac{i\Delta}{2\hbar}\tilde{T}_x\right)\Phi(x,k_y,t+\Delta) = \left(1-\frac{i\Delta}{2\hbar}\tilde{T}_x\right)\Phi(x,k_y,t). \tag{3.20}$$

We write the wave function in the lattice representation with N_x lattice sites and a lattice spacing of $\Delta_x = (x_{max}-x_{min})/N$ in the following way: $\Phi^n_{j,k_y} = \Phi(x_{min}+j\Delta_x, k_y, t_0+n\Delta)$, where the upper index n indicates the discrete time, and the lower index j the discrete position. Here x_{min} and x_{max} are the lattice boundaries. Using the finite-difference representation for the Hamilton operator $\tilde{T}_x$ we find

$$\left(1\pm\frac{i\Delta}{2\hbar}\tilde{T}_x\right)\Phi^n_{j,k_y} \simeq \Phi^n_{j,k_y} \pm \frac{i\Delta}{2\hbar}\left[-\frac{\hbar^2}{2m}\frac{\Phi^n_{j+1,k_y}-2\Phi^n_{j,k_y}+\Phi^n_{j-1,k_y}}{\Delta_x^2} - \mu\Phi^n_{j,k_y}\right] \tag{3.21}$$

The lattice points Φ^n_{j,k_y} can be written in vectorial form $\vec{\Phi}^n_{k_y} = (\Phi^n_{0,k_y},..,\Phi^n_{N-1,k_y})$. With this definition Eq. 3.20 can be rewritten in matrix representation:

$$\mathbf{D}_2\;\vec{\Phi}^{n+1}_{k_y} \;=\; \mathbf{D}_1\;\vec{\Phi}^n_{k_y} \tag{3.22}$$

with the definitions of the matrices

$$\mathbf{D}_1 \equiv \left[\left(1-\frac{i\Delta}{2\hbar}\tilde{T}_x\right)\right],\; \mathbf{D}_2 \equiv \left[\left(1+\frac{i\Delta}{2\hbar}\tilde{T}_x\right)\right]\;. \tag{3.23}$$

This shows that we have to solve a system of linear equations, and that the matrices $\mathbf{D}_1$ and $\mathbf{D}_2$ are tridiagonal matrices.

Up to now we have excluded the source term. This can easily be incorporated in this finite difference scheme. According to Eq. 3.12 or Eq. 3.11 the full equation in x-direction we have to solve including the source term is as follows:

$$\Phi(x,k_y,t+\Delta) = \mathrm{e}^{-\frac{i}{\hbar}T_x\Delta/2}\left[\mathrm{e}^{-\frac{i}{\hbar}T_x\Delta/2}\Phi(x,k_y,t) - \tfrac{i\Delta}{2\hbar}S(x,k_y,t+\Delta/2)\right]\;. \tag{3.24}$$

Here the source term $S(x,k_y,t) = S_0(t)\phi_S(k_y)\delta(x-x_0)$ is the Fourier transform of $S(x,y,t)$, but only in y-direction. The source is a δ-function in x-direction positioned

at $x_0 = x_{min} + j'\Delta_x$ (see Fig. 3.2). In order to incorporate the source term into our matrix representation we define the components of the vector $\vec{b}_{k_y}^{n+\frac{1}{2}}$

$$b_{j,k_y}^{n+\frac{1}{2}} = \frac{i\Delta}{2\hbar}\, S_0(t+\Delta/2)\, \phi_S(k_y)\, \delta_{j\,j'}\ . \tag{3.25}$$

This leads to our final result for the integration step with the finite difference method:

$$\mathbf{D}_2\, \vec{\Phi}_{k_y}^{n+1} + \vec{b}^{n+\frac{1}{2}} \ = \ \mathbf{D}_1\, \vec{\Phi}_{k_y}^{n}\ . \tag{3.26}$$

This system of linear equations with an inhomogeneous term is solved very efficiently in a numerical implementation. The next step is to include the absorbing boundaries in the propagation step. The method we use is only possible in this Crank-Nicolson integration scheme.

3.4 Absorbing Boundaries in two dimensions

In the numerical simulation we are faced with the difficulty, that we want to study scattering states which are extended to infinity to the left and to the right. But in the numerical implementation we are limited to compute in a finite region. The boundary introduces artificial back reflection in the case of the finite difference method, or recurrences due to periodic boundary conditions in the case of the Fourier propagation method. In order to tackle this problem we can either extend the lattice so that the wave packet does not reach the boundary during the propagation time, or we modify the integration scheme in order to suppress this artificial back reflection. The easiest method is the use of a complex potential, but the precision is not very accurate. Another method was introduced by T. Shibata [72] for one-dimensional systems which is especially suited in the case of scattering states with a narrow momentum distribution. In this section we generalize this method to two-dimensional systems in order to absorb wave functions at the left and right end of the numerical setup, according to Fig. 3.2, where the wave function approaches the boundary with an arbitrary angle, or even with an angular distribution.

We assume that the potential does not depend on y near the right or left boundary $V(\mathbf{r}) = V(x)$. In our case we especially use a flat potential there. The idea is to decompose the wave function along the y-direction into eigenstates. This is achieved in the case of the flat potential with the Fourier transformation in y-direction.

$$\bar{\Phi}(x,k_y) = \mathcal{F}\Phi(x,y) = \frac{1}{2\pi W}\int_0^W \mathrm{e}^{-ik_y y}\Phi(x,y)\, dy \tag{3.27}$$

Due to the eigenmode decomposition and the constant potential $V(x)$ near the boundary, the different eigenmodes do not interact anymore near the boundary. Therefore

they can be considered separately. With this trick we have reduced the task of two-dimensional absorption to the absorption in each one-dimensional Fourier mode k_y separately. This brings us back to the method of T. Shibata in one dimension $\bar{\Phi}(x; k_y)$.

Of course this method relies on the eigenmode decomposition, which is only possible for linear systems. Therefore we have to pay special attention in applying this method to the nonlinear Gross-Pitaevskii equation. To this end we switch off the nonlinearity adiabatically when approaching the boundary (see Sec. 3.6 for details).

Let us illustrate for example an incoming wave with chemical potential $\mu = \frac{\hbar^2|\mathbf{k}|^2}{2m}$. This wave gets scattered elastically in the potential under investigation, and finally approaches the boundary. Note that also in the case of the Gross-Pitaevskii equation we have only elastic scattering processes. We apply the eigenmode decomposition, in our case the Fourier transformation to obtain $\Phi(x; k_y)$. At the boundary we therefore have to absorb a wave with wave vector $k_x = \pm\sqrt{\frac{2m}{\hbar^2}\mu - k_y^2}$ in mode k_y. Of course this is only possible in the regime $\frac{\hbar^2 k_y^2}{2m} < \mu$, otherwise we have evanescent modes, which we discuss later.

Now we briefly discuss the absorbing boundary conditions for the Schrödinger equation introduced by T. Shibata [72]. We consider

$$i\hbar\frac{\partial}{\partial t}\Phi(x, k_y, t) = \left(-\frac{\hbar^2}{2m}\frac{\partial^2}{\partial x^2} - \frac{\hbar^2 k_y^2}{2m} + V_{ext}\right)\Phi(x, k_y, t), \tag{3.28}$$

where V_{ext} is a constant external potential. The wave functions $\Phi(x, k_y, t) = Ae^{-i(\mu t/\hbar - k_x x)}$ are then solutions with the dispersion relation

$$\hbar k_x = \pm\sqrt{2\left[\mu - V(k_y)\right]}, \tag{3.29}$$

where we defined the potential $V(k_y) = -\frac{\hbar^2 k_y^2}{2m} + V_{ext}$. The plus and minus signs in this equation correspond to left- and right-going waves. Therefore we want that the absorbing boundaries fulfill the branch of the dispersion relation for right moving waves at the right side of the grid, and the other branch at the left side of the grid. These are the so-called "one-way wave equations", allowing only outgoing waves. The nonlinear dispersion relation Eq. 3.29 is now approximated by a linear one:

$$\hbar k_x = g_1(\mu - V) + g_2, \tag{3.30}$$

where we have defined g_1 and g_2 according to Fig. 3.4. The approximation is chosen in such a way that it is optimal in a small interval around the energy of the incident wave:

$$\begin{aligned} g_1 &\equiv \pm\frac{\sqrt{2m\alpha_2} - \sqrt{2m\alpha_1}}{\alpha_2 - \alpha_1}, \\ g_2 &\equiv \pm\frac{\alpha_2\sqrt{2m\alpha_1} - \alpha_1\sqrt{2m\alpha_2}}{\alpha_2 - \alpha_1}. \end{aligned} \tag{3.31}$$

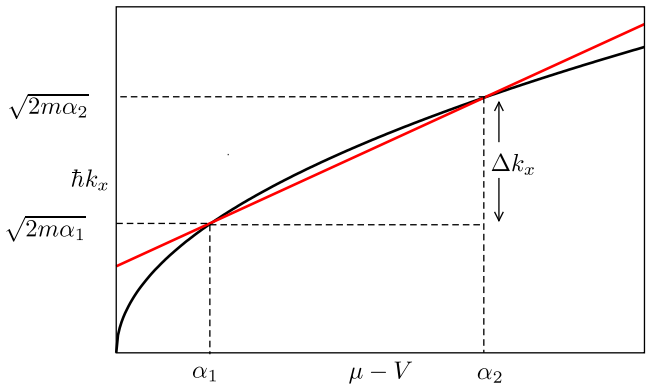

Figure 3.4: The positive branch of the dispersion relation of a plane wave (black line) is approximated by a linear function (straight blue line). The parameters α_1, α_2 are chosen such that the wave numbers of the plane waves to be absorbed lie within the momentum interval Δk_x.

The linearized dispersion relation Eq. 3.30 can now be transformed into a partial differential equation via the following duality relations:

$$i\hbar\frac{\partial}{\partial t} \Longleftrightarrow \mu, \qquad \frac{\partial}{\partial x} \Longleftrightarrow ik \; . \tag{3.32}$$

Finally, we arrive at a one-way wave equation:

$$i\hbar\frac{\partial}{\partial t}\Phi(x, k_y, t) \;\; = \;\; \left(-i\hbar\frac{1}{g_1}\frac{\partial}{\partial x} + V(k_y) - \frac{g_2}{g_1}\right)\Phi(x, k_y, t) \; . \tag{3.33}$$

This one-way wave equation can be easily implemented in combination with the Crank-Nicolson integration scheme. Only the boundary entries in the tridiagonal matrices $\mathbf{D}_1$ and $\mathbf{D}_2$ in Eq. 3.26 have to be modified. No additional calculation step is needed. The corresponding matrix elements for the implementation of the absorbing boundaries are presented in Ref [72, 73].

These boundary conditions absorb with a high degree of precision. This is demonstrated in the examples of Fig. 3.10 and Fig. 3.11. Note that this boundary conditions absorb superpositions of waves with momentum $\hbar k_x$ satisfying $\sqrt{2m\alpha_1} \lesssim \hbar k_x \lesssim \sqrt{2m\alpha_2}$.

Note that α_1 and α_2 depend on the transverse Fourier mode k_y due to the potential $V(k_y)$. This is because we fix the absolute value of the wave vector of the incoming wave $|\mathbf{k}|$, and then adjust mode the optimal momentum for absorption to $k_x = \pm\sqrt{|\mathbf{k}|^2 - k_y^2}$ in every k_y.

Evanescent modes - Complex absorbing Potentials

As seen above the method of T. Shibata can only be used in the case of $\frac{\hbar^2 k_y^2}{2m} < \mu$. Otherwise $k_x = \pm\sqrt{\frac{2m}{\hbar^2}\mu - k_y^2}$ is imaginary, and this leads to a numerical instability in the above method. This imaginary k_x corresponds to exponentially damped modes and those do not propagate. They are called evanescent modes. Usually we do not need to care about these modes, because they are damped anyway. Nevertheless in a calculation over long times an artificial back-reflected background is accumulated, especially in the case of slowly damped evanescent modes $\frac{\hbar^2 k_y^2}{2m} \lesssim \mu$. In order to reduce this artifacts we use complex absorbing potentials.

This is another often used method to suppress artificial back reflection from the boundaries. To this end one adds an imaginary part to the potential $V(\mathbf{r})$ in the time-dependent integration procedure:

$$\Phi(\mathbf{r}, t+\Delta) = \mathrm{e}^{-\frac{i}{\hbar}(T+V(\mathbf{r}))\Delta}\, \Phi(\mathbf{r}, t) \qquad \text{with } \Im(V(\mathbf{r})) < 0\ . \tag{3.34}$$

In the inside of the simulation region this imaginary part is zero and is finite near the boundary. The increase to the final value at the boundary of such an imaginary part has to be very smoothly and the strength of such an imaginary part has to be tuned very carefully and it has to be adjusted for every situation separately. There are many free parameters to fit in contrast to the method of T. Shibata with only one parameter. Nevertheless we can use complex absorbing potentials, because the modes are already damped due to the evanescent character and therefore high accuracy is not too critical, compared to propagating modes. Specifically we use a quadratic function for the imaginary potential, which continuously starts to increase at $3\pi/k$ away from the boundary.

With the combination of these two methods we arrive at a description for the boundary which absorbs a two-dimensional wave packet with a momentum spread adjusted by α_1 and α_2. The absorption is of very high accuracy and artificial back-reflections are strongly suppressed. The quality depends mainly on the lattice spacing of the numerical grid. We optimized this in such a way that in all calculations we have in the long time limit less than 1% back reflection. Most of the time we achieve 0.25% or less intensity oscillations due do artificial back reflection. Additionally this method seamlessly integrates into the whole time dependent propagation scheme, since the decomposition in eigenmodes is already performed due to the Fourier propagation method in y-direction.

3.5 Predictor-Corrector method

Up to now we described the time-dependent integration scheme for a linear Schrödinger equation but already with a time-dependent potential $V(\mathbf{r},t)$. This allows us to include the nonlinearity by replacing the potential $V(\mathbf{r},t)$ with an effective potential $V_{\text{eff}}(\mathbf{r},t) = V(\mathbf{r}) + g|\Psi(\mathbf{r},t)|^2$. The integration scheme can then be formulated in terms of the effective potential:

$$\Phi(t+\Delta) \;=\; \mathrm{e}^{-\frac{i}{\hbar}\boldsymbol{V_{\text{eff}}(t+\frac{3}{4}\Delta)}\Delta/2}\;\mathrm{e}^{-\frac{i}{\hbar}T_y\Delta/2}\mathrm{e}^{-\frac{i}{\hbar}T_x\Delta}\mathrm{e}^{-\frac{i}{\hbar}T_y\Delta/2}\;\mathrm{e}^{-\frac{i}{\hbar}\boldsymbol{V_{\text{eff}}(t+\frac{1}{4}\Delta)}\Delta/2}\;\Phi(t). \tag{3.35}$$

For the calculation of $\Phi(t+\Delta)$ from $\Phi(t)$ the unknown wave function at time $t+\frac{\Delta}{4}$ and $t+\frac{3\Delta}{4}$ enters. Assuming that the wave function is only slowly varying in time we can use the wave function at time t instead. If we let the time step Δ be infinitesimal small, the resulting error is negligible. But short time steps raise the computational time. To eliminate this problem we use the predictor-corrector method. Therefore we propagate the wave function in a first step using the effective potential at time t. In the second step we calculate the effective potential using the temporary wave function, and propagate again the same time step, but with this predicted effective potential:

- *Predictor step:* Calculate temporary $\tilde{\Phi}(t+\Delta)$
  $\Phi(t) \longrightarrow \tilde{\Phi}(t+\Delta)$
  by using $V_{\text{eff}} = V + g|\Phi(t)|^2$
- Calculate approximation for V_{eff} using linear interpolation:
  $\tilde{V}_{\text{eff}}(t+\frac{\Delta}{4}) = V + g|\frac{3}{4}\Phi(t) + \frac{1}{4}\tilde{\Phi}(t+\Delta)|^2$
  $\tilde{V}_{\text{eff}}(t+\frac{3\Delta}{4}) = V + g|\frac{1}{4}\Phi(t) + \frac{3}{4}\tilde{\Phi}(t+\Delta)|^2$
- *Corrector step:* Calculate $\Phi(t+\Delta)$ with approximated $\tilde{V}_{\text{eff}}$:
  $\Phi(t) \longrightarrow \Phi(t+\Delta)$
  using $\tilde{V}_{\text{eff}}(t+\frac{\Delta}{4})$ and $\tilde{V}_{\text{eff}}(t+\frac{3\Delta}{4})$

For an optimal result this scheme has to be iterated a couple of times until convergence is achieved, but in the investigated nonlinear regime already one recursion step is adequate.

3.6 Adiabatic change of the nonlinearity strength

In this section we bring together the *nonlinear propagation* method with the two-dimensional *absorbing boundaries* and the *source*. In order to apply the absorbing

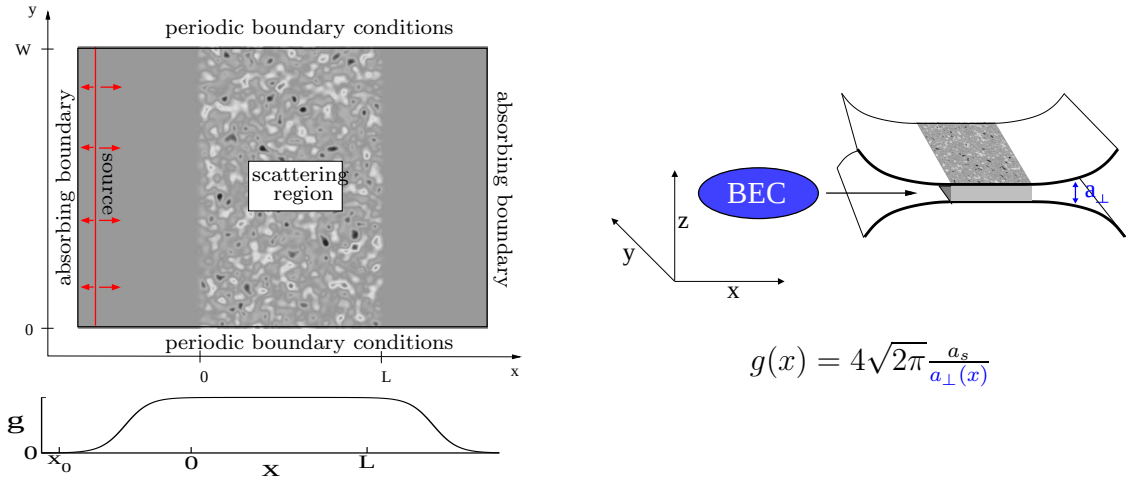

Figure 3.5: The nonlinearity $g(x)$ is adiabatically switched on inside the scattering region and switched off outside the scattering region. This is necessary for the two-dimensional absorbing boundary conditions. On the right sketch the experimental interpretation is shown. As the nonlinearity strength depends on the transverse confinement $a_\perp$ of the wave guide the reduction of the nonlinearity refers to a broadening of the wave guide. This also allows to transfer the Bose-Einstein condensate into the wave guide. If this change is slow enough, then no condensate is scattered back. a_s is the s-wave scattering length of the atom-atom interaction.

boundaries from Sec. 3.4 we have to apply an eigenmode decomposition in y-direction near the boundary. This is only possible for a linear system. Furthermore the position of the source has to be located in a linear regime in order to avoid nonlinear back-action of the wave function with the source. To get around this difficulty we change the strength of the nonlinearity slowly to zero when approaching the absorbing boundary. We also position the source in the linear regime. A schematic setup of the simulation region is shown in Fig. 3.5. We choose an adiabatic change of the nonlinearity as a function of the longitudinal direction x as follows:

$$g(x,y) \equiv g(x) = \frac{1}{2} g_0 \left[\tanh\left(\frac{2x}{x_{ad}}\right) + 1 \right]. \tag{3.36}$$

It was demonstrated by T. Paul [65] for one-dimensional wave guides that an incoming plane wave with wave vector k is transformed adiabatically to the nonlinear wave and nothing is reflected for $x_{ad} \gg \frac{2\pi}{k}$.

This adiabatic change of the nonlinearity strength $g(x)$ is not only of technical interest, it is also of experimental relevance. In an experimental setup the Bose-Einstein condensate has to be transferred to the two-dimensional wave guide. The idea is to start with a broad wave packet of condensate and move it towards the confining po-

tential with decreasing width $a_\perp$. This change of $a_\perp(x)$ is directly translated in the nonlinearity strength: $g(x) = 4\sqrt{2\pi}\frac{a_s}{a_\perp(x)}$.

3.7 Source term

In this section we show that the source term, which we introduced in Eq. 3.2 emits plane waves propagating towards the scattering potential. Since we place the source term in the linear region ($g(x) = 0$) we restrict the discussion to the Schrödinger equation with source term:

$$i\hbar\frac{\partial}{\partial t}\Psi(\mathbf{r},t) = \left(-\frac{\hbar^2}{2m}\Delta + V(\mathbf{r})\right)\Psi(\mathbf{r},t) + \; S_0(t)\phi_S(y)\delta(x-x_0)\,\mathrm{e}^{-i\mu t/\hbar}. \quad (3.37)$$

In the following we use that the source $S_0(t)\phi_S(y)\delta(x-x_0)$ emits along a line at position x_0 with a transverse intensity profile $\phi_S(y)$ and a time-dependent intensity $S_0(t)$. Furthermore μ is the chemical potential of the BEC in the reservoir. We especially focus on the case where the transverse profile is determined by $\phi_S(y) = \mathrm{e}^{ik_0 y}$. For the general case one has to decompose $\phi_S(y)$ in a superposition of Fourier modes. A solution to this inhomogeneous differential equation is given by:

$$\Psi(x,y,t) = \frac{S_0(t)m}{i\hbar^2 k_x}\mathrm{e}^{\frac{-i\mu t}{\hbar}}\mathrm{e}^{ik_0 y}\mathrm{e}^{ik_x|x-x_0|} \quad (3.38)$$

where the wave vector in x-direction is determined by $k_x = \sqrt{\frac{2m\mu}{\hbar} - k_0^2}$. We observe that the source emits a plane wave moving away from the source position x_0 with an angle $\alpha = \arctan\frac{k_0}{k_x}$, which can be illustrated with the current density:

$$\mathbf{j} = \frac{|S_0|^2}{\hbar^3|k_x|^2}\begin{pmatrix}\pm k_x\\ k_0\end{pmatrix}. \quad (3.39)$$

The plus sign corresponds to $x > x_0$ and the minus sign to $x < x_0$. In our simulations we fix the incoming current, and consequently the source term is determined by

$$|S_0|^2 = \frac{\hbar^2|k_x|^2|\mathbf{j}|}{\sqrt{2m\mu}}. \quad (3.40)$$

In order to be as close as possible to an experimental setup, we start our simulation with an empty wave guide. Then we couple a reservoir of Bose-Einstein condensate to the wave guide as depicted in Fig. 3.2, and we fill the wave guide gradually. In the alternative method where a broad wave packet of condensate is adiabatically fed into the wave guide the situation is similarly. Therefore we do not switch the source abruptly on, but instead we increase the coupling strength adiabatically from zero to

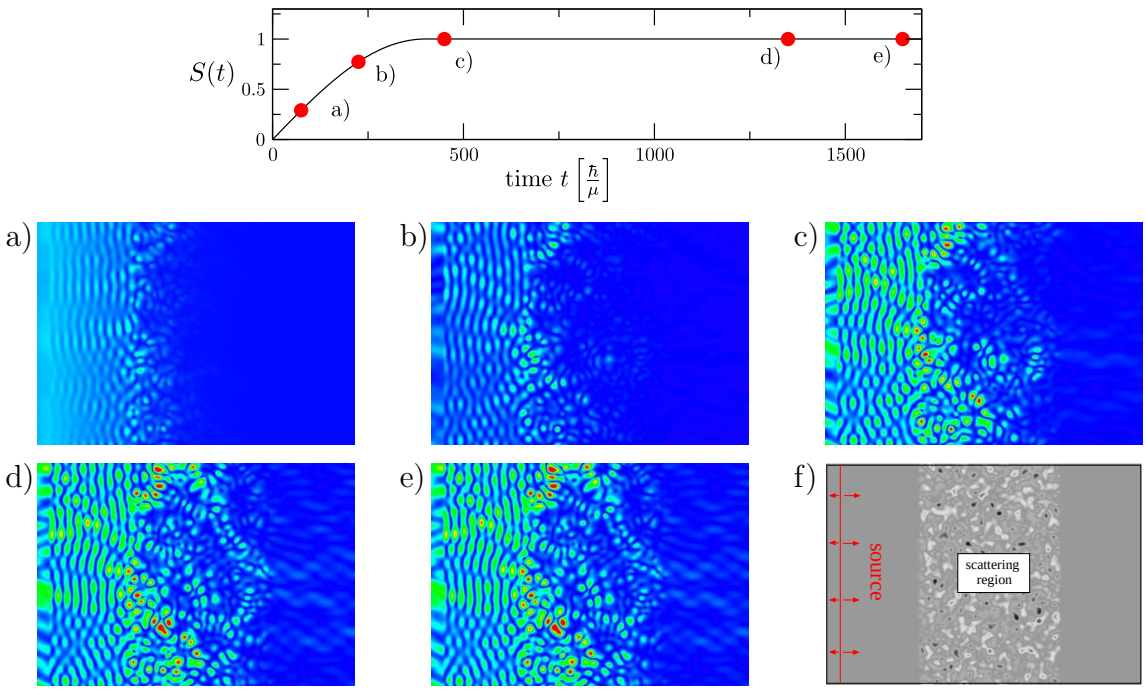

Figure 3.6: In the upper graph the adiabatic increase of the source amplitude $s(t)$ up to the final value is shown. The gradual filling of the waveguide is shown with density plots (a-e) at consecutive times corresponding to the upper graph. At the beginning the wave guide is empty, and is the slowly filled with condensate and reaches at the end a stationary scattering state. In figure f) the setup of the system is depicted.

the final value. We take the time scale for the adiabatic increase ΔT to be much larger than the characteristic time scale related to the chemical potential $\tau = \hbar/\mu \ll \Delta T$. From the numerical point of view, in the linear case of the Gross-Pitaevskii equation also convergence to a stationary scattering state is much faster reached, compared to suddenly switching the source amplitude to the final value, where oscillations emerge. Therefore we stay as close as possible to a stationary scattering state during the gradual filling, which is finally reached at the end of the calculation. In the linear case it can be shown, that a stationary solution is obtained [65], whereas in the nonlinear case it is not guaranteed that a dynamic stable solution exists. In this case the time-dependent integration scheme shows an intrinsically time-dependent wave function [19, 74]. Therefore we get additionally information about the dynamical stability of solutions.

Note that in the stationary nonlinear case there are two possible scattering states, a supersonic and a subsonic solution. Our procedure guarantees to populate always the supersonic solution [65]. This supersonic solution is the desired solution to the experimental setup described above. In principle the subsonic solution can be obtained if

one starts with a Bose-Einstein condensate which is at rest in a trap with an additional scattering potential, and then one begins to move the scattering potential [20].

3.8 Selected examples

3.8.1 Double barrier potential

In this first example we study a one-dimensional system with a double barrier potential. On the one hand this allows for a comparison to results known from Ref. [69] and to confirmation of our numerical method. On the other side we give further interpretation for the observed results, and especially relate the approach from the scattering description to the problem of a decaying quasi bound state in the nonlinear regime. To this end we consider the one-dimensional Gross-Pitaevskii equation:

$$i\hbar\frac{\partial}{\partial t}\Psi(x,t) = \left(-\frac{\hbar^2}{2m}\frac{\partial^2}{\partial x^2} + V(x) + \tilde{g}|\Psi(x,t)|^2\right)\Psi(x,t) + \; S(x,t)\,\mathrm{e}^{-i\mu t/\hbar} \quad (3.41)$$

where $\tilde{g} = 2a_s\hbar\omega_\perp$ is the one-dimensional interaction strength. We especially focus on a one-dimensional wave guide with a harmonic transverse confinement and a corresponding harmonic oscillator width of $a_\perp = \sqrt{\hbar/(m\omega_\perp)}$ in the following. We consider a double barrier potential given by:

$$V(x,y) = V_0\left(\mathrm{e}^{-\frac{|x-L/2|^2}{2\sigma^2}} + \mathrm{e}^{-\frac{|x+L/2|^2}{2\sigma^2}}\right). \quad (3.42)$$

The transmission is treated as a function of the chemical potential of the incoming wave with wave vector $k = \sqrt{2m\mu}/\hbar$ and fixed incident current. For definiteness we specify a double barrier potential with a height of $V_0 = 1.1\hbar\omega$ and a barrier width of $\sigma = 1.0a_\perp$. The two barriers are separated by a distance of $L = 4.25a_\perp$.

For the linear Schrödinger equation the double barrier potential can also be seen as a Fabry-Pérot interferometer where we get the well-known Breit-Wigner distribution for the transmission from.

$$T(\mu) = \frac{(\hbar\gamma_0/2)^2}{(\mu-\mu_0)^2 + (\hbar\gamma_0/2)^2} \quad (3.43)$$

A transmission of $T = 1$ is observed if the energy μ of the incoming monochromatic wave has a resonance frequency with energy μ_0. The width of the resonance is determined by the decay rate γ_0. Such a transmission spectrum is shown with the black line in Fig. 3.7. Of course the above Breit-Wigner distribution is only a good approximation for well separated resonances that do not overlap, which is the case for our

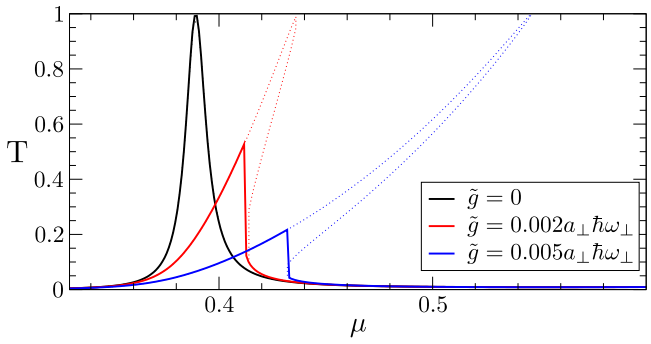

Figure 3.7: The transmission through a double barrier potential is studied. The solid line refers to the time-dependent integration of the Gross-Pitaevskii equation. The dotted line shows an alternative approach where the stationary Gross-Pitaevskii equation is solved for a fixed incident current (see Ref. [65, 73] for the methods used). Parameters: $V_0 = 1.1\hbar\omega$, $\sigma = 1.0 a_\perp$, $L = 4.25 a_\perp$, $j_i n = 1\omega$.

parameters. The energy of the lowest resonance is found at $\mu_0 = 0.389\hbar\omega$. And the next resonance is already above the potential maxima.

In Ref. [69] the transmission spectrum was studied for the nonlinear Gross-Pitaevskii equation then. It was shown there that the resonant peak bends to the right for repulsive atom-atom interaction and to the left for attractive interaction. This bending results in a bi-stability phenomenon: For a fixed incident current more than one stationary scattering solution to the stationary Gross-Pitaevskii equation is found, which is shown in the dotted lines of Fig. 3.7. The solution with high transmission results in a high population of the quasi bound state in the resonator, whereas for the solution with low transmission also a low density inside the resonator is found. Additionally we carried out the time-dependent integration process of the Gross-Pitaevskii equation, where the results are presented in the solid lines of Fig. 3.7. This shows that only the stationary solution with the lowest transmission is populated.

In the following we explain the origin of the bi-stability, and especially draw a connection between the scattering states and the corresponding decaying quasi bound states. We recognize that in the high transmitting state the corresponding high density inside the resonator shifts the resonance energy μ_0 due to the interaction energy in the nonlinear case $\mu_0 \to \mu_0(N)$, where $N = \int_{-L/2}^{L/2} |\Psi(x)|^2 dx$ is the condensate density inside the resonator. Similarly, the decay rate depends on the density $\gamma_0 \to \gamma_0(N)$. Thus, the transmission function has to be modified in the following way:

$$T(\mu) = \frac{(\hbar\gamma_0(N)/2)^2}{(\mu - \mu_0(N))^2 + (\hbar\gamma_0(N)/2)^2} \tag{3.44}$$

This ansatz assumes that the important modifications arise due to the interaction in

the resonator, and the nonlinear effects outside the double barrier can be neglected. This is justified near a resonance with a small decay rate and correspondingly with a high density inside the double barrier. The open question is now the calculation of the dependence of the density N on the chemical potential μ and the incoming current j_{in}. In the linear case it can be shown that the density is given by [73]:

$$N = \frac{\hbar\gamma_0/2}{(\mu-\mu_0)^2 + (\hbar\gamma_0/2)^2}\ \hbar j_{in} \tag{3.45}$$

In order to account for the nonlinearity in the above equation the resonance energy and the decay rate depend again on the density itself. Therefore we have to solve the resulting equation self-consistently:

$$N = \frac{\hbar\gamma_0(N)/2}{(\mu-\mu_0(N))^2 + (\hbar\gamma_0(N)/2)^2}\ \hbar j_{in} \tag{3.46}$$

Since we want to compare the new formulas Eq. 3.44 and Eq. 3.46 in the nonlinear regime with the stationary solution of the Gross-Pitaevskii equation shown in Fig. 3.7, we need the density dependent resonance energy and decay rate:

This information can be extracted now from the corresponding decaying quasi bound state [75–78]. We choose the method of time integration of the Gross-Pitaevskii equation with density renormalization. To this end we perform a numerical simulation of the time-dependent Gross-Pitaevskii equation without source term. Instead of this we use a Gaussian wave packet in the double barrier as initial condition for the propagation process close to the resonance state. After each propagation step we renormalize the wave function to the density N in the resonator according to:

$$N = \int_{-L/2}^{L/2} |\Psi(x)|^2\, dx \tag{3.47}$$

With this description convergence to the energetically lowest quasi bound state is realized with the normalization N (see Fig. 3.8 a). Finally we extract the energy of the quasi bound state by:

$$\mu_0(N) = \frac{1}{N}\ \int_{-L/2}^{L/2} dx\ \Psi^*(x)\left(-\frac{\hbar}{2m}\frac{\partial^2}{\partial x^2} + V(x) + \tilde{g}|\Psi(x)|^2\right)\Psi(x) \tag{3.48}$$

The decay rate of the quasi bound state is given by:

$$\gamma_0(N) = -\frac{\Delta N}{N\tau}\ , \tag{3.49}$$

where ΔN is the change of the density during the integration by a time step τ. The results are shown in Fig. 3.8 b and c. With this information that the intensity is

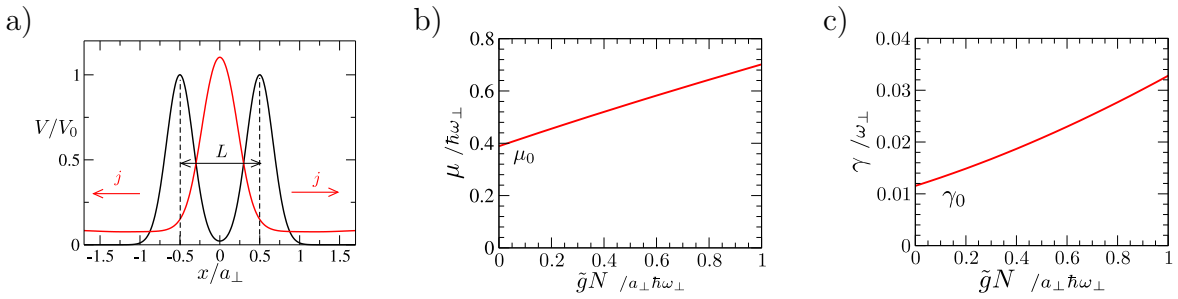

Figure 3.8: a) The black line shows the double barrier potential. The red line (in arbitrary units) shows the density of the wave function of the decaying quasi bound state, which is obtained by time evolution with density renormalization in the resonator. Absorbing boundaries are at the left and right boundary of the simulation region. b) Resonance energy depending on the intensity. c) Decay rate depending on the intensity.

dependent on the resonance energy and decay rate we can solve the equations Eq. 3.44 and Eq. 3.46 self-consistently, and obtain the related transmission spectrum from the information of the decay problem. The results are shown in Fig. 3.9. The solid line shows the transmission received from the information of the decaying state. The dotted line shows the stationary solutions of the Gross-Pitaevskii equation. For the methods used to solve the stationary Gross-Pitaevskii equation see Ref. [65, 73]. The good agreement - besides a small overestimation of the line width for higher nonlinearity - shows the one to one correspondence between nonlinear scattering states and nonlinear resonances. Especially it reveals the bistability phenomenon.

With the density depending on the resonance energy we can now provide an inter-

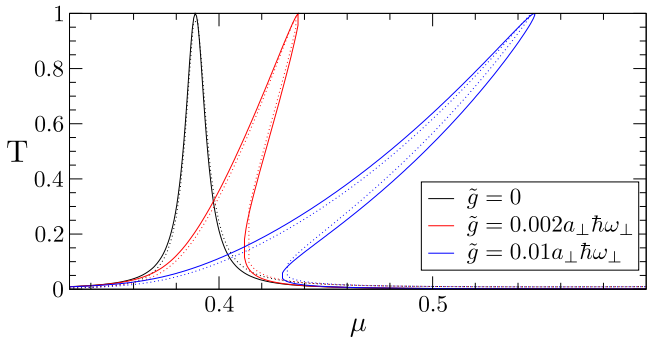

Figure 3.9: The dotted line shows the transmission corresponding to all stationary solutions of the stationary Gross-Pitaevskii equation for a fixed incident current (see Ref. [65, 73] for the methods used). The solid line shows the transmission calculated from the density dependent resonance energy and decay rate for the corresponding quasi bound state.

pretation, why only the lowest transmission state is populated in the time-dependent transmission process with source (see solid line in Fig. 3.7). To illustrate this let us consider a nonlinearity strength and a chemical potential of the incoming wave, where a bistability exists near the nonlinear resonance. Since the starting point of the time-dependent integration is an empty wave guide we are in the low density regime or, similarly expressed, in the almost linear case, which implies that the incoming wave is off-resonance. To this end no high density in the resonator can build up and the high transmitting state can not be realized. Because of this a necessary condition to populate the high transmitting state is an initial high density in the double barrier. This can for example be realized by an adiabatic increase of the chemical potential, from the linear resonance energy to the nonlinear resonance energy.

If the high transmitting state is populated in this way it is found that this state is dynamically unstable [69] and decays over a characteristic time to the low transmitting state. This extracted information is a further advantage of the time-dependent approach to the Gross-Pitaevskii equation, namely that we can extract information about the dynamic stability of stationary solutions.

3.8.2 Multiple slit interference

Now we can go on to a truly two-dimensional system. We investigate the transmission through a double slit and through an array of slits. In the latter example our numerical setup is perfectly suited, because in y-direction we have already periodic boundary conditions, and therefore we can restrict the calculation to a single slit. Treating the problem this way leads to a result which is already correct for an infinitely large array of slits. The setup is shown in Fig. 3.10 where the slit has a width of 2λ and the slits are separated by 6λ. The source emits a wave travelling perpendicular to the barrier. The barrier is chosen to have a finite height $V_0 = 5\mu$. The density plot of the final stationary solution is shown with white color referring to high intensity and black color to zero intensity. In the lower panel the stationary wave function is Fourier transformed in y-direction and the intensity of the wave function for the k_y modes are shown. The black line refers to the wave vector $k_y = 0$. At the left side one can see the typical interference pattern of the incoming and reflected wave for this mode, whereas for all other modes there is no interference pattern. Only at the barrier scattering into higher modes occurs and somewhere else away from the barrier no scattering is possible. Therefore we just have the zero mode and plane outgoing waves in all the higher modes to the right side. One can also see the perfect numerical symmetry in y-direction between the wave vectors $+k_y$ and $-k_y$. Near the barrier one can also observe higher k_y modes which go exponentially to zero when approaching the boundaries. In these cases k_y is so large that k_x needs to be imaginary to preserve the energy-momentum relation $\mu = \frac{\hbar^2}{2m}(k_x^2 + k_y^2)$.

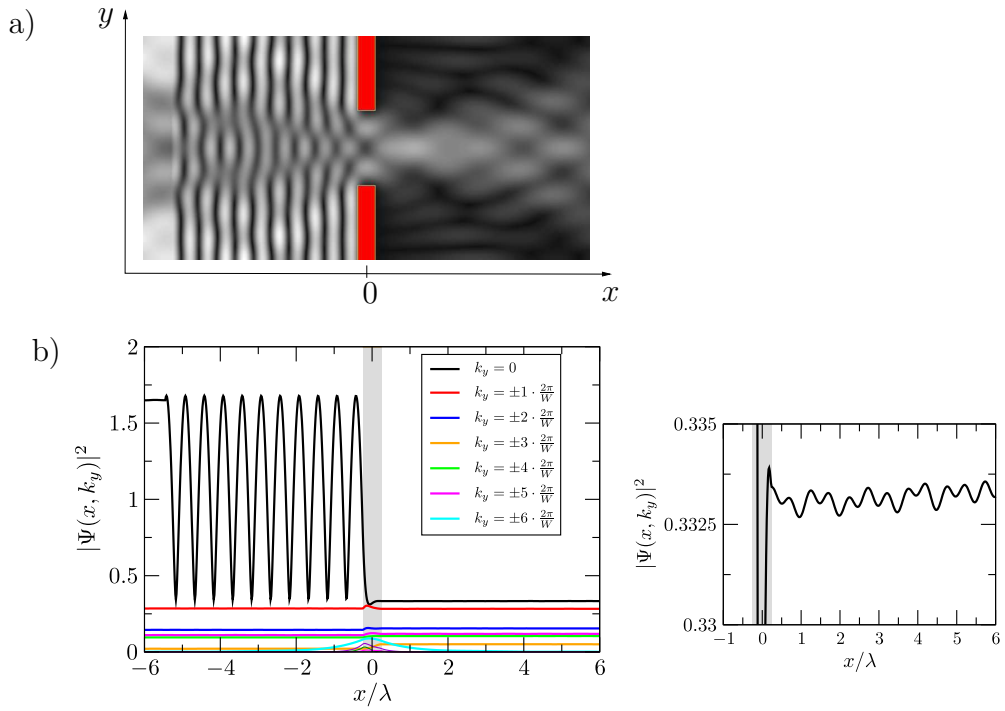

Figure 3.10: The setup is shown in the upper picture, where the slit has a width of 2λ and the slits are separated by 6λ. The source emits a wave travelling perpendicular to the barrier. The barrier is chosen to have a finite height $V_0 = 5\mu$. The density plot of the final stationary solution is shown with white color referring to high intensity and black color to zero intensity. In the lower panel the stationary wave function is Fourier transformed in y-direction and the wave function for the k_y modes are shown. The lower right graph is a high zoom to the outgoing mode $k_y = 0$, which illustrates the small errors from the absorbing boundaries.

The straight line of the intensity is also an excellent demonstration for the absorbing boundaries in two dimensions. The fact that there is no interference pattern shows the high precision of the absorbing boundaries. In the lower right graph of Fig. 3.10 a zoom into the $k_y = 0$ mode of the intensity of the wave function is shown. One can see tiny oscillations with a periodicity of the wave length. This corresponds to reflections from the boundaries. From the height of this oscillations we estimate the artificial back reflection to be less then 0.25%. In the rest of the calculation we keep the quality of the back reflection to be lower then 1%.

As a special case we want to mention the double slit as a well-known and often discussed problem: The setup is analog to the setup of the multiple slit problem. The slits in this example have a width of λ and are separated by 3λ. The finite height of the barrier is chosen as $V_0 = 5\mu$. One analytical result of the intensity at $x = x_0$ is shown in Fig. 3.11 with a black dashed line. It is shaped like a squared sine wave. The

result is calculated by summing up all incoming wave amplitudes with different wave vectors and then being squared. It is assumed that the incoming wave amplitudes are sinusoidal in the slit. This can be done, because the barrier is long enough (length is $\lambda/2$) to make the waves passing the slit be standing waves, supposed to be in the ground state. The second analytical result shown as blue dotted line in the same figure is analog to the first one but with the wave amplitudes passing the slit being taken from the numerical calculation. In this way it can be seen that the deviations arise not from numerical errors, but can be explained by using the correct intensity distribution at the slit.

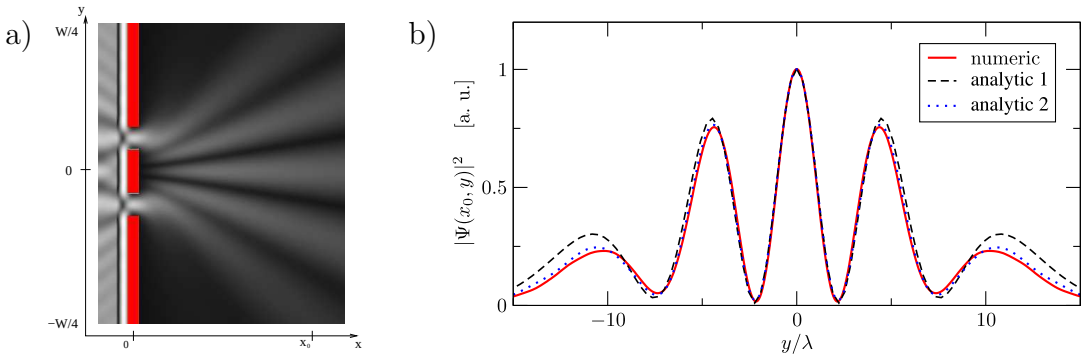

Figure 3.11: The setup is analog to the setup in Fig. 3.10. The slits in this example have a width of λ and are separated by 3λ. The finite height of the barrier is $V_0 = 5\mu$. In the right panel the intensity at $x = x_0$ is shown. The red line shows the result of the numerical calculation, the black dashed line shows the analytic calculation with the incoming wave at the slit assumed to be in the ground state, that means to be sinusoidal, and the blue dotted line shows the analytic calculation with the values of the amplitudes of the incoming wave at the slit taken from the numerical calculation

CHAPTER 4

Transport in disorder potentials

In this chapter we discuss the properties of disorder potentials and the transport process in such potentials. In experiments with Bose-Einstein condensates the disorder can originate for example from imperfection of the experimental setup. In one-dimensional waveguides manufactured with magnetic fields which are created with wires on a micro fabricated chip the imperfections in the wires result in inhomogeneous magnetic fields [19, 21–23]. Therefore this mechanism imposes a disorder potential on the waveguide. On the other hand disorder potentials can be created on purpose to investigate for example the transition to Anderson localization [26–29]. The most evolved technique for creating disorder potentials in Bose-Einstein condensate experiments is to shine a laser beam onto a diffuse plate and image the resulting speckle pattern onto the experimental region. This method results in a speckle field [31].

First we discuss the properties of the disorder potentials, and then we study the important length scales, namely the scattering mean free path and the transport mean free path. The latter one is given by the Boltzmann transport path in the diffusion approximation. When approaching the quantum regime interference effects cannot be neglected and the transport length has to be corrected by coherent multiple scattering. In this chapter we neglect the atom-atom interaction within the Bose-Einstein condensate. This allows to compare with an analytic theory where the correlations of the disorder potential are taken into account. A further justification to neglect atom-atom interaction here is given later on in chapter 5, where coherent backscattering is treated. There we show that the intensity distribution in the medium is unchanged in lowest order of the interaction strength. Only the coherent multiple scattering effects are modified due to the atom-atom interaction.

In the following we focus on the transport of a Bose-Einstein condensate through a disorder potential. Therefore it is necessary to explain the principal setup of the simulated system: A coherent flow of a Bose-Einstein condensate enters the simulation region via the inhomogeneous source term added to the Gross-Pitaevskii equation. Then the condensate scatters on a slab of disorder potential. We assume this disorder potential to be Gaussian correlated or to be a speckle potential. To simulate an infinite slab we use periodic boundary conditions at the transverse boundaries. Finally the condensate reaches the left or right boundary, where it gets absorbed.

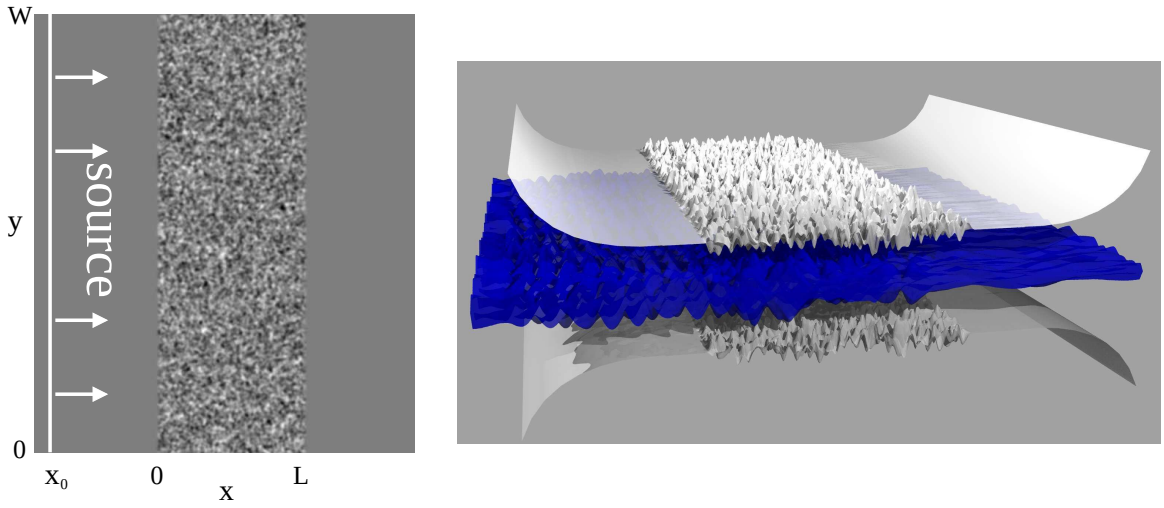

Figure 4.1: A coherent flow of a Bose-Einstein condensate enters the simulation region via the coupling with the source term. Then the condensate scatters on a slab of disorder potential. To simulate an infinite slab we use periodic boundary conditions at the transverse boundaries. Finally, the condensate reaches the left or right boundary, where it gets absorbed. The left panel shows a top view and the right panel a side view where the white plane corresponds to the potential and the condensate wave function is illustrated in blue.

4.1 Correlated disorder potentials

In Bose-Einstein condensate experiments the disorder potential can be created by optical means. In this case the shortest length scale is the wave length of the laser beam. Therefore the correlation length which gives the typical width of the disorder peak is usually in the order of $\sigma \approx 1\mu m$. On the other hand the size of the Bose-Einstein condensate is usually in the order of $d \approx 100\mu m$. This size implies a width $\Delta k \approx 1/d$ of the wave vector distribution, which in turn limits the maximal wavelength $\lambda \ll 1/\Delta k = d$ of the moving condensate in order to have condensate with a relative narrow momentum width. Therefore, it is not possible to consider a priori the disorder potential

as δ-correlated, and we have to account for a finite correlation length. In this work we consider two cases of disorder potentials: Gauss-correlated disorder potentials and speckle disorder potentials.

4.1.1 Gauss-correlated disorder potentials

In the following we consider a disorder potential which has a two-point correlation function of Gaussian shape:

$$\overline{V(\mathbf{r})V(\mathbf{r}')} = \mathcal{P}(\mathbf{r}-\mathbf{r}') = V_0^2 \mathrm{e}^{-\frac{|\mathbf{r}-\mathbf{r}'|^2}{2\sigma^2}}, \tag{4.1}$$

$$\overline{V(\mathbf{r})} \equiv 0, \tag{4.2}$$

where V_0 is the strength of the disorder potential and σ is the correlation length. A correlation energy of $E_\sigma = \frac{\hbar^2}{2m\sigma^2}$ is then related to this correlation length. For convenience, we consider a disorder potential with vanishing mean. Additionally, we assume that the disorder potential arises from a Gaussian random process. This implies that every $2N$-point correlation function can be expressed in terms of two-point correlation functions:

$$\overline{V(\mathbf{r}_1)V(\mathbf{r}_2)..V(\mathbf{r}_{2N-1})V(\mathbf{r}_{2N})} = \sum_P \overline{V(\mathbf{r}_{P(1)})V(\mathbf{r}_{P(2)})} \cdot ... \cdot \overline{V(\mathbf{r}_{P(2N-1)})V(\mathbf{r}_{P(2N)})} \tag{4.3}$$

Furthermore $(2N-1)$-point correlation functions vanish.

Such a Gauss-correlated disorder potential is analytically much easier to treat than a speckle potential which is discussed below. To this end it also allows us to compare the results with an analytical description in the nonlinear regime in the next chapter about coherent backscattering. From the experimental point of view the Gauss-correlated disorder potential is more difficult to implement, because with an optical setup a speckle potential is created. But the Gauss-correlated disorder potential can also be seen as an approximation to the speckle potential or other correlated disorder potentials. For a small enough correlation length the details of the correlation function are not that important and the true correlation function can be approximated by a Gaussian one.

The numerical implementation requires a method to create a potential with such properties. To this end we create a random number with a Gaussian probability distribution $P(a_{ij})$ on the numerical grid on each lattice point. Then we convolute these

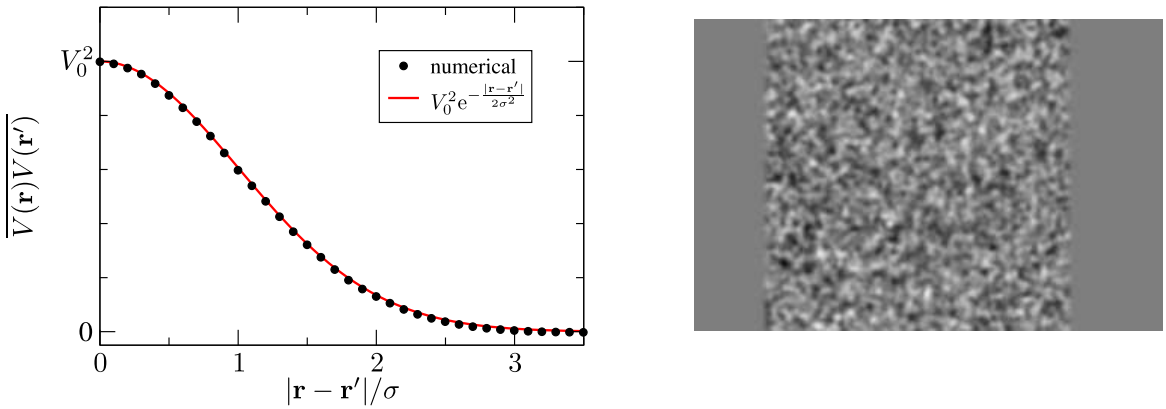

Figure 4.2: Comparison of the potential correlation function of the numerically generated disorder potentials with the analytical prediction. In the right figure a density plot of a typical disorder realization is shown.

random numbers with a Gaussian envelope:

$$V(\mathbf{r}) = \int d\mathbf{r}' \mathcal{V}(\mathbf{r}') \frac{1}{N_x N_y} e^{-\frac{|\mathbf{r}-\mathbf{r}'|^2}{2\sigma^2}} \tag{4.4}$$

$$\mathcal{V}(\mathbf{r}) = \sum_{ij} a_{ij} \delta(\mathbf{r} - \mathbf{r}'_{ij}) \qquad \text{with} \quad \mathbf{r}_{ij} = (id_x, jd_y) \tag{4.5}$$

$$P(a_{ij}) = \frac{1}{V_0\sqrt{2\pi}} e^{-\frac{a_{ij}}{2V_0^2}} \tag{4.6}$$

where i and j are the lattice points, d_x and d_y the lattice spacing in x and y-direction. V_0 is the strength of the disorder potential and σ is the correlation length. The normalization factors N_x and N_y are given by:

$$N_\alpha^2 = \sum_i e^{-\frac{2d_\alpha^2}{\sigma^2} i^2} \approx \frac{\sigma\sqrt{2\pi}}{2d_\alpha}, \tag{4.7}$$

with $\alpha = x, y$. In Fig. 4.2 a density plot of a typical disorder realization is shown. In the left graph we compare the disorder averaged correlation function of the numerically generated configurations (about 1000 disorder potentials) and the analytical prediction, and we see a very good agreement.

In the following numerical analysis we consider the transport of a Bose-Einstein condensate through a slab of disorder. Therefore we have an interface between the disorder region and the outside with a flat potential. Numerically the interface is created by restricting the primary lattice which is filled with the random numbers to the disorder region. Then we apply the convolution. This means that the crossover between flat potential and disorder takes place on a distance of the correlation length.

4.1.2 Speckle potentials

The speckle potential is the disorder potential which is most often used in Bose-Einstein condensate experiments [26–29, 31], because it can be produced in the easiest way. One shines a laser beam on a diffuse plate with radius R and images the resulting interference pattern onto the experimental region located at a distance z away from the diffuse plate. The two-dimensional condensate is in the plane perpendicular to the optical axis like it is shown in Fig. 4.3. After the diffusive plate, which is rough on the scale of the optical wavelength, the electrical field is a superposition of many coherent partial waves. Due to the irregular scattering positions the phase of these partial waves is distributed randomly. Therefore the real and imaginary part of the electrical field have Gaussian statistics. However, the speckle potential does not obey Gaussian statistics, because the interaction of the laser field with the atoms of the Bose-Einstein condensate depends on the intensity of the electrical field and the absolute square of a Gaussian random field loses its Gaussian properties. The correlation function of a speckle field is given by [79, 80]:

$$\overline{V(\mathbf{r})V(\mathbf{r}')} = V_0^2 \left[1 + \left(2\frac{J_1(|\mathbf{r}-\mathbf{r}'|/\sigma)}{|\mathbf{r}-\mathbf{r}'|/\sigma} \right)^2 \right] \tag{4.8}$$

Here J_1 denotes the first order Bessel function. V_0 is the strength of the disorder potential which is proportional to the laser intensity. The correlation length is given

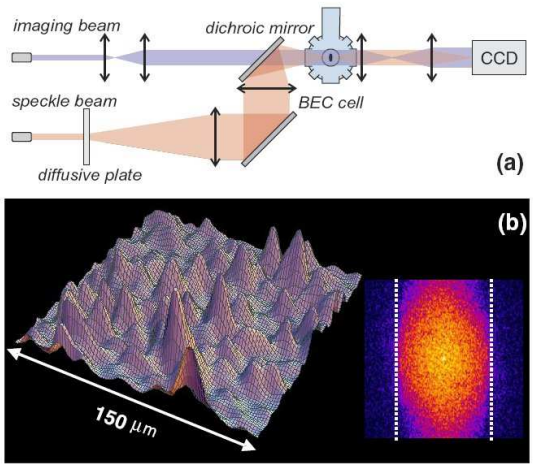

Figure 4.3: Optical setup as it was used in the experiment by J. E. Lye, et al.. A laser illuminates a diffusive plate. The resulting interference pattern is then imaged onto the region of the condensate. The lower left figure shows the speckle potential in real space and its Fourier transform in the lower right figure. (The picture is taken from Lye, et al.[31].)

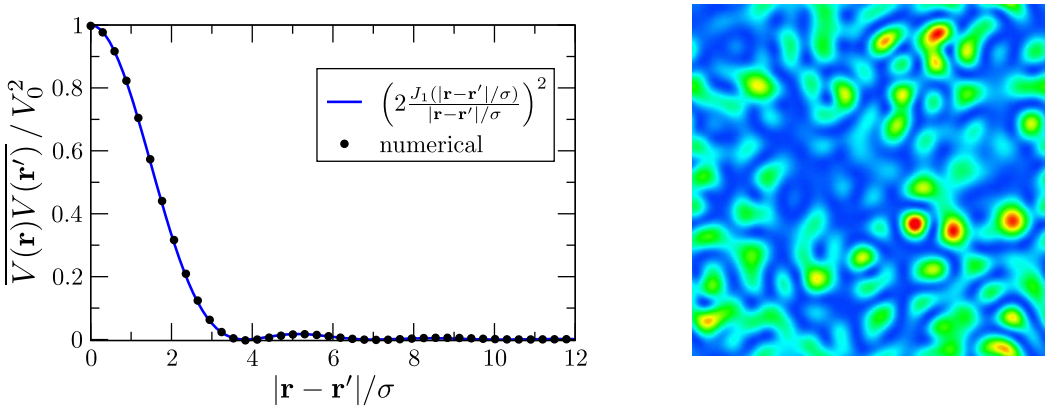

Figure 4.4: Comparison of the potential correlation function of the numerical generated disorder potentials with the analytical prediction. In the right figure a density plot of a typical disorder realization is shown. As explained in the text the speckle potential is asymmetric, because the intensity has a lower bound, but no upper threshold. There are more regions with low intensity (blue regions) and less high intensity spots (red spots).

by $\sigma = \frac{z}{Rk_L}$, where R is the radius of the diffusive plate, z is the distance between diffusive plate and condensate, and k_L is the wave vector of the laser beam [80]. Note that here we have chosen the same definition for the correlation length σ as in the literature [81]. This is a natural definition, since the speckle potential has a cut-off in momentum space $k_{max} = 1/\sigma$ (see below for discussion), which results in a width of the correlation function of $\sqrt{2}\sigma$, in contrast to a width of σ in our definition of the Gauss correlated disorder potential. In the same line we define the correlation energy in the case of the speckle potential as $E_\sigma = \frac{\hbar^2}{m\sigma^2}$. In the following we neglect the offset of V_0^2 from the correlation function which corresponds to setting the mean value to zero $\overline{V(\mathbf{r})} = V_0 \rightarrow \overline{V(\mathbf{r})} = 0$. This potential offset V_0 can be neglected, because it can be trivially separated in the Schrödinger equation.

Numerically a speckle potential is generated in the following way [80, 82, 83]: We start from the potential in the Fourier space $V(k_x, k_y)$. Then we choose random variables for the real and complex part at the positions of the numerical grid with a Gaussian probability distribution, but only at lattice points with $k = \sqrt{k_x^2 + k_y^2} < \frac{1}{\sigma} = k_{max}$. Finally, we apply a Fourier transformation back to position space resulting in a random electrical field. To get the intensity we take the absolute square of the electrical field. This method results in a speckle correlated disorder potential with the above correlation function.

Here we already recognize that the speckle potential has a finite support in the k-space with a maximal wave vector k_{max}. As a consequence the localization length for Anderson localization diverges in Born approximation. For a propagating wave with

$k > k_{max}$ this implies that it localizes on very large length scales.

Furthermore, we note that the speckle potential is not symmetric with respect to the mean value $\overline{V(r)}$. This is plausible, since intensity has a lower bound, but no upper threshold. Therefore the three-point correlation function $\overline{V(\mathbf{r})V(\mathbf{r}')V(\mathbf{r}'')} \neq 0$ does not vanish, in contrast to the Gaussian correlated disorder potential.

For our further studies of the transport through a two-dimensional slab geometry we have to define the interface between the disorder region and the flat potential. To this end we create a disorder potential in the whole simulation region, and multiply this potential with an envelop function $f(x)$:

$$f(x) = \frac{1}{4}\left[\tanh\left(\frac{x - x_{min}}{\sigma}\right) + 1\right] \cdot \left[\tanh\left(\frac{-x + x_{max}}{\sigma}\right) + 1\right] \tag{4.9}$$

where x_{min} and x_{max} are the left and right positions of the interface to the disorder. We switch on the disorder potential within the natural length scale of σ.

4.2 Scattering mean free path

In disordered systems the observables differ from realization to realization. Therefore only observables which are averaged over disorder configurations are meaningful. Such a parameter is the scattering mean free path, which denotes the average distance between two scattering events. This scattering mean free path manifests itself in the exponential decay of the disorder averaged complex wave function. It can be calculated in the weak scattering approximation from the imaginary part of the self energy in the effective medium. The real part of the self energy accounts for a change in the refractive index.
In this chapter we study the evolution of the linear system at energy $E = \frac{\hbar^2 k^2}{2m}$ where k is the wave vector which is governed by the Schrödinger equation:

$$\left(-\frac{\hbar^2}{2m}\nabla^2 + V(\mathbf{r})\right)\Phi(\mathbf{r}) = E\,\Phi(\mathbf{r}) \tag{4.10}$$

In the next two sections we follow closely the derivation of R. C. Kuhn, et al.[80, 84] for the diagrammatic Green function approach with correlated potentials and also references [85–88] for general perturbation theory and quantum transport. The retarded/advanced Green function $G^{R/A}(E)$, which describes the evolution of the wave function in a single disorder realization is given by the following Born series:

$$G^{R/A}(E) = G_0^{R/A}(E) + G_0^{R/A}(E)VG_0^{R/A}(E) + G_0^{R/A}(E)VG_0^{R/A}(E)VG_0^{R/A}(E) + \ldots \tag{4.11}$$

where $G_0^{R/A}$ is the retarded/advanced Green function for the free Schrödinger equation with vanishing disorder potential. G_0 is diagonal in momentum space due to the

isotropy of space:

$$\langle \mathbf{k}'|G_0^{R/A}(E)|\mathbf{k}\rangle = (2\pi)^2\delta(\mathbf{k}-\mathbf{k}')\; G_0^{R/A}(k,E) = \lim_{\epsilon\to 0+} \frac{(2\pi)^2\delta(\mathbf{k}-\mathbf{k}')}{E-\frac{\hbar^2k^2}{2m}\pm i\epsilon} \tag{4.12}$$

Since we are not interested in the dynamics of a special disorder potential but in observables which are independent of the disorder configuration, we average the Green function over many different disorder realizations:

$$\overline{G(E)} = G_0(E)+G_0(E)\overline{VG_0(E)V}G_0(E)+G_0(E)\overline{VG_0(E)VG_0(E)V}G_0(E)+... \tag{4.13}$$

The linear term in V disappears, because we have chosen the disorder potential V to have a vanishing mean. This series can formally be summed up to yield the following Dyson equation:

$$\overline{G^{R/A}}(E) = G_0^{R/A}(E) + G_0^{R/A}(E)\;\Sigma^{R/A}(E)\;\overline{G^{R/A}}(E) \tag{4.14}$$

$$\overline{G^{R/A}}(E) = \frac{1}{G_0^{R/A}(E)^{-1}-\Sigma^{R/A}(E)} \tag{4.15}$$

Here we introduced the retarded/advanced self-energy $\Sigma^{R/A}$. In the second equation we solved for the averaged Green function, which is possible, because upon iteration the Dyson equation shows the structure of a geometric series. The self-energy $\Sigma^{R/A}$ contains all irreducible correlation functions. Irreducible correlations cannot be split into products of lower order correlation function by suppressing only a single propagator G_0. This can be visualized by

$\Sigma =$ 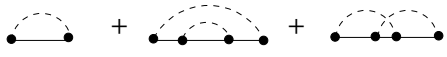 . (4.16)

Due to the disorder average the isotropy in space is restored again and the Green function and the self-energy depend only on the modulus of $k = |\mathbf{k}|$:

$$\overline{G^{R/A}}(k,E) = \lim_{\epsilon\to 0+} \frac{1}{E-\frac{\hbar^2k^2}{2m}-\Sigma^{R/A}(k,E)\pm i\epsilon}\;. \tag{4.17}$$

This leads to the complex dispersion relation $E-\frac{\hbar^2k_E^2}{2m}-\Sigma^R(k_E,E)=0$. The wave vector k_E inside the effective medium is then determined by the refractive index n:

$$k_E = n(E)\,\frac{1}{\hbar}\sqrt{2mE}\;; \tag{4.18}$$

$$n(E) = \sqrt{1-\frac{\Sigma^R(k_E,E)}{E}} \approx 1-\frac{\Re\left[\Sigma^R(k_E,E)\right]}{2E} - i\frac{\Im\left[\Sigma^R(k_E,E)\right]}{2E}\;. \tag{4.19}$$

In principle the two equations have to be solved self-consistently, but very often one uses the on shell approximation, where in Eq. 4.19 on the right hand side k_E is replaced

by the free particle dispersion relation $k_E = \sqrt{2mE}/\hbar$. This approximation and the expansion of the square root in Eq. 4.19 is only valid for weak scattering $\Delta = \frac{V_0^2}{E\,E_\sigma} \ll 1$, where V_0 is the height of the disorder potential and E_σ is the correlation energy. The imaginary part of the refractive index illustrates that an incoming wave gets damped and is therefore scattered into different scattering modes. The strength of the damping is related to the scattering time τ_s by

$$\frac{\hbar}{\tau_s(k_E)} = -2\Im\left[\Sigma^R(k_E, E)\right] \tag{4.20}$$

and to the scattering mean free path ℓ_s by

$$\ell_s(k_E) = \frac{\hbar k}{m}\tau_s(k_E)\ , \tag{4.21}$$

which is the mean distance between two scattering events. We can therefore evaluate the Green function in the on shell approximation, and by neglecting the energy shift due to the real part of the self energy we obtain

$$\overline{G^{R/A}}(k, E) \approx \frac{1}{E - \frac{\hbar^2 k^2}{2m} \pm i\hbar/2\tau_s(k_E)} \tag{4.22}$$

which transforms into position space as

$$\overline{G^{R/A}}(\mathbf{r}, \mathbf{r}', E) \approx -i\tfrac{m}{2\hbar^2}\ \mathcal{H}_0(\pm k_E|\mathbf{r} - \mathbf{r}'|)\ \mathrm{e}^{-|\mathbf{r}-\mathbf{r}'|/2\ell_s(k_E)}\ , \tag{4.23}$$

where $\mathcal{H}_0$ is the zeroth-order Hankel function. By applying the Born approximation which is valid in the regime of $\Delta = \frac{V_0^2}{E\,E_\sigma} \ll 1$ for the self energy, i. e., by cutting the perturbation expansion after the first non-vanishing diagram in Eq. 4.16 we arrive at the following expression for the self energy:

$$\Sigma_B^{R/A}(k, E) = \int \frac{d\mathbf{k}_1}{2\pi}\mathcal{P}(\mathbf{k} - \mathbf{k}_1)G_0^{R/A}(k_1, E) \tag{4.24}$$

where $\mathcal{P}(\mathbf{k})$ is the Fourier transform of the correlation function $\mathcal{P}(\mathbf{r})$ from Eq. 4.1. Now we use the fact that the imaginary part of the free Green function is a Delta function in momentum space and the definition $\mathcal{P}(k, \theta) = \mathcal{P}(k\hat{\mathbf{k}} - k\hat{\mathbf{k}}')$, where $\hat{\mathbf{k}}$ is a unit vector in the direction of $\mathbf{k}$. By combining Eq. 4.20, Eq. 4.21 and Eq. 4.24 we end up with the final expression for the scattering mean free path ℓ_s in Born approximation in two-dimensional systems [81]:

$$\frac{1}{k\ell_s(k)} = \frac{m^2}{k^2\hbar^4}\ \int_0^{2\pi} \frac{d\theta}{2\pi}\ \mathcal{P}(k, \theta)\ . \tag{4.25}$$

With this expression it is possible to insert an arbitrary correlation function for the disorder type, for example for the Gauss correlated disorder and the speckle disorder.

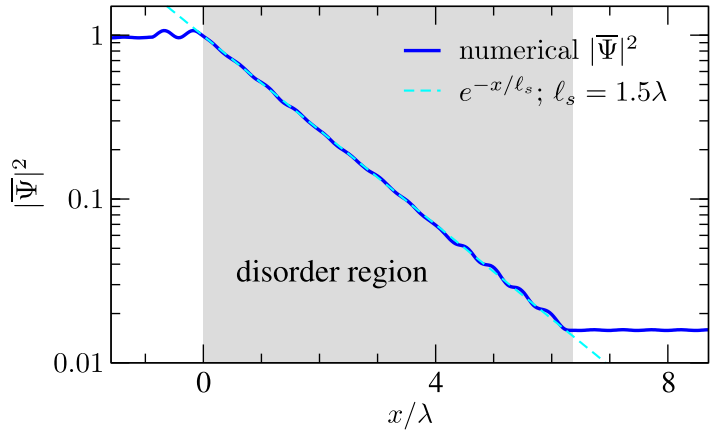

Figure 4.5: The coherent mode $\left|\overline{\Psi(x)}\right|^2$ averaged over ~ 700 disorder configurations along the propagation direction x is shown. It decays exponentially with the scattering mean free path ℓ_s. The dashed line shows the fitted exponential which is in very good agreement with the numerical calculation. A scattering mean free path of $\ell_s = 1.5\lambda$ is extracted. Parameters: $kL = 40$, $k\sigma = 0.5$, $V_0 = 0.614\mu$, $k = \sqrt{2m\mu}/\hbar$.

Gauss correlated disorder potential

Now we consider the special case of a Gauss correlated disorder potential, which has a Gaussian correlation function (Eq. 4.1):

$$\mathcal{P}(\mathbf{r}-\mathbf{r}') = \overline{V(\mathbf{r})V(\mathbf{r}')} = V_0^2 \mathrm{e}^{-\frac{|\mathbf{r}-\mathbf{r}'|^2}{2\sigma^2}} \ . \tag{4.26}$$

We insert the Fourier transformed correlation function, which is again a Gaussian, into Eq. 4.25. In the Born approximation the scattering mean free path reduces to

$$\frac{1}{k\ell_s} = \frac{\pi}{2}\,\frac{V_0^2}{E^2}\,(k\sigma)^2\, I_0(k^2\sigma^2)\, \mathrm{e}^{-k^2\sigma^2}, \tag{4.27}$$

where I_0 is the modified Bessel function of order zero and $k = \sqrt{2mE}/\hbar$. The scattering mean free path as a function of the disorder strength V_0 is shown in Fig. 4.6 for two correlation lengths. In the left graph $k\sigma = 0.5$ is used which corresponds to almost isotropic scattering, whereas in the case $k\sigma = 1.0$ scattering in forward direction is strongly enhanced compared to scattering in backward direction.

In order to compare Eq. 4.27 to our simulation we have to extract the scattering mean free path from the numerical wave functions. The setup for our numerical studies is shown in Fig. 3.1. A coherent flow of condensate with chemical potential $\mu = \frac{\hbar^2 k^2}{2m}$ approaches perpendicularly the disorder region. (In the numerical setup we usually use the term chemical potential as a synonym for the energy $E = \frac{\hbar^2 k^2}{2m}$, because the origin

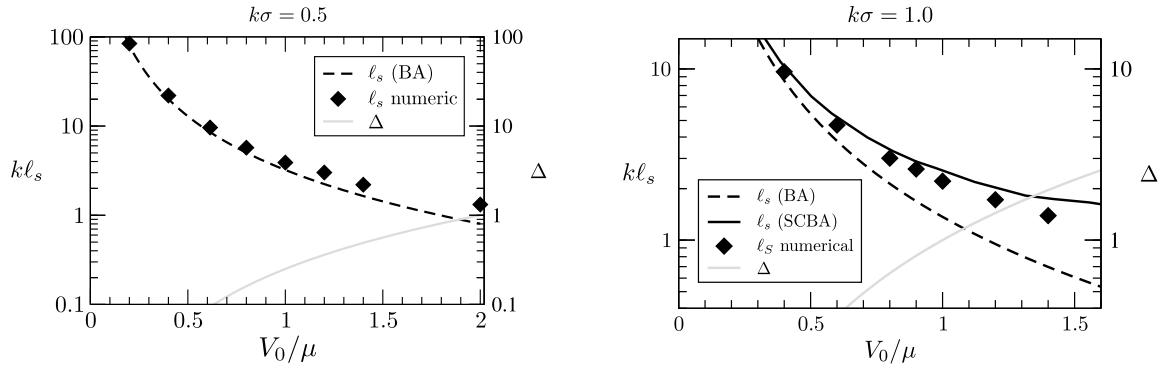

Figure 4.6: Comparison of the numerically extracted scattering mean free path (points), and the analytical results in the Born approximation (BA, dashed line) for Gauss correlated disorder potentials. This is shown for the correlation length $k\sigma = 0.5$ (left graph), where almost isotropic scattering is effective, and for $k\sigma = 1.0$ with anisotropic scattering. We observe good agreement in the weak scattering limit $\Delta = \frac{V_0^2}{E\,E_\sigma} \ll 1$ with $E_\sigma = \frac{\hbar^2}{2m\sigma^2}$, whereas we find a deviation of a factor 2 at $\Delta \approx 1$. The deviations can be explained for $k\sigma = 1.0$ by higher order approximation, the self consistent Born approximation [89].

of the propagating wave is a reservoir of condensate with a chemical potential μ.) In the transverse y-direction we have periodic boundary conditions, so that we have translational invariance in y-direction for the observables such as the coherent mode or the intensity after the disorder average is performed. As soon as the wave has entered the disorder region, the coherent mode $\left|\overline{\Psi(x)}\right|^2$ (the absolute value is taken *after* the average in contrast to the intensity $\overline{|\Psi(x)|^2}$) according to Eq. 4.23 is exponentially damped with the scattering mean free path. This is shown in Fig. 4.5, where we see an excellent agreement with an exponential fit. The oscillation in front of the disorder medium and at the end of the medium are not numerical or statistical effects, but are due to reflection at the boundary due to a change of the refractive index and will be discussed later on. In Fig. 4.6 we compare the extracted scattering mean free path with the analytical predictions. In the weak scattering regime $\Delta = \frac{V_0^2}{E\,E_\sigma} \ll 1$ where the diagrammatic perturbation theory is valid we observe good agreement between the analytical results (dashed line) and the numerical results (points). However, for larger $\Delta \approx 1$ we already see a significant deviation by approximately a factor of two. Sometimes [81] the validity of the Born approximation is assumed up to $\Delta \approx 1$, especially in the context of strong localization. The importance is due to the fact that the localization length is strongly underestimated in this case. The localization length ξ_{loc} gives the length scale of the exponential decay of the wave function in the regime of Anderson localization (strong disorder). The localization length is given by $\xi_{loc} = \ell_B \exp(\frac{\pi}{2} k\ell_B)$ [84], where ℓ_B is the Boltzmann transport mean free path which is identical with the scattering mean free

path in the case of isotropic scattering. The transport mean free path is discussed in the next section. Since the localization length is exponentially dependent on the mean free path small deviations in the scattering mean free path result in large deviations of the localization length. In order to demonstrate that the deviations are related to the breakdown of the Born approximation we compare our results to the scattering mean free path in the self-consistent Born approximation (SCBA) calculated by C. A. Müller [89], shown in the right graph of Fig. 4.6, where we observe a much better agreement with the numerical results than for the Born approximation.

As already mentioned earlier we observe oscillations in the coherent mode in front of the disorder region and also at the end of the disorder region in our numerical simulation. These are no numerical errors or statistical fluctuations, but they are due to the reflection at the disorder boundary. As seen in Eq. 4.19 the self-energy also modifies the real part of the refractive index $n = \sqrt{1 - \frac{\Re[\Sigma(E)]}{E}}$. Due to this index mismatch between the free part and the disorder region one observes specular reflection at the interface [67]:

$$R = \left(\frac{1-n}{1+n}\right)^2 . \tag{4.28}$$

The real part of the self energy for Gaussian disorder can be calculated in the Born approximation yielding the following result [90]:

$$\Re\left[\Sigma_2(k,E)\right] = -\frac{m\sigma V_0^2}{\sqrt{2}\hbar^2 k}\mathrm{e}^{-2k^2\sigma^2}\int_0^\infty dv\ \frac{\mathrm{e}^{-v}}{\sqrt{v}\sqrt{1+\frac{v}{2k^2\sigma^2}}}. \tag{4.29}$$

Additionally, we can extract the reflected intensity from our numerical data. We assume to have a superposition of an incoming plane wave with amplitude α and a reflected wave with amplitude β: $\psi = \alpha\mathrm{e}^{ikx} + \beta\mathrm{e}^{-ikx}$. The intensity pattern is then described by

$$|A|^2 = \alpha^2 + \beta^2 + 2\alpha\beta\cos(2kx). \tag{4.30}$$

We fit this function to our coherent mode in front of the disorder region and extract the amplitudes α and β, which results in the numerical reflection coefficient $R = \frac{\alpha^2}{\beta^2}$. In Fig. 4.7 a comparison between the analytical results (solid line) and the numerical data (points) is shown. The good agreement confirms our explanation at least for not too large disorder strengths where the analytical result is applicable.

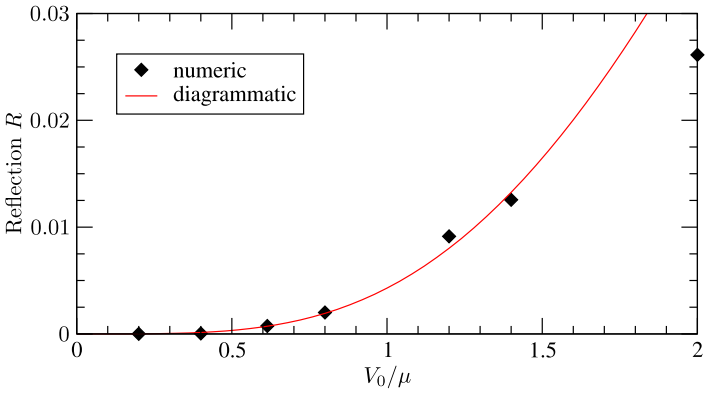

Figure 4.7: Comparison of the reflection at the disorder interface due to the refractive index mismatch between the analytical result in Born approximation (solid line) and the numerical data (points).

Speckle disorder potential

Now we consider the case of a speckle potential which is described by the correlation function Eq. 4.8:

$$\mathcal{P}(\mathbf{r}-\mathbf{r}') = \overline{V(\mathbf{r})V(\mathbf{r}')} = V_0^2 \left(2\frac{J_1(|\mathbf{r}-\mathbf{r}'|/\sigma)}{|\mathbf{r}-\mathbf{r}'|/\sigma} \right)^2 . \tag{4.31}$$

Within the Born approximation all higher order correlation functions are neglected, like the three point correlation function, which vanishes in the Gaussian correlated disorder, but not in the speckle potential. The Fourier transformation of this correlation function can be calculated to yield [84]:

$$\mathcal{P}(\mathbf{k}) = \frac{8V_0^2}{\sigma^2} \left[\arccos\left(\frac{k}{2\sigma}\right) - \frac{k}{2\sigma}\sqrt{1-\left(\frac{k}{2\sigma}\right)^2} \right] \theta\left(1-\frac{k}{2\sigma}\right) . \tag{4.32}$$

The scattering mean free path cannot be calculated in closed form, therefore we have to calculate the integral in Eq. 4.25 numerically. A comparison between the diagrammatic approach in the Born approximation (BA) and our numerical calculations are shown in Fig. 4.8 for two different correlation lengths. We observe quite large deviations in the scattering mean free path for intermediate potential strength. The difference is much larger than in the Gauss correlated disorder potential[1]. This slower convergence of the

[1]Note that due to the definition of the correlation length Eq. 4.8 of the speckle potential a correlation length of σ of the speckle potential should be compared with a correlation length $\sqrt{2}\sigma$ of the Gauss correlated disorder potential.

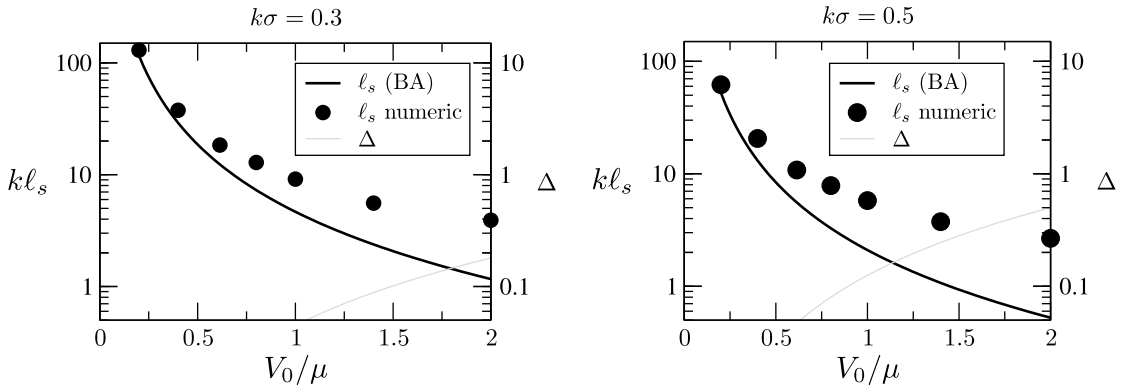

Figure 4.8: Comparison of the numerical extracted scattering mean free path (points), and the analytical results in the Born approximation (BA, solid lines) for speckle disorder potentials. This is shown for the correlation length $k\sigma = 0.3$ where almost isotropic scattering is effective and for $k\sigma = 0.5$ with anisotropic scattering. We observe already significant deviations in the weak scattering limit $\Delta = \frac{V_0^2}{E\,E_\sigma} \ll 1$ with $E_\sigma = \frac{\hbar^2}{m\sigma^2}$.

diagrammatic approach is also expected in the case of the speckle potential. In the Gaussian case there are no diagrams contributing to the self energy which arise from three point correlators. This is different in the speckle potential, where the self energy has an additional contribution from the following third order diagram [84]:

$\Sigma_3 =$ 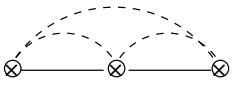 (4.33)

These deviations between our numerical studies and the analytical results are important, especially when the transition to strong localization is considered. Because a change in the scattering mean free path modifies the localization length $\xi_{loc} = \ell_B \exp(\frac{\pi}{2} k\ell_B)$ [84] significantly. The Boltzmann transport mean free path ℓ_b is proportional to the scattering mean free path ℓ_s for fixed $k\sigma$.

4.3 Transport mean free path

In this section we focus on transport processes in disordered systems. Therefore a description of the intensity propagation is necessary, which finally leads to the diffusion equation with the transport mean free path. In the classical limit, where interference effects are neglected, this leads to the Boltzmann transport mean free path. Approaching the quantum regime this transport mean free path has to be adjusted with weak localization corrections due to coherent multiple scattering. We compare our numerical simulations through a slab geometry with disorder to analytical results. In the

diagrammatic approach we present only the main results following the derivation of R. C. Kuhn, et al.[80, 84] and the original work by D. Vollhardt and P. Wölfle [91, 92].

In order to study the averaged current or the average intensity within a disordered medium the intensity propagation kernel $K = \overline{G^A \otimes G^R}$ plays a fundamental role where $G^{R/A}$ is the retarded/advanced Green function in the disorder potential. The matrix elements are given by:

$$K(\mathbf{k},\mathbf{k}',\mathbf{q},E,\epsilon) = \overline{\langle \mathbf{k}' - \tfrac{\mathbf{q}}{2}|G^A(E+\tfrac{\epsilon}{2})|\mathbf{k}-\tfrac{\mathbf{q}}{2}\rangle\langle \mathbf{k}+\tfrac{\mathbf{q}}{2}|G^R(E-\tfrac{\epsilon}{2})|\mathbf{k}'+\tfrac{\mathbf{q}}{2}\rangle} \quad (4.34)$$

$=$

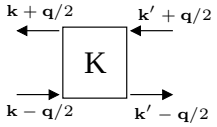

(4.35)

Similarly the matrix elements of the operator $\overline{G^A} \otimes \overline{G^R}$ are given by:

$$\langle \mathbf{k}' - \tfrac{\mathbf{q}}{2}, \mathbf{k} + \tfrac{\mathbf{q}}{2}|\overline{G^A}(E+\tfrac{\epsilon}{2}) \otimes \overline{G^R}(E-\tfrac{\epsilon}{2})|\mathbf{k}-\tfrac{\mathbf{q}}{2}, \mathbf{k}'+\tfrac{\mathbf{q}}{2}\rangle \quad (4.36)$$
$$= (2\pi)^2\, \delta(\mathbf{k}-\mathbf{k}')\overline{G^A}(\mathbf{k},\mathbf{q},E,\epsilon)\overline{G^R}(\mathbf{k},\mathbf{q},E,\epsilon)$$

In the way the average Green function solves the Dyson equation the intensity propagation kernel K solves the Bethe-Salpeter equation:

$$K = [\overline{G^A} \otimes \overline{G^R}] + [\overline{G^A} \otimes \overline{G^R}]\; R\; [\overline{G^A} \otimes \overline{G^R}]\;, \quad (4.37)$$
$$R = U + U\; [\overline{G^A} \otimes \overline{G^R}]\; R. \quad (4.38)$$

Here R is the reducible vertex function and U the irreducible vertex function. A irreducible vertex function cannot be divided into two diagrams by removing a single propagator line.

U =

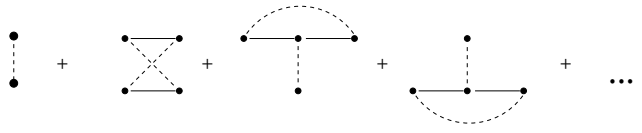

(4.39)

A upper line corresponds to $\overline{G^R}$ and a lower line to $\overline{G^A}$. In order to account also for speckle statistics further building blocks have to be considered. In this case also third order diagrams appear [80], similar to the additional diagram in the self-energy shown in Eq. 4.33:

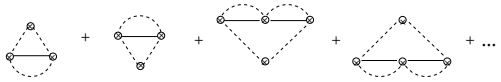

(4.40)

Now one can solve the quantum kinetic equation in the diffusion approximation and in linear response [84, 86, 91]. A central quantity appearing in this derivation is the

Diffusion constant D or the transport time τ, which are related by $D(k) = \frac{\hbar^2 k^2}{2m^2}\tau(k)$. The transport time expressed in terms of the irreducible scattering vertex U is [80]:

$$\frac{\hbar}{\tau(k_E)} = \frac{1}{2\pi N(E)} \int\int \frac{d\mathbf{k}\; d\mathbf{k}'}{(2\pi)^4}(1 - \hat{\mathbf{k}}\cdot\hat{\mathbf{k}}')A(k,E)A(k',E)\; U(\mathbf{k},\mathbf{k}',E), \tag{4.41}$$

where we have defined the spectral function $A(k,E) = -2\Im[\overline{G^R}(k,E)]$ and the density of states $N(E) = \int \frac{d\mathbf{k}}{(2\pi)^3}A(k,E)$. $\hat{\mathbf{k}}$ is again a unit vector in direction $\mathbf{k}$. This expression is quite general. It does not rely on the Boltzmann approximation, because it still contains the general scattering vertex U. From the transport scattering time we define the transport mean free path by $\ell(k) = \frac{\hbar k}{m}\tau(k)$.

In the following we briefly explain the time evolution of a intensity distribution in terms of this Diffusion constant. We consider a point source, which is suddenly switched on and off at $t = 0$. Therefore, we define the diffusive intensity relaxation kernel:

$$\mathcal{K}(\mathbf{k},\mathbf{q},\epsilon) = \int \frac{dE}{2\pi} \int \frac{d\mathbf{k}'}{(2\pi)^2} K(\mathbf{k}',\mathbf{k},\mathbf{q},E,\epsilon). \tag{4.42}$$

This diffusive intensity relaxation kernel can be approximated in the long time limit $\epsilon\tau/\hbar \ll 1$ and large-distance limit $\ell(k)q \ll 1$ to yield:

$$\mathcal{K}(\mathbf{k},\mathbf{q},\epsilon) = \frac{1}{-i\epsilon + \hbar D(k_E)q^2} \quad \text{and} \tag{4.43}$$

$$\mathcal{K}(\mathbf{k},\mathbf{R},t) = \frac{1}{4\pi D(k)t}\mathrm{e}^{-\frac{|\mathbf{R}|^2}{4D(k)t}}. \tag{4.44}$$

In the second equation we applied a Fourier transformation to time and position space. This diffusive intensity relaxation kernel obeys the well known diffusion equation:

$$\frac{\partial}{\partial t}\mathcal{K}(\mathbf{k},\mathbf{R},t) - D(k)\Delta\,\mathcal{K}(\mathbf{k},\mathbf{R},t) = \delta(\mathbf{R})\delta(t), \tag{4.45}$$

where $\mathbf{R} = \mathbf{r} - \mathbf{r}'$. With these definitions the time evolution of the disorder averaged probability density is written in the following way:

$$p(\mathbf{r},t) = \langle\mathbf{r}|\theta(t)\overline{\rho}(t)|\mathbf{r}\rangle = \int \frac{d\mathbf{k}}{(2\pi)^2} \int d\mathbf{r}'\mathcal{K}(\mathbf{k},\mathbf{r}-\mathbf{r}',t)W_0(\mathbf{k},\mathbf{r}'). \tag{4.46}$$

The probability density is expressed in terms of the average atomic density operator $\overline{\rho}(t)$, and the initial density is specified with the corresponding Wigner function $W_0(\mathbf{k},\mathbf{r}') = \int \frac{d\mathbf{q}}{(2\pi)^2}\langle\mathbf{k}' + \frac{\mathbf{q}}{2}|\rho_0|\mathbf{k}' - \frac{\mathbf{q}}{2}\rangle$.

We have introduced a general framework to characterize the transport process in a disordered medium. The diagrammatic perturbation theory allows to calculate the relevant transport observables like the transport mean free path, which in turn allows to calculate the propagation of the diffuse probability density. This approach is still general, because the disorder type has not to be specified yet. Moreover, the scattering vertex is not fixed allowing to include coherent multiple scattering.

4.3.1 Boltzmann transport mean free path

In this subsection we show the independent scattering approximation applied to the transport mean free path, where all effects of interference are neglected and which is called the Boltzmann approximation. The only irreducible diagram which is taken into account is:

$U \approx$  $U(\mathbf{k}, \mathbf{k}', E) \approx \mathcal{P}(\mathbf{k} - \mathbf{k}')$. (4.47)

In order to account for multiple scattering of this type a series of these single scattering events is considered. In the reducible vertex function the considered types of diagrams form a ladder. They are therefore denoted by L. This series of diagrams is also called Diffuson.

$R \approx$ 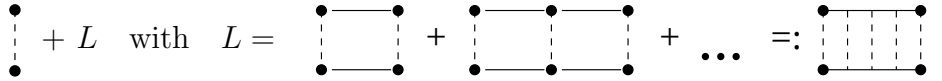 . (4.48)

Considering the wave function it can be interpreted in the following way: The amplitude of a wave which returns to a given point is calculated by summing up all amplitudes ϕ_i corresponding to a scattering path i. Hence the intensity is given by $\overline{|\sum_i \phi_i|^2} = \sum_i \overline{\phi_i \phi_i^*} + \sum_{i \neq j} \overline{\phi_i \phi_j^*}$. For different scattering paths i and j a randomly distributed phase factor appears in the second term, and thus the sum is zero. Only the first term is kept, where the two waves travel along the same scattering path. In this case weak localization corrections are neglected.

Inserting the lowest order diagram, Eq. 4.47, into the general expression for the mean transport time, Eq. 4.41, we find the Boltzmann transport scattering time:

$$\frac{\hbar}{\tau_B(k_E)} = \frac{1}{2\pi N(E)} \int\int \frac{d\mathbf{k}\, d\mathbf{k}'}{(2\pi)^4} (1 - \hat{\mathbf{k}} \cdot \hat{\mathbf{k}}') A(k, E) A(k', E)\, \mathcal{P}(\mathbf{k} - \mathbf{k}') \quad (4.49)$$

$$= \frac{m}{\hbar^2} \int_0^{2\pi} d\theta\, [1 - \cos(\theta)] \mathcal{P}\left(2 k_E \sin(\tfrac{\theta}{2})\right). \quad (4.50)$$

For the spectral function one can use the on-shell approximation, which reduces the spectral function to a delta function. From the Boltzmann transport time we can define the Boltzmann scattering mean free path in the usual way by $\ell_B(k) = \frac{\hbar k}{m} \tau_B(k)$. Combining Eq. 4.50 with the expression of the scattering mean free path in the Born approximation Eq. 4.25 we end up with the final result for the Boltzmann scattering mean free path:

$$\frac{\ell_s}{\ell_B} = 1 - \langle \cos(\theta) \rangle_f = 1 - \int_0^{2\pi} d\theta\ \cos(\theta) f(k, \theta). \quad (4.51)$$

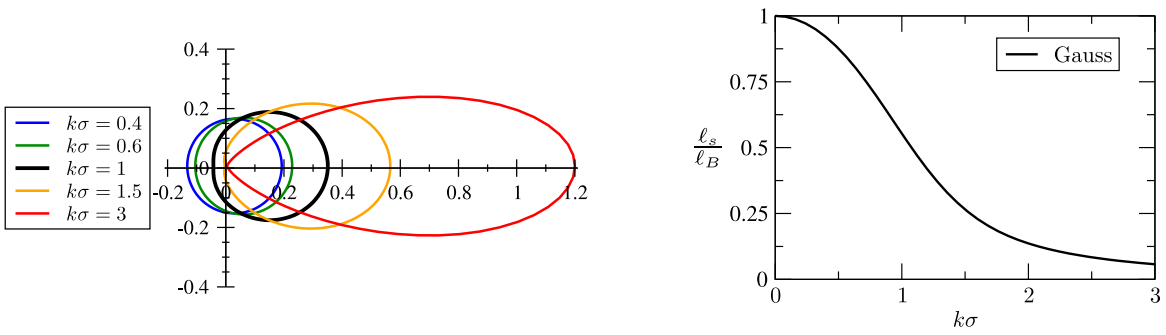

Figure 4.9: In the left graph the phase function for the Gauss correlated disorder potential is shown. Small values of $k\sigma$ correspond to almost isotropic scattering, otherwise scattering in forward direction is enhanced and scattering is less effective. Therefore ℓ_B is larger than ℓ_s, which is shown in the right graph.

Here we have defined the phase function $f(k,\theta)$, which illustrates the scattered intensity into the scattering angle θ:

$$f(k,\theta) = \frac{\mathcal{P}(k,\theta)}{\int_0^{2\pi} d\theta\, \mathcal{P}(k,\theta)}. \tag{4.52}$$

For delta correlated disorder potentials this phase function is constant as a function of the angle, which implies isotropic scattering. Whereas for correlated potentials forward scattering is usually pronounced in comparison to scattering in backward direction.

Gauss correlated disorder potential

Now we concentrate again on the Gauss correlated disorder potential. Analog to the scattering mean free path we can calculate the Boltzmann transport mean free path in closed form:

$$\frac{\ell_s}{\ell_B} = 1 - \frac{I_1(k^2\sigma^2)}{I_0(k^2\sigma^2)} \tag{4.53}$$

where I_j is the modified Bessel function of order j and $k = \sqrt{2mE}/\hbar$. We note that $\ell_B \propto \ell_s$, and that the proportionality factor depends only on the product $k\sigma$. In the case of isotropic scattering, $k\sigma \ll 1$, the two length scales ℓ_s and ℓ_B are identical, whereas in the case of longer correlation lengths forward scattering is enhanced as illustrated in Fig. 4.9. This implies that scattering is less effective and the Boltzmann transport mean free path is always larger than the scattering mean free path. In Fig. 4.14 a comparison to our numerically obtained transport mean free path is presented. It shows very good agreement to the analytical results in the weak scattering regime for

small V_0. For stronger scattering we see a deviation due to weak localization effects. Both this effect and also the way we extract the transport mean free path from the numerical simulation will be discussed below.

Speckle potential

In the case of the speckle potential the Boltzmann transport mean free path cannot be calculated in closed form. Instead we state only analytical expressions for the limiting cases [80]:

$$\ell_B = \frac{\pi^2 - 4}{\pi^2 - 8}\ell_s \qquad k\sigma = 1 \tag{4.54}$$

$$\ell_B \approx \ell_s \qquad k\sigma \ll 1 \tag{4.55}$$

$$\ell_B \approx \frac{15}{4}(k\sigma)^2\ell_s \qquad k\sigma \gg 1 \tag{4.56}$$

In Fig. 4.11 numerical results for the Boltzmann transport mean free path are shown, which are calculated by inserting the speckle correlation function from Eq. 4.8 or Eq. 4.31 into the general expression for the Boltzmann transport mean free path ℓ_B, Eq. 4.51. We extract the transport mean free path from our numerical simulations and find significant deviations like in the case of the scattering mean free path. This is shown in Fig. 4.15.

4.3.2 Diffusion in a slab of finite width

Now we relate the analytical results to our numerical simulation. In the numerical setup we consider a coherent beam propagating along the x-direction towards the disorder

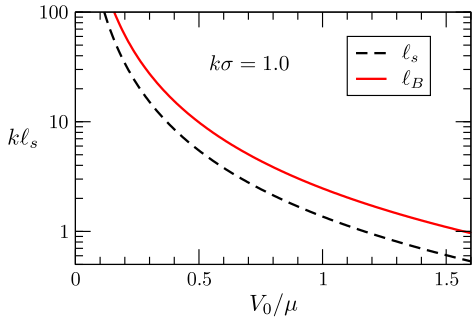

Figure 4.10: Comparison between scattering mean free path and Boltzmann transport mean free path for $k\sigma = 1.0$ for a Gauss correlated disorder potential.

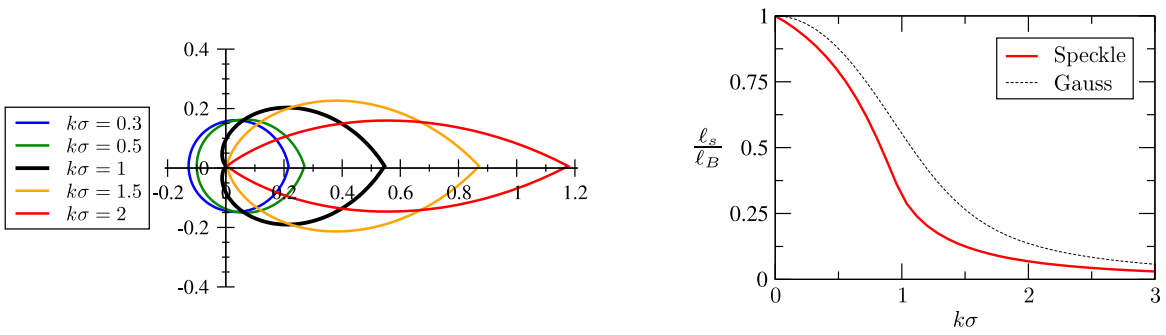

Figure 4.11: In the left graph the phase function for the speckle disorder potential is shown. Small values of $k\sigma$ correspond to almost isotropic scattering, otherwise scattering in forward direction is enhanced and scattering is less effective. Therefore ℓ_B is larger than ℓ_s, which is shown in the right graph.

region of finite length L. We can extract the intensity distribution in x-direction from the stationary scattering state. Note that in y-direction we have translational invariance due to the periodic boundary conditions after applying the disorder average. Such an intensity distribution is shown in Fig. 4.12. According to Refs. [87, 93] the intensity decays in the diffusive regime for long samples linearly with the position x. Only at the entrance the intensity has a different shape and also at the exit, where boundary effects are present. A method to extract the transport mean free path is to extend the linear decay over the disorder region at the right boundary until it hits the zero-line of the intensity. The distance from this point to the disorder boundary corresponds to the transport mean free path $z_0\ell_{tr}$ for two dimensions, as indicated by an arrow in Fig. 4.12. The factor z_0 is known only numerically: $z_0 \approx 0.82$ [94]. We have confirmed this factor by solving the diffusion process numerically. The procedure we adopted for the numerical diffusion simulation is performed with a Monte-Carlo method: We start with the intensity of an incoming plane wave and propagate one step ℓ, a random length, into the disorder region, where ℓ is taken from the probability distribution with characteristic length ℓ_s: $P(\ell) = \frac{1}{\ell_s} \mathrm{e}^{-\ell/\ell_s}$ according to the average real space Green function. Then a scattering event into a random direction θ takes place, where θ is the scattering angle. The probability distribution for the scattering angle is the normalized phase function $f(k, \theta)$ (Eq. 4.52) corresponding to the correlation function of the disorder potential. Then the propagation of the wave function and the scattering events are repeated until the boundary of the medium is reached. For the intensity distribution we calculate the sum over the intensity along the scattering path. Finally, the entire scattering process is repeated until the intensity distribution is statistically converged.

The only input parameters of the calculation are the incoming intensity, the scatter-

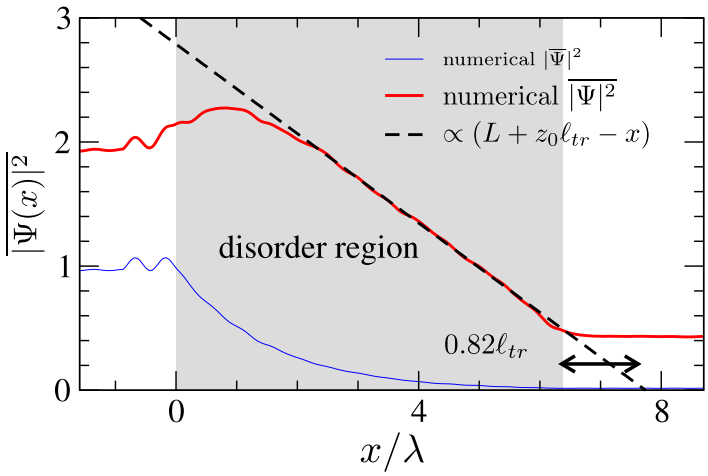

Figure 4.12: The intensity averaged over ~ 700 disorder configurations along the propagation direction x is shown. After an initial bump it decays linearly until the end of the disorder region. The dashed line shows the linear fit where the transport mean free path is extracted. The distance between the disorder boundary and the linear extrapolation of the intensity to the x-axis results in $0.82\ell_{tr}$. For illustration the coherent mode is also shown. Parameters: $kL = 40$, $k\sigma = 0.5$, $V_0 = 0.614\mu$, $k = \sqrt{2m\mu}/\hbar$.

ing mean free path, where we used the numerically extracted one from the quantum mechanical calculation, and the phase function, where we inserted the analytical formula Eq. 4.52. Note that there is no further fitting parameter involved. The result of the diffusion process is shown in Fig. 4.13 (blue line), which shows good agreement with our quantum mechanical results (black line). However, there are deviations, especially in the maximal value of the intensity. This is due to the weak localization effects. To demonstrate this we performed the numerical simulation of the nonlinear Gross-Pitaevskii equation with a nonlinearity strength at which the coherent backscattering cone vanishes (see next chapter for details). In this case the intensity profiles (red and blue lines) lie on top of each other.

4.3.3 Weak localization corrections

We have already seen that in the quantum limit and in the limit of strong scattering we see deviations from the independent scattering approximation due to coherent multiple scattering. Regarding the wave function we can calculate the amplitude of a wave which returns to a given point by summing up all amplitudes ϕ_i corresponding to a scattering path i. Therefore the intensity is given by $\overline{|\sum_i \phi_i|^2} = \sum_i \overline{\phi_i \phi_i^*} + \sum_{i \neq j} \overline{\phi_i \phi_j^*}$. The first part corresponds to the independent scattering approximation. If we take a closer look at the second term, not all contributions cancel. Considering a scattering path

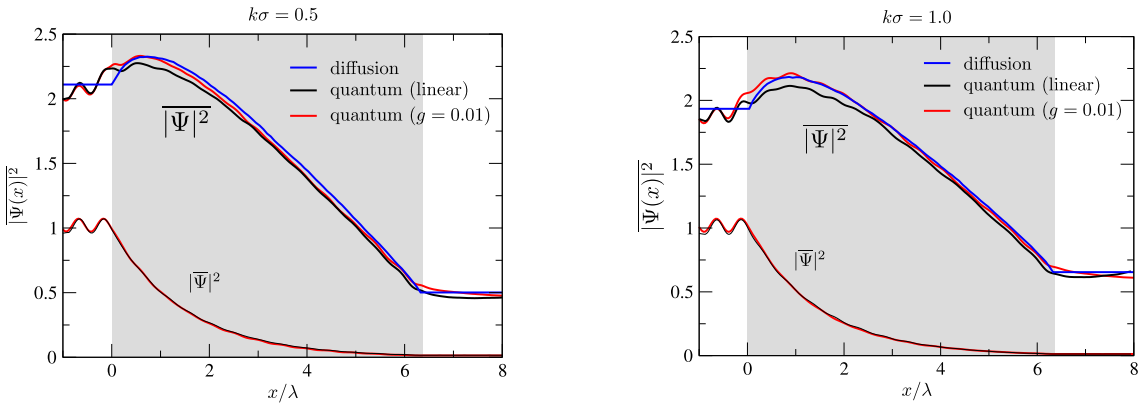

Figure 4.13: Intensity distribution inside the disordered medium. The blue line is the solution of the classical diffusion process in comparison to the black line from our quantum mechanical calculation. The red line is the solution to the Gross-Pitaevskii equation with a nonlinearity of $g = 0.01$, which corresponds to a vanishing backscattering cone (see next chapter). In the latter case the multiple scattering effects are effectively suppressed and therefore the intensity matches best with the classical diffusion process. Parameters left: $k\sigma = 0.5$, $V_0 = 0.614\mu$, $k\ell_s = 9.6$, right: $k\sigma = 1.0$, $V_0 = 0.4\mu$, $k\ell_s = 9.34$.

i and its time reversed counterpart i_{rev}. We write the second term as $\sum_{i\neq j} \overline{\phi_i \phi_j^*} = \sum_i \overline{\phi_i \phi_{i_{rev}}^*} + \sum_{i\neq j\neq i_{rev}} \overline{\phi_i \phi_j^*}$, and realize that the amplitude of a path and its time reversed counterpart have always the same phase. Thus this contribution does not vanish, but increases the return probability by a factor of two.

In order to account for this phenomena in the language of the diagrammatic approach, we have to include the maximally crossed diagrams C_A, also called Cooperon:

$$U \approx U_{\text{Boltzmann}} + C_A \quad \text{with } C_A = \quad + \quad + \ \ldots \quad =: \quad . \tag{4.57}$$

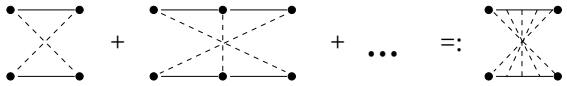

The relation to the ladder diagram is quite close, only the direction of the lower line has to be inverted. Using time-reversal symmetry arguments the crossed diagrams can be related to the ladder diagrams by:

$$C_A(\mathbf{k}, \mathbf{k}', q, E, \epsilon) = L(\tfrac{\mathbf{k}-\mathbf{k}'}{2} + \tfrac{q}{2}, \tfrac{\mathbf{k}'-\mathbf{k}}{2} + \tfrac{q}{2}, \mathbf{k} + \mathbf{k}', E, \epsilon). \tag{4.58}$$

In the case of anisotropic scattering due to the correlated potential it is also necessary to include Hikami corrections C_B, C_C to have a consistent approximation [84]:

$$C = C_A + C_B + C_C = \quad + \quad + \quad =: \quad . \tag{4.59}$$

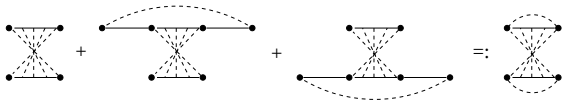

It can be shown that the total Cooperon correction yields $C = \frac{1}{2}(1 - \langle\cos(\theta)\rangle_f) C_A$, [84]. With this information it is possible to evaluate the transport time τ_{tr} with weak

localization correction in analogy to the derivation of the Diffuson. For the corrected transport time we get:

$$\frac{\tau_{tr}}{\tau_B} = \frac{1}{1+\delta\tau_{tr}/\tau_B} \approx 1 - \frac{\delta\tau_{tr}}{\tau_B}, \tag{4.60}$$

where the correction $\delta\tau_{tr}$ is determined by [84]:

$$\frac{\delta\tau_{tr}}{\tau_B} = \frac{2\hbar^2}{m}\int d\mathbf{Q}\,\frac{1}{-i\epsilon+\hbar D_B Q^2} \tag{4.61}$$

$$= \frac{2}{\pi k\ell_B}\int_{1/L}^{1/\ell_B} dQ\,\frac{1}{Q}. \tag{4.62}$$

In the second line the static limit is taken: $\epsilon \to 0$, and $D_B = \frac{\hbar k}{2m}\ell_B$. The integral Eq. 4.61 is divergent, so that an ultra-violet cut-off and also a infra-red cut-off has to be introduced. For the UV cut-off the natural length scale is the system size or in case of phase breaking mechanisms the phase coherence length (whatever is smaller). The infra-red cut-off is set to be the Boltzmann transport mean free path. Evaluation of Eq. 4.62 yields the final expression for the transport mean free path $\ell_{tr} = \frac{\hbar k}{m}\tau_{tr}$ with the corrections for coherent multiple scattering [81, 95]:

$$\ell_{tr} = \ell_B\left[1+\frac{2}{\pi k\ell_B}\ln\left(\frac{L}{\ell_B}\right)\right]^{-1} \tag{4.63}$$

This expression implies that due to the higher return probability the scattering in backward direction is enhanced, and therefore transport processes are suppressed. Thus

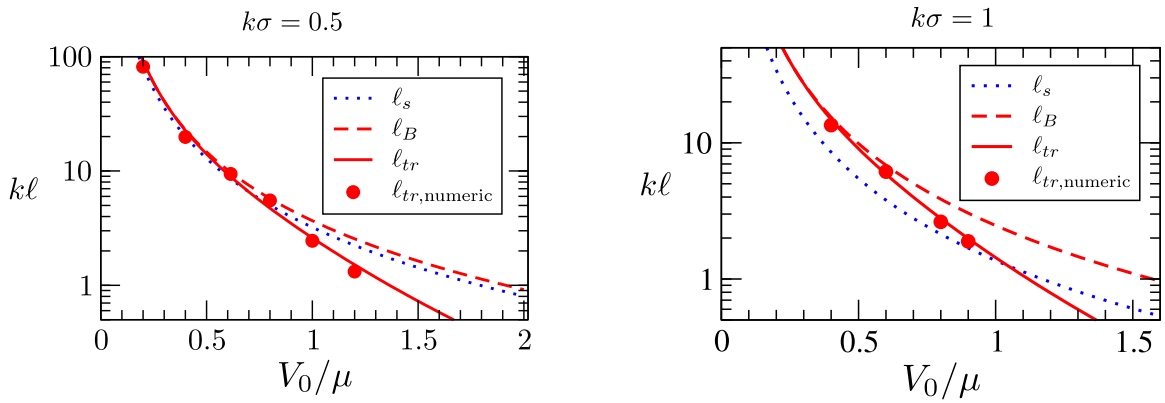

Figure 4.14: Transport mean free path for a Gauss correlated disorder potential for nearly isotropic scattering (left graph) and anisotropic scattering (right graph). The points denote ℓ_B extracted from our numerical simulation, compared to the analytical Boltzmann approximation ℓ_B (dashed) and with weak localization corrections ℓ_{tr}. The blue dotted line shows the scattering mean free path. The length L of the disorder region is $kL = 40$.

the transport mean free path is always smaller than the classical Boltzmann transport mean free path.

Finally we can compare the expected corrections due to weak localization with our numerical simulation. In the case of the Gauss correlated disorder potential the transport mean free path is shown in Fig. 4.14 for almost isotropic scattering (left graph, $k\sigma = 0.5$) and anisotropic scattering (right graph, $k\sigma = 1.0$). In both cases we see the agreement of the analytical results with our numerical simulation. For small disorder strengths V_0 the diffusion approximation is valid and the Boltzmann mean free path captures the physics, whereas for stronger disorder strength V_0 weak localization effects get important, and the transport mean free path (numerical and analytical one) deviate significantly from the independent scattering approximation. The results fit for both isotropic and anisotropic scattering.

Figure 4.15 shows the same situation but now for the speckle disorder potential. As mentioned earlier we already see significant deviations for the scattering mean free path. In the same way the transport mean free path deviates from the analytical predictions. In our numerical data one can see clearly the same qualitative behavior. In the diffusive regime the transport mean free path is larger than the scattering mean free path, which reverts in the regime of weak localization. This deviation of the analytical result is important for the diagrammatic discussion, with regard to the predictive power for experiments, since the threshold for strong localization depends strongly on the transport mean free path. The localization length is given by $\xi_{loc} = \ell_B \exp(\frac{\pi}{2} k\ell_B)$.

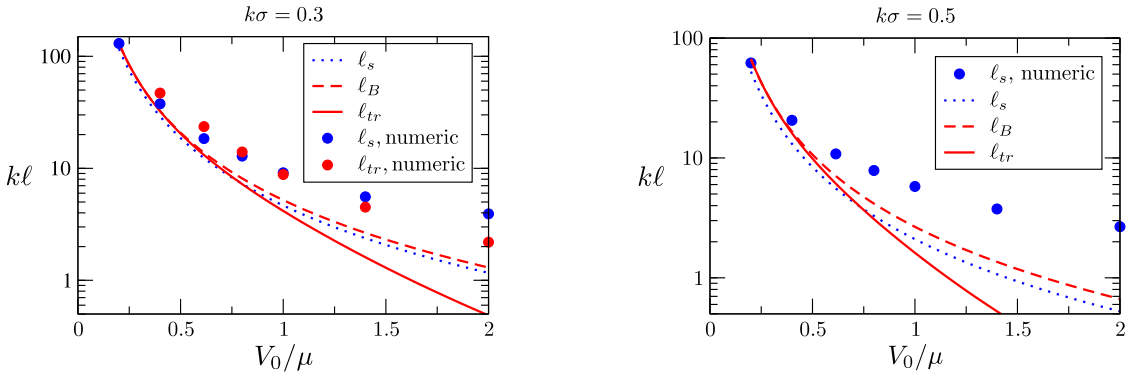

Figure 4.15: Transport mean free path for a speckle disorder potential for nearly isotropic scattering (left graph) and more anisotropic scattering (right graph). The points denote ℓ_B extracted from our numerical simulation, compared to the analytical Boltzmann approximation ℓ_B (dashed) and with weak localization corrections ℓ_{tr}. The blue line shows the scattering mean free path and the blue dots the numerical scattering mean free path. The length L of the disorder region is $kL = 40$.

CHAPTER 5

Coherent backscattering

In astrophysics it was observed already in 1887 [47] that the reflected light intensity at the rings of Saturn is higher in backscattering direction, when sun, Saturn and earth are aligned. The interpretation in terms of coherent backscattering led to a better understanding of this effect [48, 49, 87].
One of the most prominent implications of coherent multiple scattering in disordered systems is the phenomenon of coherent backscattering. If a random media is illuminated by a phase coherent laser beam, an increase of the angular resolved scattered intensity is observed by a factor of two in exactly backward direction [43–45, 87]. This was for the first time realized experimentally and discussed in 1985 by M. van Albada and A. Lagendijk [44], and also by P. Wolf and G. Maret [45]. The effect of coherent backscattering is closely related to the weak localization corrections to the transport mean free path discussed in the previous chapter. The underlying situation appears in several physical systems. This effect can also be investigated in acoustics [50, 51]. The weak localization phenomenon is also valid for electrons, but there the angular structure cannot be analyzed because the electrons are injected and also collected from reservoirs. In this context, however, characteristic peaks in the magneto-resistance are observed [96, 97]. In optical systems the disordered media is often provided by a suspension of small beads with a diameter in the order of $0.5\mu m$ [44, 45]. The parameters of the disordered medium can be modified to reach the regime of Anderson localization [24, 39–42, 46]. Another recently studied scattering medium are cold atoms [52–55], where the atoms act like point-shaped scatterers. Furthermore they were thought as good candidates to explore multiple scattering effects also in the strong localized regime, since resonant scattering of identical particles can be exploited to increase the scattering cross section. But then a modified peak structure, especially for different

polarizations, was observed due to the interaction with the internal structure of the Rubidium atoms. The saturation of the intra-atomic transition leads to nonlinear, but also to inelastic scattering [56–58]. Further complexity is added due to thermal motion [52] and polarization phenomena [55].

Now we introduce the opposite system: We change the propagating waves from light to a Bose-Einstein condensate, and change the disorder potential from the condensate as scatterers to a speckle potential created by light. The (interacting) Bose-Einstein condensate is scattered in a quasi two-dimensional disorder potential, resulting from a speckle field created with a laser. This opens new possibilities to study coherent backscattering in two dimensions with a special focus on the atom-atom interaction described within the Gross-Pitaevskii equation. Our approach should provide a cleaner system compared to scattering with light from cold atoms since the wave function of the Bose-Einstein condensate in the mean-field regime remains well preserved in the presence of the nonlinearity. We show that a moderate nonlinearity strength already results in substantial modifications of the albedo, leading to a negative coherent backscattering contribution indicating destructive instead of constructive interference. We further confirm our numerical results by comparing them with a diagrammatic approach which was developed very recently by T. Wellens and B. Grémaud [59]. Increasing the nonlinearity further, we show that the stationary solution is not stable anymore and we enter into a time-dependent regime.

5.1 Linear coherent backscattering

We begin by introducing a theoretical scheme of coherent backscattering and of calculating the resulting intensity in backward direction for a non-interacting system. Coherent backscattering arises due to constructive interference between time reversed paths. To demonstrate this we consider an incoming wave which scatters along the path i and leaves the medium in backward direction with angle θ between the incoming and the outgoing wave vector. The wave is described by the wave function ϕ_i corresponding to the scattering path i.
We first describe the two parts the intensity consists of: A diffusive part, independent of the angle θ between the incoming and outgoing wave vector, and where the wave function and its complex conjugated one have the same scattering events in the same direction, and a coherent part, where the wave function and its complex conjugate have the same scattering events in time reversed direction, and which depends on θ. Later we calculate these two expressions for the diffusive and coherent intensity.
The intensity is given by $\overline{|\sum_i \phi_i|^2} = \sum_i \overline{\phi_i \phi_i^*} + \sum_{i \neq j} \overline{\phi_i \phi_j^*}$. The first part relates to the diffusive intensity which is independent of the angle θ. If we take a closer look at the second term, we see that not all contributions cancel in the disorder average. To

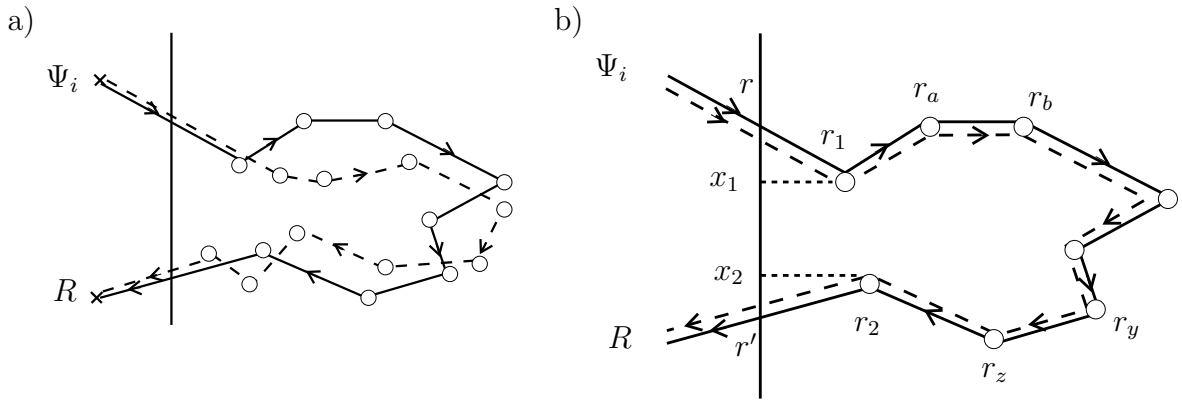

Figure 5.1: a) Scattering path, which results in a speckle pattern in the backscattered intensity profile in one disorder realization, but vanishes upon disorder averaging, since the phase difference between the two scattering paths depends strongly on the disorder realization. b) Diffuson approximation for the backscattered intensity. The contribution of this scattering paths survives the disorder average, because the two paths accumulate always the same phase.

every scattering path i there exists also a time reversed scattering path $i_{\rm rev}$. Now we write the second term as $\sum_{i\neq j}\overline{\phi_i\phi_j^*} = \sum_i \overline{\phi_i\phi_{i_{\rm rev}}^*} + \sum_{i\neq j\neq i_{\rm rev}}\overline{\phi_i\phi_j^*}$, and realize that the amplitude of a path and its time reversed counter part have always the same phase if the angle $\theta = 0$. Thus, this contribution, $\sum_i \overline{\phi_i\phi_{i_{\rm rev}}^*}$, does not vanish but increases the backscattering by a factor of two. The last term, $\sum_{i\neq j\neq i_{\rm rev}}\overline{\phi_i\phi_j^*}$, finally vanishes in the disorder average. Indeed, for a fixed realization of the disorder it gives rise to a random speckle pattern of the reflected intensity, see Fig. 5.1a.

In order to study the angular dependence of the backscattering cone we follow the derivation presented by E. Akkermans et al. [87, 98, 99]. We consider the case of isotropic scattering, that means the scattering mean free path is the same as the transport mean free path: $\ell_s = \ell_{tr}$. First we study the backscattered intensity arising from the independent scattering approximation, which corresponds to the Diffuson approximation, where the two propagation lines experience the same scatterers in the same order, see Fig. 5.1b. We specify the case where the incident wave enters perpendicular the disorder medium located in the half plane, $x > 0$. The scattered current j_d in backward direction then is given by:

$$j_d = n2\pi kR \int d\mathbf{r}_1 d\mathbf{r}_2 \;\; \left|\overline{\psi}_i(\mathbf{r}_1)\right|^2 P(\mathbf{r}_1,\mathbf{r}_2) \left|\overline{G}^R(\mathbf{r}_2,\mathbf{R})\right|^2 \; . \tag{5.1}$$

Here $\overline{\psi}_i(\mathbf{r}_1)$ is the incoming plane wave, which scatters the first time at $\mathbf{r}_1$, and $\overline{G}^R$ is the disorder averaged Green function as defined in Eq. 4.23. The propagation of the intensity from $\mathbf{r}_1$ to $\mathbf{r}_2$ is expressed by the probability density kernel $P(\mathbf{r}_1,\mathbf{r}_2)$ taking into account all scattering events. The wave exits from the last scattering event $\mathbf{r}_2$ to $\mathbf{R} = R\hat{\mathbf{s}}_e$, $\hat{\mathbf{s}}_e$ denoting the exit direction. In the formula n is a normalization factor.

The disorder averaged incoming wave which is exponentially damped inside the disorder medium with the scattering mean free path as discussed in Sec. 4.2 is given by:

$$\overline{\psi}_i(\mathbf{r}_1) \propto \mathrm{e}^{-|\mathbf{r}_1-\mathbf{r}|/2\ell_s}\ \mathrm{e}^{ik\hat{\mathbf{s}}_i\mathbf{r}_1}. \tag{5.2}$$

$\mathbf{r}$ denotes the point where the incoming wave enters the medium, and ℓ_s is the scattering mean free path. To propagate the wave from the last scattering position $\mathbf{r}_2$ to the point of observation, $\mathbf{R}$, we use the Green function Eq. 4.23:

$$\begin{aligned}\overline{G}^R(\mathbf{r}_2,\mathbf{R}) &\propto -i\,\mathcal{H}_0(k|\mathbf{R}-\mathbf{r}_2|)\ \mathrm{e}^{|\mathbf{r}'-\mathbf{r}_2|/2\ell_s} &(5.3)\\ &\approx -\mathrm{e}^{|\mathbf{r}'-\mathbf{r}_2|/2\ell_s}\ \frac{\mathrm{e}^{i(kR+\pi/4)}}{\sqrt{2\pi kR}}\ \mathrm{e}^{ik\hat{\mathbf{s}}_e\mathbf{r}_2}. &(5.4)\end{aligned}$$

Here $\mathbf{r}'$ is the exit point of the outgoing wave. In the last approximation we assumed $\mathbf{R}$ to be far to the left. We define x_2 as the distance from the line $x = 0$. Therefore we have $|\mathbf{r}_2 - \mathbf{r}'| = x_2/\mu$ with $\mu = \cos(\theta)$, see Fig. 5.1b. Then,

$$j_d = n\int d\mathbf{r}_1 d\mathbf{r}_2\ \ \mathrm{e}^{-x_1/\ell_s}\mathrm{e}^{-x_2/\mu\ell_s}P(\mathbf{r}_1,\mathbf{r}_2). \tag{5.5}$$

At last we have to solve for the intensity relaxation kernel $P(\mathbf{r}_1, \mathbf{r}_2)$. It has to fulfill the stationary diffusion equation Eq. 4.45 with the appropriate boundary conditions:

$$-D\Delta_{\mathbf{r}_2}P(\mathbf{r}_1,\mathbf{r}_2) = \delta(\mathbf{r}_1-\mathbf{r}_2)\ . \tag{5.6}$$

As seen in Sec. 4.3.2, the diffusive intensity vanishes a distance $z_0\ell_{tr}$ away from the boundary, with z_0 being a fixed number, mentioned already in the last chapter, $z_0 = 0.82$ in two dimensions.

In the next step we calculate the coherent multiple scattering contribution to the backscattered intensity. We consider the crossed diagrams, also called Cooperons. There, the two propagator lines experience the same scattering points, but in reverse direction, as shown in Fig. 5.2. The expression for the coherent backscattered current $j_c(\hat{\mathbf{s}}_e)$ obeys the same structure as for the diffusive one, varying only in the positions for the first scattering event for $\overline{\psi}_i$ and $\overline{\psi}_i^*$ and similarly for the outgoing wave:

$$\begin{aligned}j_c(\hat{\mathbf{s}}_e) &= n\int d\mathbf{r}_1 d\mathbf{r}_2\ \ \overline{\psi}_i(\mathbf{r}_1)\overline{\psi}_i^*(\mathbf{r}_2)\ P'(\mathbf{r}_1,\mathbf{r}_2)\ \overline{G}^R(\mathbf{r}_2,\mathbf{R})\overline{G}^A(\mathbf{R},\mathbf{r}_1) &(5.7)\\ &= n\int d\mathbf{r}_1 d\mathbf{r}_2\ \ \mathrm{e}^{-\frac{\mu+1}{2\mu}\frac{x_1+x_2}{\ell_s}}\ P'(\mathbf{r}_1,\mathbf{r}_2)\ \mathrm{e}^{ik(\hat{\mathbf{s}}_i+\hat{\mathbf{s}}_e)\cdot(\mathbf{r}_1-\mathbf{r}_2)}\ . &(5.8)\end{aligned}$$

Note that the normalization factor n is the same for j_d and j_c. Here $P'(\mathbf{r}_1, \mathbf{r}_2)$ is the intensity relaxation kernel for the crossed diagrams. It can be shown by time reversal

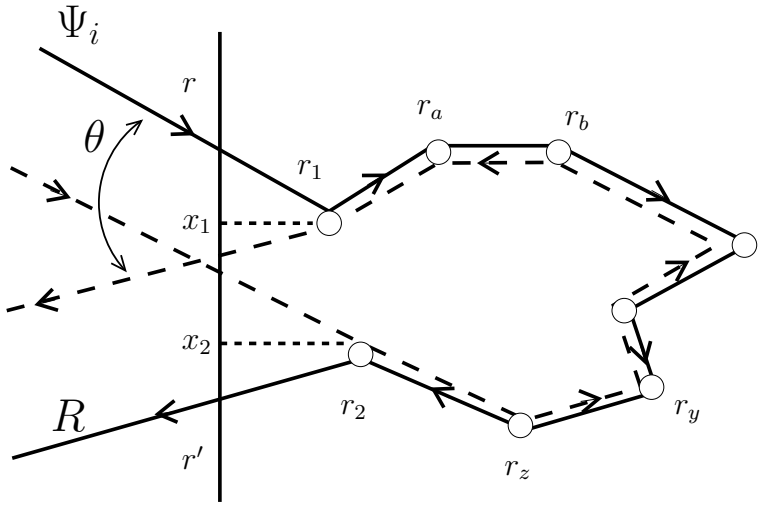

Figure 5.2: Contribution of the Cooperon to the backscattered intensity. For the angle $\theta = 0$ the two paths acquire the same phase and interfere constructively, resulting in the same intensity contribution in backward direction as the Diffuson approximation, see Fig. 5.1. The intensity reduces for a larger angle and a larger distance between the first and last scattering event.

arguments (similar to Eq. 4.58) that $P'(\mathbf{r}_1, \mathbf{r}_2) = P(\mathbf{r}_1, \mathbf{r}_2)$. We see that in backward direction both contributions, the diffusive one and the coherent one, are equal:

$$j_c(\theta = 0) = j_d(\theta = 0) \tag{5.9}$$

Furthermore we notice the additional phase factor in Eq. 5.8, compared to j_d. This phase factor results in a strong dependence of j_c on the angle θ between incoming and reflected wave in contrast to the almost flat profile of the diffusive contribution.

Finally, it is possible to calculate $P(\mathbf{r}_1, \mathbf{r}_2)$ in the semi-infinite medium and to obtain the shape of the cone [87, 98–101]:

$$\begin{aligned}
\frac{j(\theta)}{j_d(\theta=0)} &= \mu \frac{2z_0 + \frac{2\mu}{\mu+1}}{2z_0+1} + \frac{1}{(2z_0+1)(k_\perp \ell_s + \frac{2\mu}{\mu+1})^2} \left(\frac{1-\exp(-2z_0 k_\perp \ell_s)}{k_\perp \ell_s} + \frac{2\mu}{\mu+1} \right) \\
&\approx 1 + \frac{1}{(2z_0+1)(k_\perp \ell_s + 1)^2} \left(\frac{1-\exp(-2z_0 k_\perp \ell_s)}{k_\perp \ell_s} + 1 \right) \qquad (5.10) \\
&\approx 2 - \frac{2(z_0+1)^2}{1+2z_0}\ k\ \ell_s\, |\theta| \ . \qquad (5.11)
\end{aligned}$$

Here $k_\perp = k(\hat{\mathbf{s}}_i + \hat{\mathbf{s}}_e)_\perp = k \sin(\theta)$ is the projection on the $x = 0$ line. In the second line of Eq. 5.10 we assumed $\mu = \cos(\theta) \approx 1$, which is usually a valid approximation, since the width of the cone is very sharp in optical experiments. We furthermore recognize

that the width of the cone depends on the product of the scattering mean free path and the wave vector and is given by $\delta\theta = \frac{1}{k\ell_s}$.

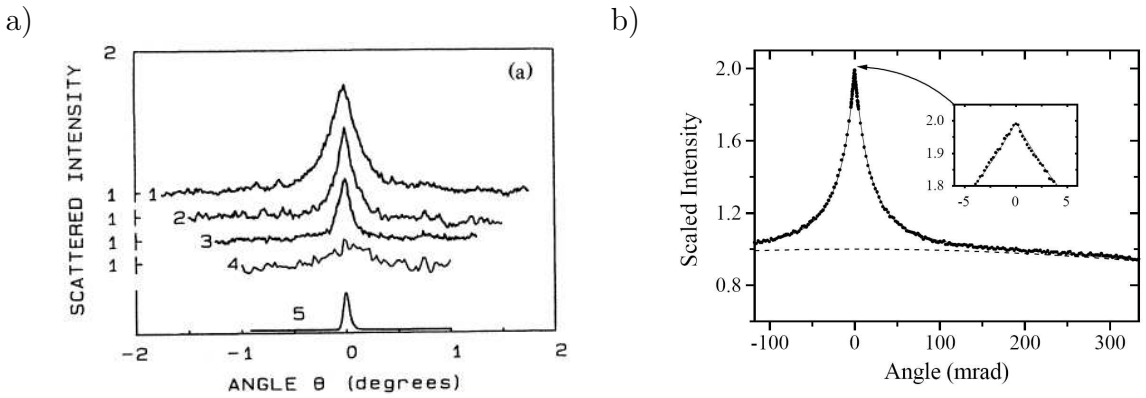

Figure 5.3: a) Experimental observation of the coherent backscattering from a suspension of sub-micron sized polystyrene particles by P. Wolf and G. Maret [45] in 1985. The cone width (curve 1) decreases with an decreasing concentration of the particles, and vanishes (curve 4) if the optical resolution (curve 5) is larger than the cone width. b) The cone shape was studied with high precision by D. S. Wiersma [102] and shows the triangular cusp of the backscattered intensity measured in a powder of ZnO. The pictures are from [45] and [102].

Coherent backscattering was first observed experimentally by M. P. van Albada and A. Lagendijk [44] and P. Wolf and G. Maret [45] in 1985, see Fig. 5.3 a. In these experiments a highly concentrated suspension of sub-micron sized polystyrene spheres was illuminated with a laser beam. In backward direction it was possible to observe the backscattering cone. Here we see already the sharp cusp of the backscattering signal, also present in the analytical description. The approximation $k_\perp \approx \frac{2\pi}{\lambda}|\theta|$ for the third equation in Eq. 5.11 is only valid for very small angles and shows the triangular shape of the cone. This reveals that the line shape of the cone has a singularity in the backscattering direction. When analyzing the contributions to the coherent backscattering arising from different scattering orders [100], it is observed that low orders contribute to the broader angular spectrum, while the higher scattering orders form the sharp cusp of the coherent backscattering cone. This was nicely demonstrated experimentally by D. S. Wiersma [102], see Fig. 5.3 b.

The derivation of the cone shape for weak localization presented here is valid only for isotropic scattering where $\ell_s = \ell_{tr}$ is the only relevant length scale. In the case of anisotropic scattering it can be shown that the shape of the cone is not changed, only ℓ_s has to be replaced by the transport mean free path: $\ell_s \to \ell_{tr}$ [87, 100].

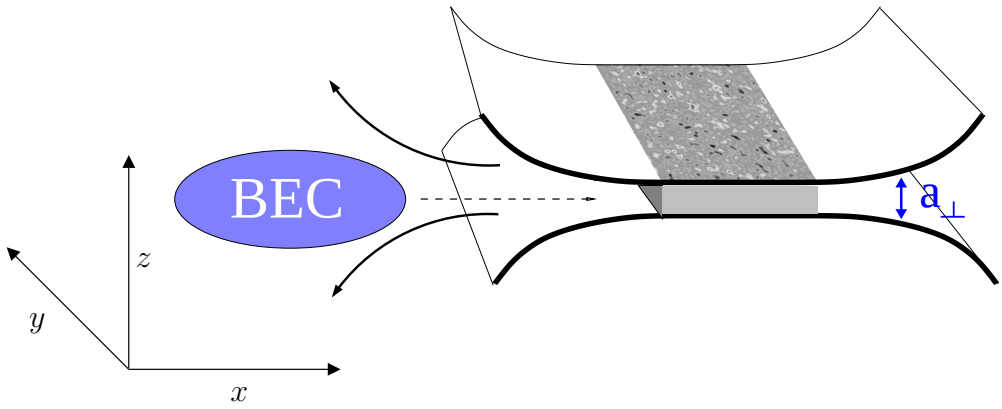

Figure 5.4: Sketch of an experimental setup for the study of coherent backscattering with Bose-Einstein condensates. The reflected matter waves can be detected after a time-of-flight expansion with absorption imaging.

5.2 Coherent backscattering with Bose-Einstein condensates

In this section we introduce the phenomenon of coherent backscattering to the field of matter waves, especially with Bose-Einstein condensates. To our knowledge this has not been studied experimentally and also not theoretically before our work. We show a new effect arising due to the atom-atom interaction in the condensate. To this end we consider the setup shown in Fig. 4.1, where a broad wave packet of the Bose-Einstein condensate enters adiabatically into a two-dimensional waveguide. Then the condensate scatters in the disorder region and is partly transmitted and partly reflected. The reflected intensity again leaves the waveguide (for a sketch see Fig. 5.4). The condensate then can be detected after a time-of-flight expansion and absorption imaging, where the Bose-Einstein condensate is resonantly illuminated and then the transmitted intensity is recorded. Of course the Bose-Einstein condensate is destroyed at this measurement process.

Alternatively, it might be possible to extend the method of an atom laser to two-dimensional systems. In one dimension a guided quasi-continuous atom laser has already been demonstrated [15–17], where a Bose-Einstein condensate is trapped in an optomagnetic trap. Then it is coupled out by superimposing a radio frequency and inserted into the quasi one-dimensional optical waveguide, formed by a narrow focused laser beam.

The two-dimensional waveguide can be realized with two laser beams propagating in opposite direction along the z-direction. This forms a standing wave, and therefore an

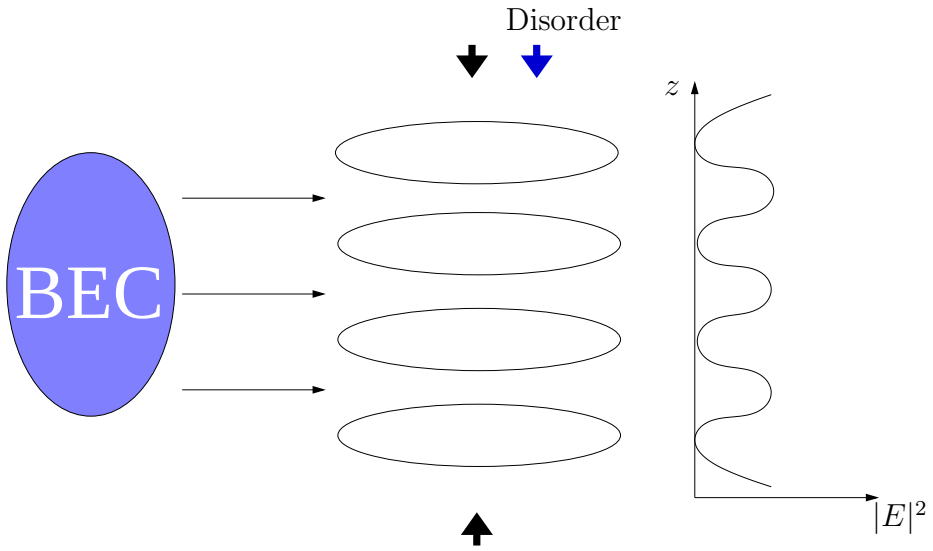

Figure 5.5: The two-dimensional confinement can be realized with an optical lattice potential in z-direction. Several propagation processes in the different slices can be performed, allowing already for an disorder average.

optical lattice potential in z-direction. One of these potential minima can then be used to confine the Bose-Einstein condensate to two dimensions, such that in transverse z-direction only the ground state is populated. Along the z-direction one can superimpose the disorder potential by optical means. But it has to be taken into account, that we have to perform an average over disorder realizations in order to have a statistical statement in contrast to single samples. To this end one can use several minima of the confining optical lattice potential in z-direction and perform the propagation of the Bose-Einstein condensate in the two-dimensional slices simultaneously. This procedure intrinsically implies already an average over disorder realizations. This is depicted in Fig. 5.5. Another experimental setup was suggested by G. Labeyrie and is shown in Fig. 5.6, where a strongly confined droplet of condensate starts to expand and reaches a ring of disordered media. In this configuration the coherent backscattering shows up as an increased intensity at the original starting point of the expanding condensate. The situation is similar to the situation of coherent backscattering of acoustic seismological waves in the near field around a source [103].

5.3 Nonlinear coherent backscattering

In Sec. 5.1 we studied the coherent backscattering effect for wave functions which are solutions to the linear Schrödinger equation or equivalently to the Helmholtz equation

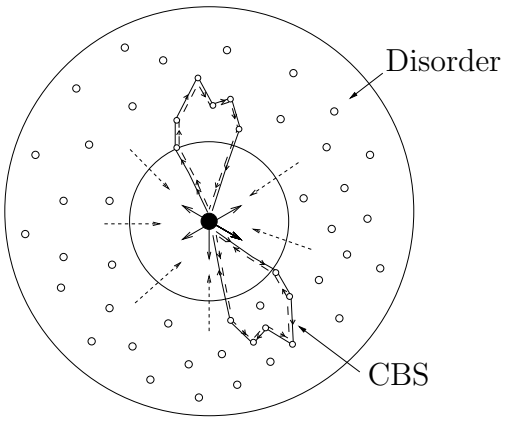

Figure 5.6: Experimental setup suggested by G. Labeyrie, where an condensate which is initially confined to the center expands into the disorder region and then gets (coherently) scattered back to the origin, similar to the coherent backscattering of acoustic seismological waves in the near field around a source [103].

in the optical context. Now we apply this mechanism to the nonlinear Gross-Pitaevskii equation, where the nonlinearity arises due to the atom-atom interaction in the s-wave approximation. The Gross-Pitaevskii equation with source term is given by (Eq. 3.2):

$$\begin{aligned} i\hbar\frac{\partial}{\partial t}\Psi(\mathbf{r},t) &= \left(-\frac{\hbar^2}{2m}\Delta + V(\mathbf{r}) + \frac{\hbar^2 g(x)}{2m}|\Psi(\mathbf{r},t)|^2\right)\Psi(\mathbf{r},t) \\ &\quad + S_0(t)\phi_S(y)\delta(x-x_0)\,\mathrm{e}^{-i\mu t/\hbar}. \end{aligned} \tag{5.12}$$

The dimensionless nonlinearity strength $g(\mathbf{r}) = 4\sqrt{2\pi}a_s/a_\perp(\mathbf{r})$ is determined by the s-wave scattering length a_s and the transverse confinement $a_\perp(\mathbf{r}) = \sqrt{\hbar/[m\omega_\perp(\mathbf{r})]}$. The source term is already included, and we use a constant profile $\phi_S(y) \equiv 1$ (if not explicitly specified otherwise), which corresponds to an incoming plane wave perpendicular to the disorder region as shown in Fig. 5.7. In the following calculations we fix the incoming current density to $j_{in} = \hbar k|\Psi_0|^2/m$, where $k = \sqrt{2m\mu}/\hbar$ is the wavenumber of the incident beam. This is no restriction since the Gross-Pitaevskii equation can be rescaled by keeping the product $g|\Psi|^2$ constant, and a higher current just renormalizes the nonlinearity strength g to lower values otherwise.

In order to study coherent backscattering numerically, we have to extract the angular resolved current from the simulations. One possibility is to take the disorder average over the wave function and to apply a two-dimensional Fourier transformation in the region between the source and the disorder where the nonlinearity is still negligible small. The nonlinearity has to be negligible, such that the superposition principle is valid, and in order to associate the Fourier modes with the outgoing current in certain

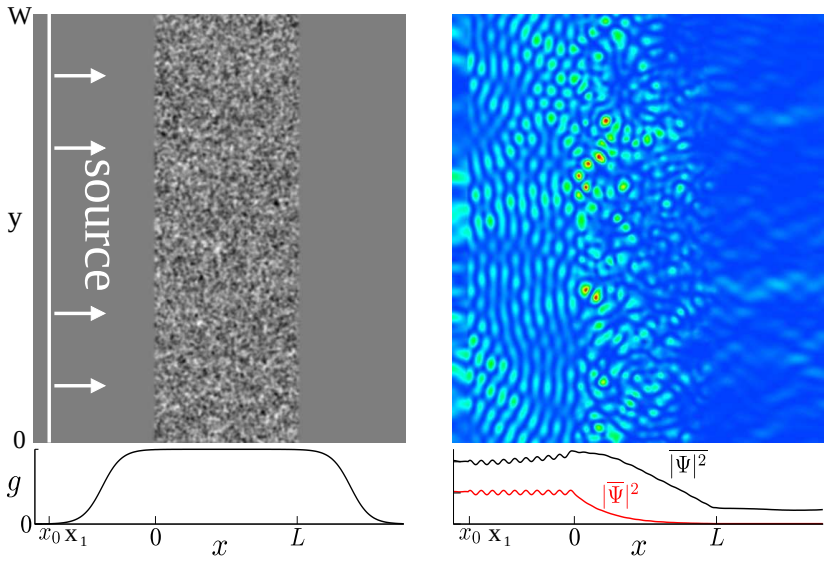

Figure 5.7: Scattering geometry and stationary scattering state associated with a randomly generated disorder potential. The left hand side displays the potential $V(x, y)$ in a gray scale plot and the spatial variation of the nonlinearity $g(x)$. x_0 is the position of the source and x_1 denotes the position where the backscattered current is evaluated. The upper right panel shows the density plot of the corresponding scattering state. The lower right panel shows the decay of the coherent mode $|\overline{\Psi}|^2$ and the density $\overline{|\Psi|^2}$ averaged over y and ≈ 1000 disorder configurations.

directions. Thereby the relevant **k**-vectors of the transport modes are extracted. A density plot pointing out the intensity distribution as a function k_x and k_y is shown in Fig. 5.8 b. With this method we can separate incoming waves ($k_x > 0$) from reflected waves ($k_x < 0$). The strong peak in forward direction corresponds to the incoming plane wave, while in backward direction we can clearly see the coherent backscattering signal at $k_y = 0$ and $k_x < 0$ and for larger angles we see also the diffusive background. The drawback of this method is that we need an extra simulation region where the nonlinearity is zero and which is large enough to allow a good resolution. Already in Fig. 5.8(b) the size in x-direction is almost to small resulting in artificial oscillations for large angles due to the finite spacing.

On the other hand the Fourier decomposition in x-direction is only necessary to subtract the incoming wave component. However, we know the value of this amplitude analytically and can also calculate it numerically in a simulation without any disorder potential. We have chosen the second method, because the discretization of the source can introduce errors in the order of 0.2% for typical input parameters, and those deviations from the analytical prediction are eliminated with the numerical calculation of the propagating plane wave $\Phi_0(x, y, t)$. To avoid these numerical errors we subtract

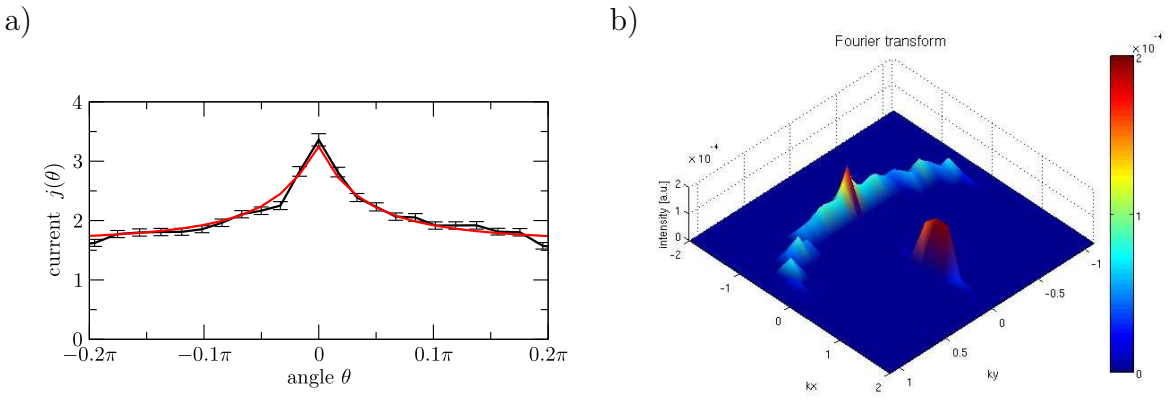

Figure 5.8: a) The angular dependent current of the backscattered condensate is plotted. The clear coherent backscattering cone is observed. The analytical formula Eq. 5.10 is fitted and shows good agreement. The current is extracted along the line $x = x_1$. b) Extraction of the coherent backscattering by a two-dimensional Fourier transformation of this part of the averaged wave function right to the source position. The strong peak (height is cut) represents the incoming wave ($k_x > 0$). For $k_x < 0$ we see the coherent backscattering cone. The oscillations arise due to the finite spacing of the grid.

the wave function that is numerically obtained in the absence of a scattering potential, namely $\Phi_0(x, y, t) \propto |\Psi_0| \mathrm{e}^{ikx}$, from the wave function $\Phi(x, y, t)$ to get the reflected part $\Phi_{\mathrm{ref}}(x, y, t)$:

$$\Phi_{\mathrm{ref}}(x, y, t) = \Phi(x, y, t) - \Phi_0(x, y, t) \; . \tag{5.13}$$

Note that we do not have to care about a time-dependent phase-factor since the trivial time-dependence has been already separated with the ansatz $\Psi(\mathbf{r}, t) = \Phi(\mathbf{r}, t)\mathrm{e}^{-i\mu t/\hbar}$ in the numerical calculation. In order to calculate the backscattered current we apply a Fourier transformation in y-direction to the disorder averaged reflected wave function $\overline{\Phi}_{\mathrm{ref}}(x_1, y)$ at the position x_1 close to the source, where the nonlinearity $g(x_1)$ is still negligible small (see Fig. 5.7). This results in a decomposition into transverse eigenmodes $\Phi(x_1, k_{y,n}) \sim \exp(in\pi y/W)$, which supports outgoing waves into directions with angles $\theta_n = \arcsin[\frac{2\pi n}{kW}]$.

The current density in direction θ_n, normalized with respect to the total incoming current $W j_{in}$, is then calculated by:

$$j(\theta_n) \;\; = \;\; \frac{2\pi}{W j_{in}} \, \frac{\hbar}{m} \, k_{x,n} \, |\Phi(x_1, k_{y,n})|^2 \; W \cos(\theta_n) \; . \tag{5.14}$$

The wave vector $k_{x,n}$ is related to the transverse mode by $k_{x,n} = \sqrt{|\mathbf{k}|^2 - k_{y,n}^2}$ (see Fig. 5.9). The last factor $W \cos(\theta_n)$ arises due to the geometrical fact that the outgoing

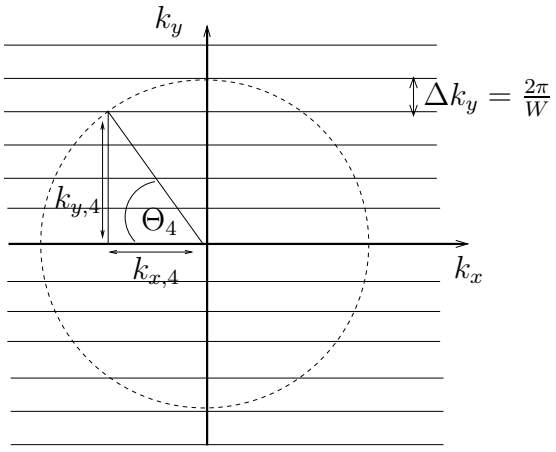

Figure 5.9: The angular resolution of the backscattered current is limited by the width W of the disorder region. This implies a spacing of the wave vector $\Delta k_y = \frac{2\pi}{W}$ in y-direction. The angle corresponding to the transversal Fourier mode n is given by: $\theta_n = \arcsin[\frac{2\pi n}{kW}]$.

current in direction θ_n passes through a perpendicular line of length $W\cos(\theta_n)$. A typical angular resolved backscattered current is shown in Fig. 5.8 a. The current is then normalized in the following way:

$$\int_0^{2\pi} j(\theta)\, d\theta = 2\pi\ . \tag{5.15}$$

Note that this integration (or summation over discrete angles) also takes angles in forward direction into account.

In the following we want to summarize the numerical implementation and the parameters we have chosen. Afterwards we present the results we yield in this way: We consider a Gauss correlated disorder potential characterized by $\overline{V(\mathbf{r})V(\mathbf{r'})} = V_0^2 \exp(-\frac{|\mathbf{r}-\mathbf{r'}|^2}{2\sigma^2})$. Furthermore we specify an average height of the potential of $V_0 = 0.614\mu$ and a correlation length of $k\sigma = 0.5$ with the wave vector $k = \sqrt{2m\mu}/\hbar$. This corresponds to almost isotropic scattering as already seen in the previous chapter. Using the results of Eq. 4.27, Eq. 4.53 and Eq. 4.63 we can calculate the scattering and transport mean free path. Additionally we have extracted the length scales numerically and have found a scattering mean free path $k\ell_s \simeq 9.61$ and a transport mean free path of $k\ell_{tr} \simeq 9.75$, which is in good agreement with the analytical result. The result $\ell_s \approx \ell_{tr}$ confirms that we have almost isotropic scattering. For the optical thickness b of the disorder medium we have chosen $b = L/\ell_s = 4.1$ ($kL = 40$) and the width $kW = 120$. The width of the system results in an angular resolution of $\Delta\theta = 2\pi/kW \simeq 0.05[rad]$. In order to perform the disorder average we repeat the time-dependent integration of the Gross-Pitaevskii equation approximately 10^3 times with randomly generated disorder realizations for each set of parameters. The error bars in the following graphs represent

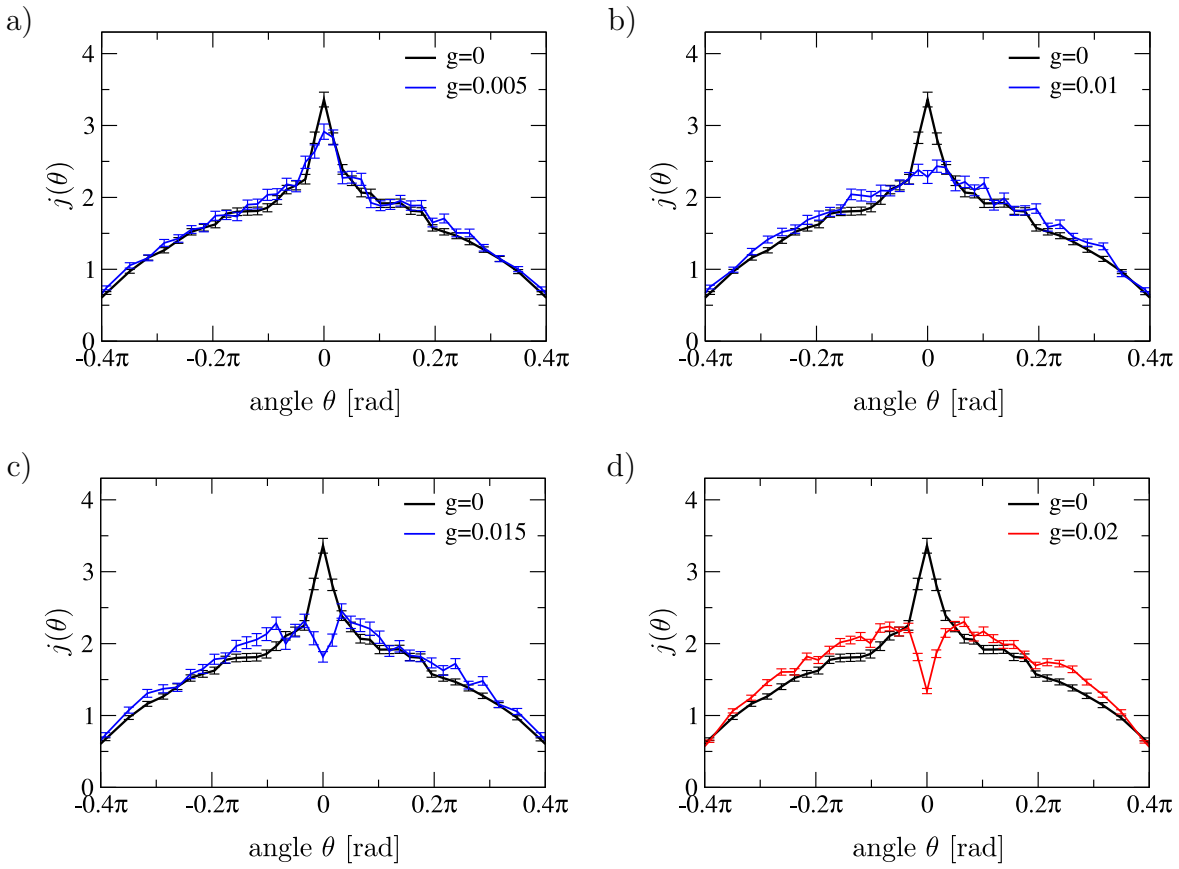

Figure 5.10: The coherent backscattering peak for the nonlinear Gross-Pitaevskii equation is calculated for several nonlinearity values g. The error bars correspond to the statistical deviations arising from the disorder average (∼1000 realizations). a) In the linear regime $g = 0$ the well known behavior is observed with a cone height by a factor of two larger compared with the diffusive background. b) For a nonlinearity $g = 0.01$ the coherent backscattering peak vanishes. c) and d) The cone reverts into a pronounced dip ($g = 0.02$), implying destructive instead of constructive interference. The underlying interference phenomenon is still active. This is observed already at a small interaction energy $g|\Psi(\mathbf{r})|^2 \sim 10^{-2}$.

the standard deviation arising from the disorder average.

In the linear case $g = 0$ we encounter the well known coherent backscattering peak as explained in the previous section. We observe a peak height of roughly a factor two compared to the diffusive background as shown in Fig. 5.10(a). This is expected since our potential has a vanishing mean $\overline{V(\mathbf{r})} = 0$ and furthermore the real part of the refractive index in the effective medium is modified only marginal as we have seen in Fig. 4.7. This implies a small single scattering contribution. For a small nonlinearity the cone height is reduced (Fig. 5.10(a)) and vanishes eventually if the interaction

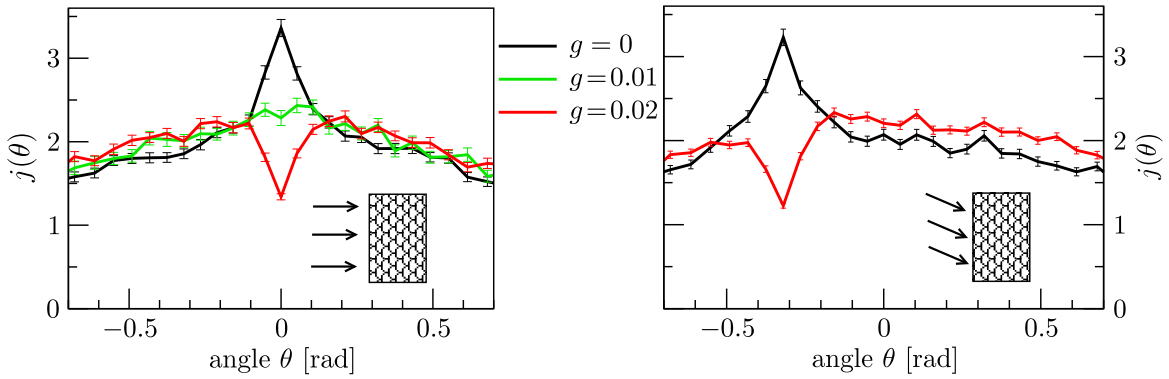

Figure 5.11: We compare the coherent backscattering, where the incident wave enters the disorder region perpendicular (left graph) and where the incoming wave is tilted by an angle $\phi_{-6} \simeq -0.32$ (right graph). In the latter case coherent backscattering is observed in retro-reflection, in contrast to ordinary specular reflection, where the peak would appear at $\phi_{+6} \simeq +0.32$. This is also observed in the nonlinear case, which confirms that in both cases the feature arises due to interference between time reversed paths.

strength increases (Fig. 5.10(b)). But it is very interesting that the underlying interference effect is not washed out but reverts the cone (Fig. 5.10(c) and Fig. 5.10(d)) for intermediate strength of the nonlinearity. We find the novel phenomenon that the atom-atom interaction reverts the interference from constructive to destructive, implying that the interference phenomenon is still effective. The shape of the cone and the dip are quite similar, especially the width is comparable. The intermediate interaction strength $g = 0.02$, where the dip is quite pronounced, is still weak, corresponding to an interaction energy of $g|\Psi(\mathbf{r})|^2 \sim 10^{-2}\mu$.

In the case of a perpendicular incident wave we cannot distinguish between coherent backscattering and ordinary specular reflection. In the case of coherent backscattering one expects the peak to appear in exactly backward direction in contrast to specular reflection, where the reflected wave forms with the incoming wave an angle of $2\phi_n$. In order to prove that the dip is still related to coherent backscattering we investigated the angular resolved current in the case where the incident wave enters the disorder medium with an angle ϕ, as depicted in Fig. 5.11 in the right side. This can actually be achieved in our numerical simulation by changing the transverse function of the source. To this end we choose the source amplitude $\phi_S(y)$ of Eq. 5.12 to be an excited transverse eigenmode:

$$\phi_{S,n}(y) = e^{i\frac{2\pi n}{W}y}. \tag{5.16}$$

The incident wave is tilted by the angle $\phi_n = \arcsin[\frac{2\pi n}{kW}]$ in this case.

We specifically have chosen $n = -6$ and $\phi_{-6} \simeq -0.32$. In the case of coherent

backscattering the peak has to appear in exactly backward direction. Indeed we observe the dip structure like the cone in retro-reflection, see Fig. 5.11. This shows clearly that the origin of the dip arises due to interference between the time reversed scattering paths. In the right graph, especially for $g = 0$, one is attempted to see a small peak at the opposite angle $\phi_{+6} \simeq +0.32$ which could correspond to specular reflection of the single scattering events. But this is not significant due to the statistical error bars.

The observed dip structure shows that the reduction of the peak height results from a *coherent* effect, which is necessary for a negative contribution of the coherently scattered light, in contrast to "dephasing processes", which lead to a suppressed coherent contribution. Such a contribution is never negative. This reduced coherent part is observed in absorption processes and polarization effects [55, 104], thermal motion [52], or magnetic fields in electronic devices [96, 97] (except in combination with spin orbit coupling [105]). Nonlinearities, on the other hand, also arise in scattering of light from cold atoms [53] due to the saturation of the intra-atomic transition [56–58]. However, in this case the saturation leads also to inelastic scattering. To this end our approach, where a Bose-Einstein condensate in the mean-field regime scatters from an optical disorder potential provides a cleaner situation, since the coherence of the atomic wave function is well preserved in the presence of the nonlinearity.

Before we study the new effects in nonlinear coherent backscattering in more details, we first give a short review of a diagrammatic approach to nonlinear coherent backscattering, which was developed very recently. This theory will confirm our numerical results. The discussion of results for even stronger atom-atom interaction is postponed until Sec. 5.6, since we enter a new regime, where time-dependent effects play a role.

5.4 Diagrammatic approach to nonlinear coherent backscattering

In order to confirm our observations of the reversed coherent backscattering peak arising due to the atom-atom interaction in a Bose-Einstein condensate, we compare our numerical results with a diagrammatic theory developed recently by T. Wellens and B. Grémaud [59] for nonlinear scattering events in the optical context. This theory is equally applicable to a nonlinear wave equation like the Gross-Pitaevskii equation. We briefly discuss in this section the diagrammatic approach following the references [59, 106, 107]. The starting point is the integral form of the Gross-Pitaevskii equation (Eq. 5.12) in the stationary case:

$$\Psi(\mathbf{r}) = \Psi_0\, e^{ikx} + \int \mathrm{d}\mathbf{r}'\; G_0^R(\mathbf{r},\mathbf{r}')\;\left[V(\mathbf{r}') + \tfrac{\hbar^2}{2m} g|\Psi(\mathbf{r}')|^2\right]\;\Psi(\mathbf{r}'). \tag{5.17}$$

This is the solution of the Gross-Pitaevskii equation with the boundary condition of an incident plane wave with amplitude ψ_0 along the x-direction. In the following, we restrict the discussion to a slab geometry. G_0^R is the free retarded Green function:

$$G_0^R(\mathbf{r},\mathbf{r}') \;=\; -i\frac{m}{2\hbar^2}H_0(k|\mathbf{r}-\mathbf{r}'|). \tag{5.18}$$

In the case of weak nonlinearity $\frac{\hbar^2}{2m}g\overline{|\Psi(\mathbf{r})|^2}\,\sqrt{k\ell_s} \ll \mu$ the equation Eq. 5.17 can be solved self-consistently by iteration, and we can already extract the building blocks for the diagrammatic approach:

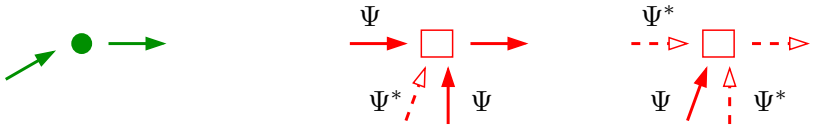

(5.19)

The first diagram corresponds to the usual linear scattering event due to the disorder potential. The second diagram arises from the nonlinear wave equation. Due to the term $g|\Psi(\mathbf{r})|^2$ two additional incoming lines appear, one from Ψ and the other from Ψ^*. Here solid lines correspond to Ψ (or G^R) and dashed lines to Ψ^* (or G^A). The last diagram is the complex conjugate of the second one. Eq. 5.17 can be similarly written for the complex conjugate Ψ^*, and in this situation the third diagram appears.

In the next step we consider the disorder average. First of all we restrict the discussion to isotropic scattering $\overline{V(\mathbf{r})V(\mathbf{r}')} \propto \delta(\mathbf{r}-\mathbf{r}')$, and additionally to weak scattering, such that $k\ell_s \gg 1$. In this limit all the transport length scales coincide $\ell_s \approx \ell_B \approx \ell_{tr}$. In the disorder average always a pair of Ψ and Ψ^* have to be grouped together, other contributions vanish in the stationary phase approximation. In this case we have to take into account ladder diagrams and for the interference effects for coherent backscattering the Cooperon diagrams. Below we want to describe first the Diffuson and then the Cooperon.

Contribution of the nonlinear Diffuson

For the ladder diagrams the propagation lines are grouped such that all lines point in the same direction. An example for such a process is depicted in Fig. 5.12 a. To develop a diagrammatic approach we notice that any nonlinear ladder diagram can be composed from the building blocks L_a and L_b, as shown in Fig. 5.12 b, and additional linear scattering events. But also the opposite is true, all combinations of L_a and L_b result in the full set of ladder diagrams. The nonlinear contribution $\overline{G^{nl}}$ to the average Green function arising from the diagram L_a can be approximated in lowest order of the nonlinearity g by

$$|\overline{G^{R,nl}}(\mathbf{r}_1,\mathbf{r}_2)|^2 \;=\; 2g\,\tfrac{\hbar^2}{2m}\int d\mathbf{r}_3\,\overline{G^R}(\mathbf{r}_1,\mathbf{r}_3)\,\overline{G^R}(\mathbf{r}_3,\mathbf{r}_2)\,\overline{G^A}(\mathbf{r}_1,\mathbf{r}_2)\,\overline{|\Psi(\mathbf{r}_3)|^2} \tag{5.20}$$

$$\simeq\; -igk\,|\mathbf{r}_1-\mathbf{r}_2|\,|\overline{G^R}(\mathbf{r}_1,\mathbf{r}_2)|^2\,\langle|\Psi|^2\rangle_{\mathbf{r}_1\to\mathbf{r}_2}/k^2\,. \tag{5.21}$$

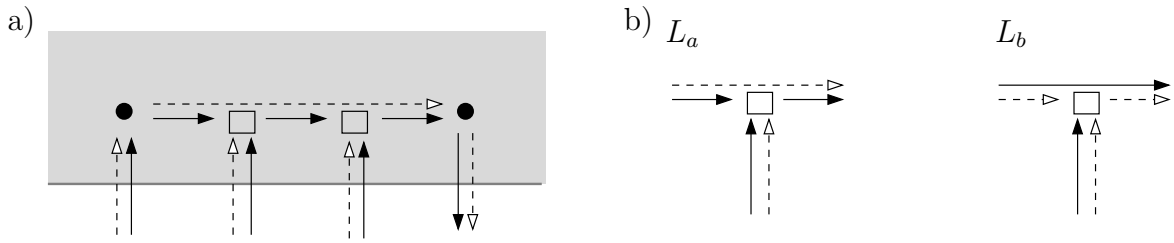

Figure 5.12: a) Example for a nonlinear ladder diagram. The points denote a linear scattering event, and the squares a nonlinear scattering event. The lines that belong together point all in the same direction. b) Building blocks for the nonlinear scattering events. All nonlinear Diffuson diagrams can be extracted from these building blocks and vice versa.

Here we consider a nonlinear propagation from $\mathbf{r}_1$ to $\mathbf{r}_2$ with a nonlinear scattering event at $\mathbf{r}_3$. At $\mathbf{r}_3$ the intensity $\overline{|\Psi(\mathbf{r}_3)|^2}$ modifies the index of refraction. In Eq. 5.21 we denoted the average of $|\Psi(\mathbf{r})|^2$ along the line $\mathbf{r}_1 \to \mathbf{r}_2$ with $\langle|\Psi|^2\rangle_{\mathbf{r}_1\to\mathbf{r}_2}$. The approximation in Eq. 5.21 was obtained with a stationary phase argument, where the disorder averaged Green function, arising just from linear scattering events, is given by:

$$\overline{G^R}(\mathbf{r},\mathbf{r}') = -i\frac{m}{2\hbar^2}\, H_0(k|\mathbf{r}-\mathbf{r}'|)\, \mathrm{e}^{-|\mathbf{r}-\mathbf{r}'|/2\ell_s} \overset{kr\gg 1}{\approx} -\frac{m}{\hbar^2}\, \frac{\mathrm{e}^{i(k|\mathbf{r}-\mathbf{r}'|+\frac{\pi}{4})}}{\sqrt{2\pi k|\mathbf{r}-\mathbf{r}'|}}\, \mathrm{e}^{-|\mathbf{r}-\mathbf{r}'|/2\ell_s}. \quad (5.22)$$

The condition for weak nonlinearity $g^2|\Psi(\mathbf{r})/k|^4 k\ell_s \ll 1$ ensures that at most one nonlinear event occurs between two linear scattering events. That means in other words that the scattering from the fluctuations arising due to the nonlinearity is small compared to scattering from the disorder potential [108, 109]. The self-consistent diffusion equation for the average intensity $\overline{|\Psi(\mathbf{r})|^2}$ is then modified by the nonlinearity in the following form:

$$\begin{aligned}\overline{|\Psi(\mathbf{r})|^2} &= |\Psi_0|^2 \mathrm{e}^{-x/\ell_s} + \int d\mathbf{r}' \frac{\mathrm{e}^{-|\mathbf{r}-\mathbf{r}'|/\ell_s}}{2\pi\ell_s|\mathbf{r}-\mathbf{r}'|}\overline{|\Psi(\mathbf{r}')|^2}\left(1 - i(g-g^*)k|\mathbf{r}-\mathbf{r}'|\langle|\Psi|^2\rangle_{\mathbf{r}_1-\mathbf{r}_2}/k^2\right) \\ &= |\Psi_0|^2\, \mathrm{e}^{-x/\ell_s} + \int d\mathbf{r}'\, \frac{\mathrm{e}^{-|\mathbf{r}-\mathbf{r}'|/\ell_s}}{2\pi\ell_s|\mathbf{r}-\mathbf{r}'|}\, \overline{|\Psi(\mathbf{r}')|^2}. \quad (5.23)\end{aligned}$$

The term proportional to g in the first line of Eq. 5.23 corresponds to the nonlinear diagram L_a and the term g^* arises from diagram L_b. Since we consider the case of real g, this contribution vanishes. Therefore, in the energy conserving case of real g the intensity distribution does not change due to nonlinear scattering in this order of approximation. On the contrary, in the case of an absorbing medium, with an imaginary g or in the case of amplifying media (random lasers [110]), the nonlinearity would yield modifications in the intensity distribution [111]. The probability to leave the disorder region after the last nonlinear event is then given by the intensity multiplied

with the exponential damping with the scattering mean free path. For the diffusive backscattered current follows:

$$j_d = \int \frac{d\mathbf{r}}{\ell_s |\Psi_0|^2 W} \, \mathrm{e}^{-x/\ell_s} \, \overline{|\Psi(\mathbf{r})|^2}. \tag{5.24}$$

Contribution of the nonlinear Cooperon

Now we consider the case of the Cooperon intensity. As we saw in the previous section we expect substantial modifications arising from the nonlinear crossed diagrams. A crossed diagram consists of one pair of counter propagating paths, as shown in Fig. 5.13a. Similar to the ladder diagrams we can specify building blocks. Every crossed diagram can be assembled from the building blocks as depicted in Fig. 5.13 b. However the contrary is not true. Not every combination of the building blocks C_a, C_b, C_c and C_d is a valid crossed diagram. An example of a *forbidden diagram* is shown in Fig. 5.14. When going back to the integral form of the Gross-Pitaevskii equation Eq. 5.17, which is expanded by iteration, we see that such a loop between C_c and C_d is not allowed by causality. A loop between those diagrams, where each diagram serves as source for the other, is not possible. In order to account for this forbidden diagram, we exclude all combinations in the summation, where a diagram C_c appears in the iterative expansion after C_d. To this end we split up the Cooperon part

$$C(\mathbf{r}) = C_1(\mathbf{r}) + C_2(\mathbf{r}) \, , \tag{5.25}$$

where C_1 contains only diagrams of C_a, C_b and C_c. C_2 is a self-consistent equation for the diagrams for C_a, C_b and C_d, and additionally C_1 can enter as source into C_2. This

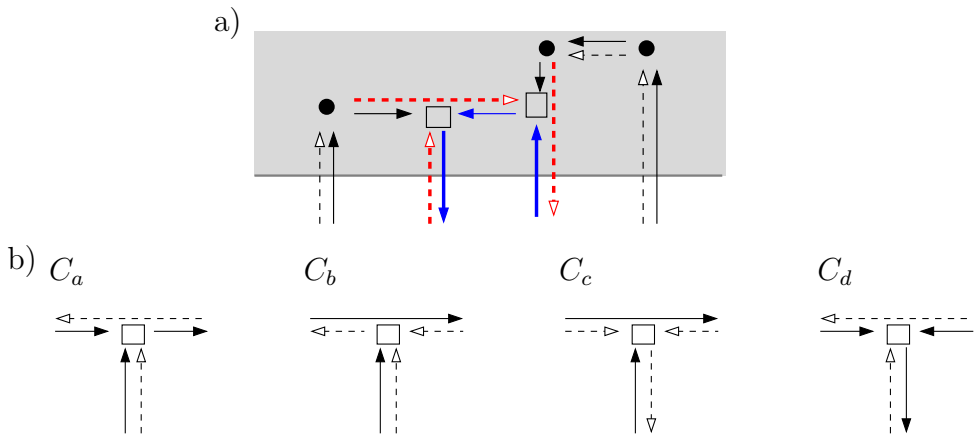

Figure 5.13: a) Example for a nonlinear crossed diagram. There is one path with counter propagating waves. b) Building blocks for the nonlinear scattering events contributing to the Cooperon. All Cooperon diagrams can be assembled from these building blocks.

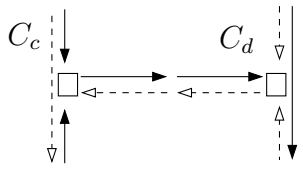

Figure 5.14: This *forbidden diagram* does not appear in the iterative expansion of Eq. 5.17.

assures that no C_c can appear after C_d:

$$\begin{aligned} C_1(\mathbf{r}) &= |\Psi_0|^2 \mathrm{e}^{-x/\ell_s} + \int d\mathbf{r}' \frac{\mathrm{e}^{-|\mathbf{r}-\mathbf{r}'|/\ell_s}}{2\pi\ell_s|\mathbf{r}-\mathbf{r}'|} C_1(\mathbf{r}') \left[1 - k\ell_s\big(i(g-g^*) - ig^*\big)\frac{\overline{|\Psi(\mathbf{r}')|^2}}{k^2}\right] , \\ C_2(\mathbf{r}) &= \int d\mathbf{r}' \frac{\mathrm{e}^{-|\mathbf{r}-\mathbf{r}'|/\ell_s}}{2\pi\ell_s|\mathbf{r}-\mathbf{r}'|} \left[C_2(\mathbf{r}') - k\ell_s\Big(C_2(\mathbf{r}')\big(i(g-g^*)+ig\big) + igC_1(\mathbf{r}')\Big)\frac{\overline{|\Psi(\mathbf{r}')|^2}}{k^2}\right] \\ j_c &= \int \frac{d\mathbf{r}}{\ell_s|\Psi_0|^2 W}\, \mathrm{e}^{-x/\ell_s} \left(C_1(\mathbf{r}) + C_2(\mathbf{r}) - \mathrm{e}^{-x/\ell_s}\right) . \end{aligned} \tag{5.26}$$

Here the factors $i(g-g^*)$ correspond to C_a and C_b, the factor $-ig^*$ (in the equation for C_1) to C_c and the factor ig (in the equation for C_2) is associated with C_d. The last line in the above equations is the Cooperon contribution to the backscattered current. Here a factor e^{-x/ℓ_s} has to be subtracted to exclude single scattering. For simplicity we assumed, that $\mathbf{r}$ and $\mathbf{r}'$ are far inside the medium to be able to neglect boundary effects, and also that $\overline{|\Psi(\mathbf{r})|^2}$ and $C_{1,2}(\mathbf{r})$ vary on length scale much larger than ℓ_s.

In the energy conserving case (real g) the above equations can be rewritten in the following form:

$$C(\mathbf{r}) = |\Psi_0|^2 e^{-x/\ell_s} + \int \mathrm{d}\mathbf{r}' \, \frac{e^{-|\mathbf{r}-\mathbf{r}'|/l_s}}{2\pi\ell_s|\mathbf{r}-\mathbf{r}'|} C(\mathbf{r}') \, \left(1 - igk\ell_s\langle|\Psi^2(\mathbf{r}')|\rangle/k^2\right) , \tag{5.27}$$

$$j_C = \int \frac{\mathrm{d}\mathbf{r}}{|\Psi_0|^2 W\ell_s} \, e^{-x/\ell_s} \, \Re\left[C(\mathbf{r}) - e^{-x/\ell_s}\right] . \tag{5.28}$$

From this equations we see that the Cooperon equation acquires a phase factor due to the nonlinearity g. Since for the outgoing wave the intensity depends on the real part of the Cooperon, the intensity is reduced, and can also become negative. This shows qualitatively the same behavior as we found in our numerical simulations in the previous chapter.

This derivation can only account qualitatively for the phenomenon of the inversion of the peak height. But it shows, that the reduction of the peak height results from a coherent effect, which allows also a negative contribution. This is in contrast to

"dephasing processes" which lead to a suppressed coherent contribution, but this is never negative. However, in order to compare quantitatively with our numerical simulations, boundary effects and the variation of the intensity has to be taken into account. Furthermore, nonlinear processes can take place to the left of the disorder potential (see Fig. 5.6 for the setup of the system). This can be incorporated and the resulting equations were derived by T. Wellens [112], which we present in the Appendix A. A simplified version [59, 107], where especially the contribution C_2 is neglected, is given by

$$C_c(x) = |\psi_0|^2 e^{-\hat{x}/\ell_s}\left(1+\frac{i}{k}\int_{x_0}^{x} dx' g(x') C_1(x')\right), \tag{5.29}$$

$$\begin{aligned} C_1(x) = \int_0^L \frac{dx'}{\pi\ell_s}\Bigg[& K_0\left(\left|\frac{\hat{x}-x'}{\ell_s}\right|\right)\Big(C_1(x')+C_c(x')\Big) + \\ & + \frac{i}{k} K_1\left(\left|\frac{\hat{x}-x'}{\ell_s}\right|\right)\langle|\psi(x')|^2\rangle \int_{\min(x,x')}^{\max(x,x')} dx'' g(x'')\Big(C_1(x'')+C_c(x'')\Big)\Bigg] \end{aligned} \tag{5.30}$$

for the Cooperon intensity $C_1(x)$ and the coherent Cooperon intensity $C_c(x)$, with $\hat{x} \equiv \max(x,0)$ and $K_{0,1}$ the modified Bessel functions of the second kind. The contribution to the flux scattered in backward direction then results in

$$j_c(0) = \Re\int_0^L \frac{dx}{\ell_s|\psi_0|^2} e^{-x/\ell_s}\left(C_1(x) + \frac{i}{k}\langle|\psi(x)|^2\rangle\int_{x_0}^{x} dx' g(x') C_1(x')\right). \tag{5.31}$$

Note that nonlinear processes also occur for $x_0 < x < 0$ where $V(\mathbf{r}) = 0$ but $g(x) > 0$. From this derivation developed by T. Wellens and B. Grémaud one can also deduce, that the same effect is expected for attractive interaction, which corresponds to a negative nonlinearity strength g.

5.5 Comparison with diagrammatic theory and further numerical results

In this section we compare our numerical results for coherent backscattering with the diagrammatic approach presented in the previous section. The equations arising from the diagrammatic approach were numerically solved by T. Wellens, and the results agree well with our numerical observations. In addition we want to show with our numerical simulations that the novel effect that the coherent backscattering cone reverts into a dip for increasing nonlinearity g is applicable for a quite large range of parameters. We furthermore investigate whether this phenomenon is influenced by the geometry of the two-dimensional waveguide, especially when the Bose-Einstein

condensate is transferred into the waveguide. Additionally, the impact of the disorder correlation length and moreover the type of disorder correlation function onto the backscattered current distribution is discussed.

5.5.1 Cone height

We start our discussion with the comparison of the current in exact backward direction $j(\theta = 0)$. As already presented in Sec. 5.3 we observe that the coherent backscattering peak changes with increasing nonlinearity strength g from a cone in the linear case to a flat profile and then to a dip. The same qualitative behavior is indeed also expected from the diagrammatic approach. Now we compare our numerical calculation quantitatively with the diagrammatic theory. The results of this relation – the parameters are listed below – are presented in Fig. 5.15. The points denote the numerically calculated current in backward direction as a function of the nonlinearity strength, where the error bars show the statistical standard deviation arising from the average over $\sim 10^3$ disorder realizations. The blue dashed line shows the diffusive contribution j_d to the backscattered current from the diagrammatic approach as given in Eq. 5.24. The diffusive contribution does not change with the nonlinearity g, because we saw in the previous section, that the intensity profile $\overline{|\psi(\mathbf{r})|^2}$ is not affected in lowest order by the nonlinearity (see Eq. 5.23). The red dotted line in Fig. 5.15 shows the total backscattered current $j(\theta{=}0) = j_d + j_c(\theta{=}0)$, where the current arising from the Cooperon is given by Eq. 5.31. As explained in the previous section this is an approximation to the full set of equations given in App. A, which result in the current shown by the red solid line.

For the simulation we used the same parameters as in Sec. 5.3. Especially we consider a Gauss correlated disorder potential with a small correlation length $k\sigma = 0.5$, which results in almost isotropic scattering. This is needed to compare to the analytical theory, which is valid only for isotropic scattering. For the strength of the disorder potential we use $V_0 = 0.614\mu$. This results in a scattering mean free path of $k\ell_s \approx 9.61$ and a transport mean free path $k\ell_B \approx k\ell_{tr} \approx 9.75$. This confirms the isotropic scattering condition ($\ell_s \approx \ell_{tr}$). For the optical thickness b of the slab geometry we used $b = L/\ell_s = 4.2$ ($kL = 40$) and a width of $kW = 120$. The nonlinearity strength $g(x)$ as a function of x is shown in Fig. 5.7.

In general we see good agreement between our numerical results and the diagrammatic approach in Fig. 5.15. We observe a vanishing peak at the nonlinearity strength $g \simeq 0.01$ and at $g \simeq 0.02$ we find clearly a negative Cooperon contribution. All three curves for the total current show the same overall behavior. The two curves from diagrammatic theory coincide at small nonlinearity and then deviate. Nevertheless the main contributions from the full equations (solid red line, App. A) are captured in the

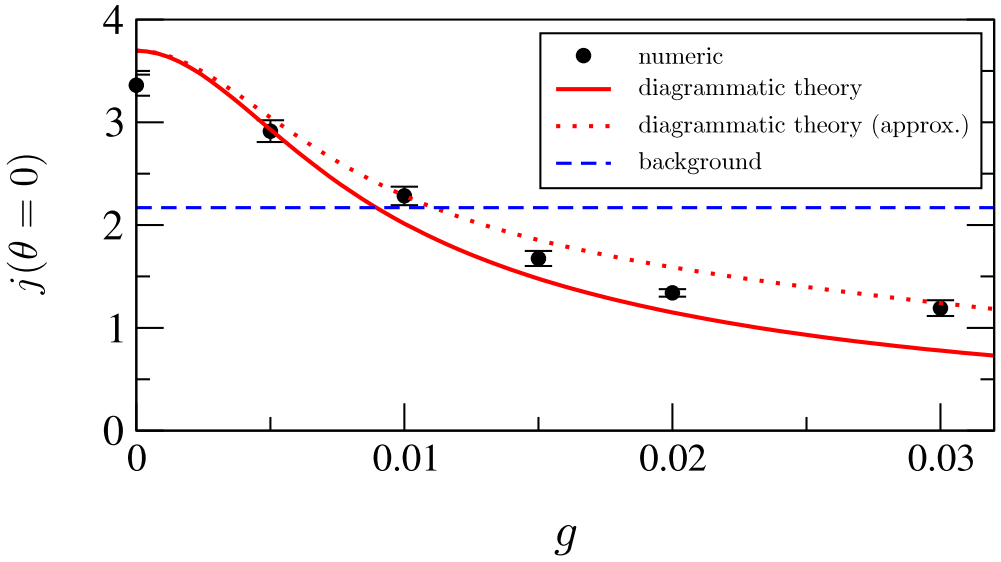

Figure 5.15: Comparison of the current scattered in exact backward direction ($\theta = 0$) as a function of the nonlinearity strength g. The black dots correspond to the current extracted from the numerical solution of the Gross-Pitaevskii equation, where the error bars denote the statistical standard deviation. The red curves present the results from the diagrammatic approach from the previous section. The diffusive contribution j_d (Eq. 5.24) is given by the blue dashed line. The solid red line shows the total current $j = j_d + j_c$ from the full set of equations (App. A), and the dotted red line the approximation to this equation, as stated in Eq. 5.31 and Eq. 5.24. In overall we see good agreement. Parameters: $kL = 40$, $kW = 120$, $j_{in} = \hbar k^3/m$, $k = \sqrt{2m\mu}/\hbar$, Gauss correlated disorder potential with $k\sigma = 0.5$ and $V_0 = 0.614\mu$, $g(x)$ as shown in Fig. 5.7.

approximation given in Eq. 5.31 (dotted red line). In comparison with the numerical results we see good agreement. Nevertheless we also see small deviations, which we explain in the following. We postpone the discussion of the differences in the last point $g \simeq 0.03$ to the next section, because they are fundamentally different from the following discussion. So we start with the discussions of the deviations in the linear case.

In the diagrammatic description the diffusion process is solved, which fulfills already current conservation, implying that the integral over the outgoing current over all angles - including forward direction - is equal to the incoming current. In our normalization this reads:

$$\int_0^{2\pi} d\theta \; j_d(\theta) = 2\pi(1 - \mathrm{e}^{-L/\ell_s}) \; . \tag{5.32}$$

where the last term accounts for the coherent mode leaving the disorder region in forward direction without any scattering event. Note that the diffusive intensity depends

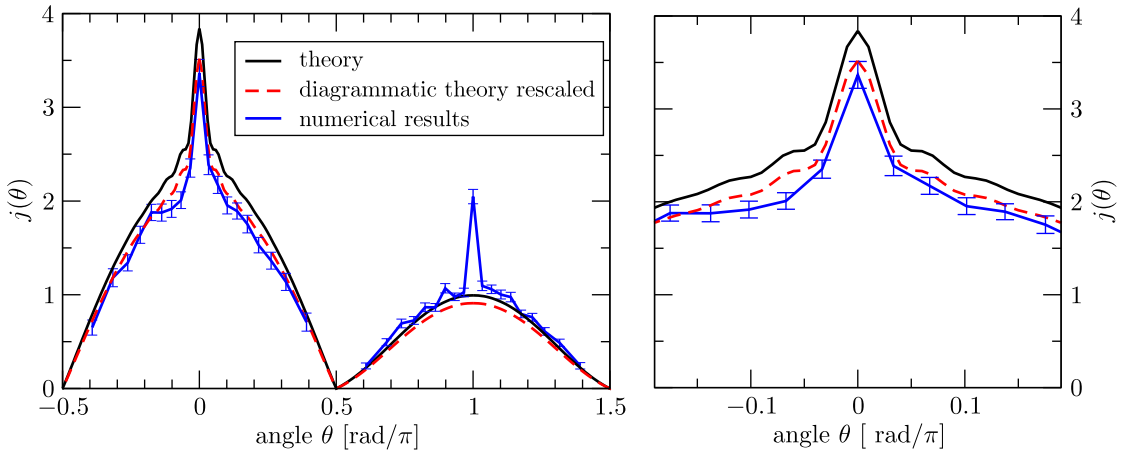

Figure 5.16: Comparison between the numerical (blue line) and diagrammatic (black line) angular resolved current. Angles with $\theta > \pi/2$ correspond to scattering in forward direction. Since the diagrammatic prediction does not obey current conservation we rescale the curve by an angle independent factor. This results in the red dashed curve, which is in much better agreement with our numerical results. Parameters: $kL = 40$, $j_{in} = \hbar k^3/m$, $k = \sqrt{2m\mu}/\hbar$, Gauss correlated disorder potential with $k\sigma = 0.5$ and $V_0 = 0.614\mu$, $k\ell_s = 9.6$. The right panel shows the region $\theta = -0.2 \ldots 0.2$ in more detail.

on the angle only due to geometrical reasons, which means that the angular profile is shaped cosine-like due to the smaller effective width of the slab for larger angles. In addition to this Diffuson part the Cooperon contribution is calculated. This implies, that current conservation is not fulfilled anymore for the total current $j = j_d + j_c$. In order to see the influence of this effect we rescaled the diagrammatic result by an angle independent factor α such that current conservation is restored:

$$\int_0^{2\pi} d\theta\, \alpha\Big(j_d(\theta) + j_c(\theta)\Big) = 2\pi(1 - \mathrm{e}^{-L/\ell_s})\,. \tag{5.33}$$

Of course this can only be seen as a first order approximation, and for a detailed study higher order coherent contributions, namely Hikami contributions [87, 113], have to be taken into account, which are responsible to restore current (or equivalently energy) conservation in the coherent part. It was shown [114] that the coherent multiple scattering contribution is adjusted downwards at all angles with a larger negative shift at angles near backward direction.

The angular dependence of the current is shown in Fig. 5.16 for the linear case. In the left plot the full angular dependence of the current is shown, including the forward direction ($\theta > \pi/2$), and in the right graph a zoom to small angles in backscattering direction is presented. The blue line shows the numerical results and the black line the diagrammatic prediction. The rescaled curve from diagrammatic theory, which

now obeys current conservation, is shown as a red, dashed line. We observe that the rescaled curve shows much better agreement with the numerical results. Therefore we attribute the discrepancies in Fig. 5.16 at $g = 0$ between numerical and diagrammatic results to the approximations used in the diagrammatic description.

For stronger nonlinearity we expect similar deviations, but in the opposite direction. For the diagrammatic results, we consider in the following the results arising from the full set of equations (see App. A). In the linear case the theory overestimates the total outgoing current, due to the constructive interference leading to the increased backscattering cone. In the same way the theory underestimates the total current for the destructive interference leading to the dip structure in the angular resolved current. In the last case a renormalization of the diagrammatically predicted current would yield a higher current in direction $\theta = 0$. To this end we expect that the theory overestimates the current in the linear case at $g = 0$, is in good agreement at a vanishing cone ($g \simeq 0.01$), and underestimates the current at the nonlinearity $g \simeq 0.02$, at the position of the dip. We observe exactly this behavior between the numerical results (black dots) and the results from diagrammatic theory (solid red line, full set of equations) in Fig. 5.15.

5.5.2 Influence of the width of the disorder sample

In our numerical simulation, we always have to take a finite width W of the simulation region into account as presented in Fig. 5.7. We numerically checked whether this width influences the coherent backscattering effect. Since we have periodic boundary conditions the wave can go in y-direction a length W and then interfere with itself. This would be an artifact of our numerical simulation not encountered in an experimental setup. Therefore we checked the dependence of the angular resolved current for two widths, $kW_1 = 120$ as in the previous calculations, and $kW = 40$, where both have the same length of the disorder region, $kL = 40$. The most obvious difference is of course the angular resolution $\Delta\theta$ of the current:

$$\Delta\theta \approx \sin(\Delta\theta) = \frac{\Delta k_y}{k} = \frac{2\pi}{kW}. \tag{5.34}$$

This angular resolution is also important in an experimental setup in order to be able to resolve the angular width of the coherent backscattering cone. This is clearly recognized in Fig. 5.17, which shows the angular resolved current in backward direction $\theta < \pi/2$ and in forward direction $\theta > \pi/2$, in the linear regime ($g = 0$). The two curves coincide very nicely. Especially in backward direction of the coherent backscattering cone there are no deviations observed, although the angular resolution is not enough to show the details of the peak structure. However we see differences in the current in forward direction, moreover the peak height in forward direction changes. However, this is to be

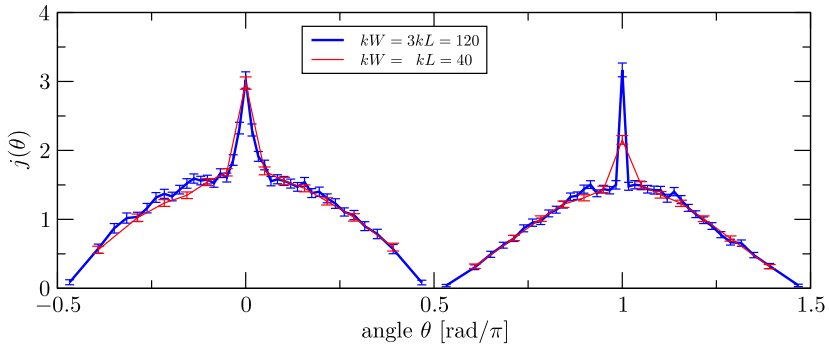

Figure 5.17: Angular resolved current in backward and forward direction in the linear case, from our simulation. We observe no difference in the current distribution for different widths of the disorder region, except in forward direction. This arises from the vanishing angular width of the coherent mode. The same overall behavior is observed in the nonlinear regime.

expected. The origin of this peak is the coherent mode $\overline{|\Psi(x,y)|^2} \propto \exp(-x/\ell_s)$. Due to the finite length of the disorder region some part of the condensate can go through the disorder region without any scattering event. Since the coherent mode is observed strictly in forward direction, i.e. it has no width in contrast to the backscattering cone, the height of the coherent part should scale with $1/\Delta\theta \propto W$. We estimate from Fig. 5.17 the height of the coherent mode j_0 on top of the diffusive background in the case of $kW = 40$ to $j_0 \approx 0.6 \pm 0.1$ and in the case of $kW = 120$ to $j_0 \approx 1.6 \pm 0.15$, which is in agreement within the error bars compared to an expected factor of 3.

Here we have shown only the comparison in the linear case. But the results are equally applicable for the nonlinear regime. We did not find any significant deviations there.

5.5.3 Nonlinear density distribution and coherent mode

Now we turn to how the nonlinearity modifies the scattering mean free path. To this end we calculate the coherent mode $|\overline{\Psi(\mathbf{r})}|^2$ in the disorder potential. This coherent mode is shown in Fig. 5.18, with the characteristic exponential decay. For the nonlinearity strength under consideration we do not observe any significant deviations from the linear case. We conclude that the scattering mean free path is unchanged.

For the intensity distribution $\overline{|\Psi(\mathbf{r})|^2}$ the diagrammatic description predicts no changes arising due to the nonlinearity. This can be confirmed with our numerical simulations. As we see in Fig. 5.18 the intensity distribution $\overline{|\Psi(\mathbf{r})|^2}$ is only very slightly affected by changes in the nonlinearity, in contrast to the coherent backscattering peak. We especially observe a good agreement between the diffusive calculation (see Sec. 4.3.2)

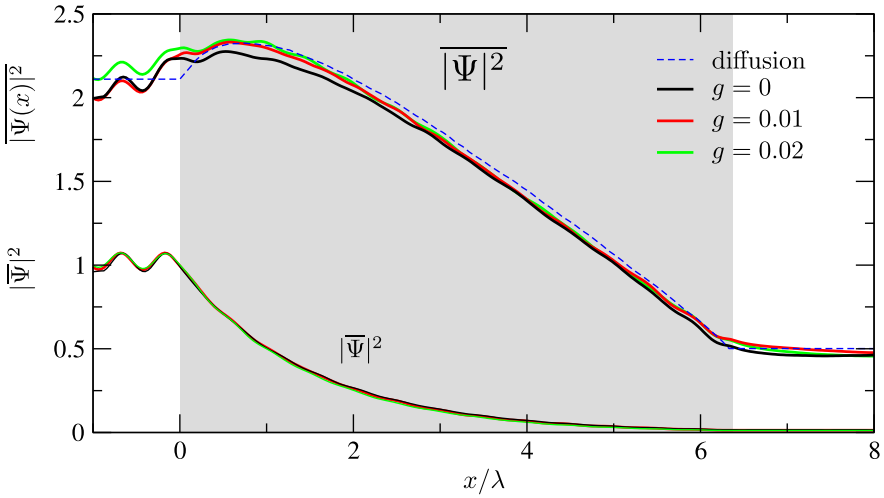

Figure 5.18: The coherent mode $|\overline{\Psi(\mathbf{r})}|^2$ is not affected by the nonlinearity. The intensity distribution $\overline{|\Psi(\mathbf{r})|^2}$ is also almost unchanged, as predicted by theory. Parameters: $kL = 40$, $kW = 120$, $j_{in} = \hbar k^3/m$, $k = \sqrt{2m\mu}/\hbar$, Gauss correlated disorder potential with $k\sigma = 0.5$ and $V_0 = 0.614\mu$, $g(x)$ as shown in Fig. 5.7.

and the nonlinear curve at $g = 0.01$, where the peak vanishes. This is compared to a slightly smaller intensity in the linear case, which is necessary to compensate the coherent backscattering peak for current conservation, which results in a reduced background of backscattered intensity, according to

$$j_d = \int \frac{d\mathbf{r}}{\ell_s |\Psi_0|^2 W} \, \mathrm{e}^{-x/\ell_s} \, \overline{|\Psi(\mathbf{r})|^2}. \tag{5.35}$$

Nevertheless the deviations are very small and probably difficult to measure in an experimental realization.

Similarly, the transmission current through the disordered system is almost unaffected by the nonlinearity, as shown in Fig. 5.19. We observe a very slight increase of the current from peak ($g = 0$) to dip ($g = 0.03$), which is in the same order as the current contained in the coherent backscattering cone ($\sim 6\%$). In conclusion we see only slight changes, which we think are not easily accessible in an experiment with a Bose-Einstein condensate, at least in the weak localization regime with weak nonlinearity.

5.5.4 Influence of the transverse confinement of the waveguide

In the following we discuss the influence of the experimental geometry onto the nonlinear coherent backscattering effect. Especially we show that the nonlinear region in

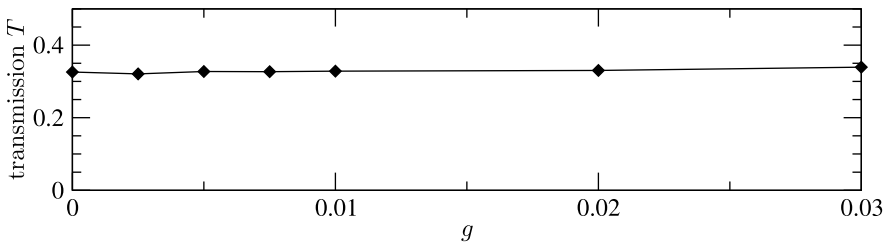

Figure 5.19: Transmission through the two-dimensional disorder region as a function of the nonlinearity strength. The same parameters as in Fig. 5.18 are used.

front of the disorder region is quantitatively changing the results, but not qualitatively. We study a system where a three-dimensional droplet of Bose-Einstein condensate is transferred by an adiabatic increase of the confining potential in z-direction into the effective two-dimensional system. The situation is shown in Fig. 5.20. In the mean-field description for the condensate we use the Gross-Pitaevskii equation:

$$i\hbar\frac{\partial}{\partial t}\Psi(\mathbf{r},t) = \left(-\frac{\hbar^2}{2m}\Delta + V(\mathbf{r}) + \frac{\hbar^2 g(x)}{2m}|\Psi(\mathbf{r},t)|^2\right)\Psi(\mathbf{r},t) + S(\mathbf{r})\,\mathrm{e}^{-i\mu t/\hbar}, \quad (5.36)$$

where the nonlinearity g is given by:

$$g(x) = \frac{4\sqrt{2\pi}a_s}{a_\perp(x)}\,, \qquad \text{with} \qquad a_\perp(x) = \sqrt{\hbar/[m\omega_\perp(x)]}\,. \quad (5.37)$$

Here a_s is the s-wave scattering length, $a_\perp$ is the transverse confinement, and $\omega_\perp$ the corresponding frequency of the confinement when approximated by a harmonic

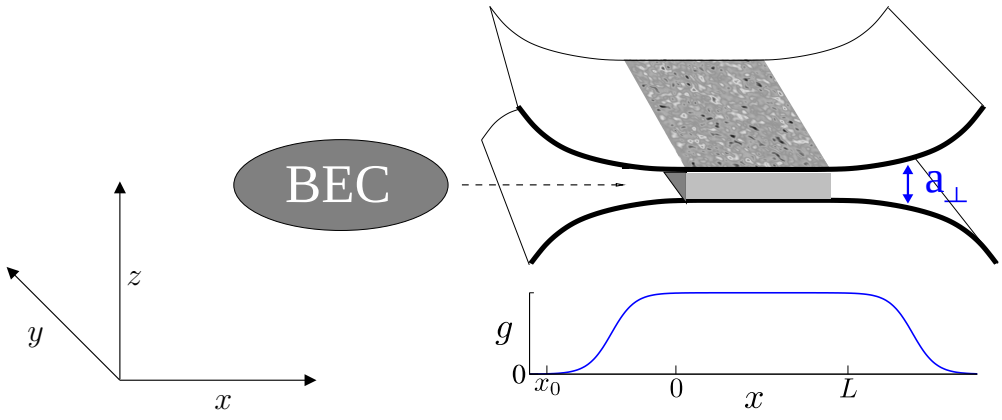

Figure 5.20: A wave packet of Bose-Einstein condensate is transferred into the two-dimensional confinement. In this case the nonlinearity $g(x) = 4\sqrt{2\pi}a_s/a_\perp(x)$ depends through $a_\perp(x)$ on the position x. The corresponding nonlinearity g is shown.

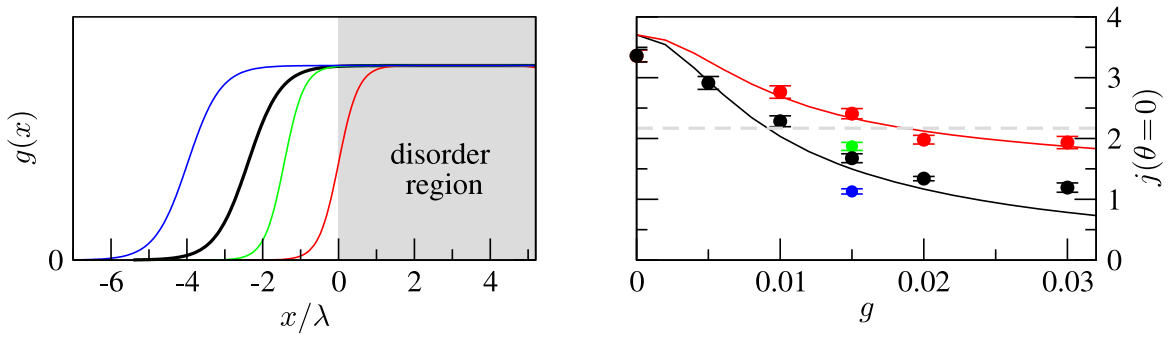

Figure 5.21: Dependence of the current in backward direction on the length of the nonlinear region in front of the disorder region. The nonlinearity strength of the black (red, blue and green) curve in the left graph corresponds to the black (red, blue and green) points (numeric) and the black (red) line (diagrammatic theory) in the right graph, where the current in exactly backward direction is shown. The gray dashed line in the right graph shows the diffusive background for comparison. Parameters: $kL = 40$, $kW = 120$, $j_{in} = \hbar k^3/m$, $k = \sqrt{2m\mu}/\hbar$, Gauss correlated disorder potential with $k\sigma = 0.5$ and $V_0 = 0.614\mu$. The black line corresponds to parameters $kx_l = -15$, $kx_r = 55$, and $kx_{ad} = 3.5\pi$, which were used in all previous calculations.

oscillator. But in our situation this transverse confinement $a_\perp$ changes from a small value in the two-dimensional confinement to a very large value outside, where the droplet of condensate starts the propagation towards the disorder region, as depicted in Fig. 5.20. To this end the nonlinearity $g(x)$ varies due to the confining width $a_\perp(x)$ with the position x, as given in Eq. 5.37. For the numerical simulations we used the following functional dependence for $g(x)$:

$$g(x) = g_0 \ \frac{1}{2}\left(\tanh\left(\frac{2(x-x_l)}{x_{ad}}\right) - \tanh\left(\frac{2(x-x_r)}{x_{ad}}\right)\right) \ , \tag{5.38}$$

where x_l and x_r are the left and right positions for the adiabatic increase, and x_{ad} is the distance over which the adiabatic increase is performed and g_0 is the nonlinearity strength inside the disorder potential.

We performed simulations with different forms of the adiabatic increase of the nonlinearity. Especially we changed the position, where we start to increase the nonlinearity, as shown in the left graph of Fig. 5.21. We find that the current in backward direction ($\theta = 0$) is modified. In particular we find a stronger reduction of the current if the region in front of the disorder region is longer (black and blue points in Fig. 5.21). On the contrary, a larger nonlinearity strength is needed to reach a negative coherent backscattering contribution if the nonlinear region vanishes in front of the disorder potential (red points). The diffusive background is shown by the dashed gray line.

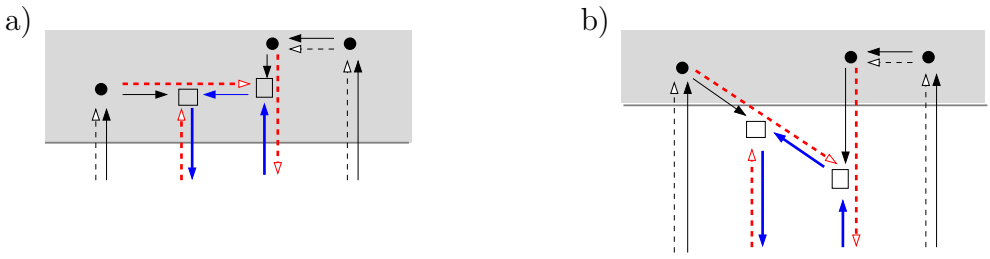

Figure 5.22: a) Diagram that contributes to the nonlinear coherent backscattering as described in Sec. 5.4. b) Nonlinear scattering events can also occur in front of the disorder region, and contribute to the backscattered current, in contrast to linear scattering events, which are pinned to the disorder region.

Nevertheless in all cases we find a dip in the angular resolved backscattered current for a strong enough nonlinearity strength.

Our numerical results are in good agreement with the predictions from diagrammatic perturbation theory. This is shown in the right graph of Fig. 5.21 with the solid red and black curve. Those were calculated by T. Wellens with the set of equations from App. A and the same functional dependence of the nonlinearity strength.

From those observations we conclude that it is important to include nonlinear scattering events also in front of the disorder region. This is in contrast to linear scattering events, which are pinned to the disorder region. A nonlinear crossed diagram is shown in Fig. 5.22 a, but this nonlinear events can occur also outside the disorder region, as shown in Fig. 5.22 b. This nonlinear region in front of the disorder potential effectively introduces an additional phase difference, which enhances the destructive interference.

In order to know the backscattered current we can state by following the diagrammatic perturbation theory, that the observed effects depend on $gk\ell_s\langle|\Psi^2(\mathbf{r}')|\rangle/\mu$ (see Eq. 5.27), where ℓ_s should be replaced by an effective length of the nonlinear scattering path, including the length in the nonlinear region in front of the disorder potential.

5.5.5 Nonlinear coherent backscattering for an anisotropic scattering potential

Here we want to show that the destructive interference in backscattering direction is also observed for a larger correlation length. To this end we used a Gauss-correlated disorder potential with a correlation length of $k\sigma = 1.0$. In Fig. 4.9 we see that this correlation length corresponds to anisotropic scattering with enhanced forward scattering. We used a disorder strength of $V_0 = 0.4\mu$. We extracted the scattering mean free path numerically and found $k\ell_s = 9.6$, and for the transport mean free path

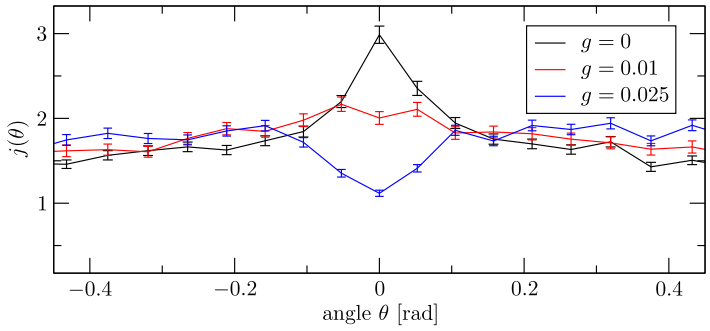

Figure 5.23: This plot confirms that the negative coherent backscattering contribution is also observed for anisotropic scattering. Here we used a correlation length of $k\sigma = 1$. Parameters: $kL = 40$, $j_{in} = \hbar k^3/m$, $k = \sqrt{2m\mu}/\hbar$, Gauss correlated disorder potential with $k\sigma = 1.0$ and $V_0 = 0.4\mu$, $k\ell_s = 9.6$, $k\ell_{tr} = 13.4$.

$k\ell_{tr} = 13.4$, resulting in a slightly larger cone width. In Fig. 5.23 we found the same effect of destructive interference for a nonlinearity strength $g = 0.025$. Therefore we conclude that this phenomenon of a negative coherent backscattering contribution is also observed for larger correlation lengths. A finite correlation length is relevant in an experimental setup, since the lower bound for the correlation length is given by the wave length of the laser, which produces the disorder potential.

Here we cannot compare with results from the diagrammatic approach to nonlinear coherent backscattering from Sec. 5.4, since this theory is only applicable to isotropic scattering, and has not been generalized to the case of anisotropic scattering.

5.5.6 Nonlinear coherent backscattering with a speckle disorder potential

For small correlation lengths one can argue that the details of the correlation function does not influence the coherent backscattering. In order to verify that the destructive interference effect also persists for an intermediate correlation length we performed numerical simulations for a speckle potential. The speckle disorder potential is of most interest from the experimental point of view, since it can be realized very easily by shining a laser on a diffusive plate, and then image this speckle pattern onto the experimental region.

To implement this we created randomly chosen realizations of speckle patterns and performed the same simulations as before. We used a correlation length of $k\sigma = 0.5$ and a strength of $V_0 = 0.614\mu$. This results in a scattering mean free path of $k\ell_s = 10.8$ and a transport mean free path of $k\ell_{tr} = 15$. We used a system size of $kL = kW = 40$ and

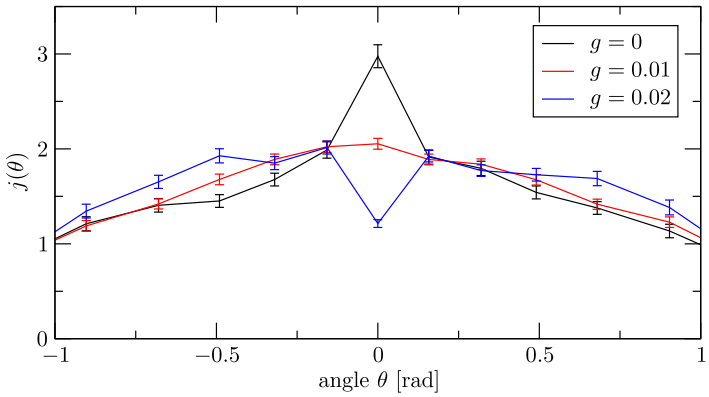

Figure 5.24: The inversion of the coherent backscattering peak applies also to a speckle potential, which is experimentally most easily accessible. Parameters: $kL = 40$, $j_{in} = \hbar k^3/m$, $k = \sqrt{2m\mu}/\hbar$, $x_l = -15$, $kx_r = 55$, $kx_{ad} = 3.5\pi$, speckle potential with $k\sigma = 0.5$ and $V_0 = 0.614\mu$, $k\ell_s = 10.8$. $k\ell_{tr} = 15$.

the same functional dependence of $g(x)$ as above. The results are shown in Fig. 5.24. We find that the phenomenon, where the coherent backscattering peak changes from constructive to destructive interference, is quite robust, and shows the same behavior for a speckle potential.

In conclusion we confirm that this interference phenomenon is quite robust under variation of system sizes, potential strength, correlation length, and also correlation function (Gauss and speckle) in the regime of weak localization.

5.6 Time-dependent effects in the transport process

In the course of this chapter we study nonlinear coherent backscattering. Thus, we simulate the propagation process with the time-dependent Gross-Pitaevskii equation. We start with an empty two-dimensional waveguide and couple the condensate with the additional source term, we added to the Gross-Pitaevskii equation, into the simulation region. In order to be as close as possible to a stationary scattering state we slowly increase the strength of the source up to a final value corresponding to the desired incoming current density. In the linear case this procedure guarantees to reach a stationary scattering state. For a nonlinear wave equation this is not true in general. In particular there can exist stationary scattering states, which are not dynamically stable [19]. With our time-dependent integration scheme of the Gross-Pitaevskii equation we are sensitive to instabilities, which are predicted by Ref. [108, 109].

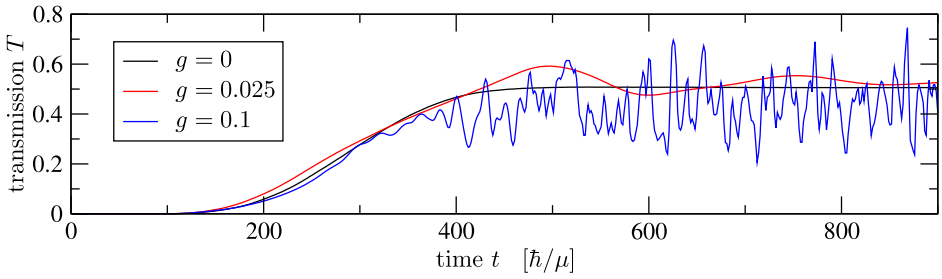

Figure 5.25: Time-dependent transmission through n individual disorder potential for different nonlinearity strength. The source is adiabatically increased over a time period of $t = 300\hbar/\mu$. For $g = 0.1$ we observe a strong intrinsic time-dependence of the transmission.

For a nonlinearity $g \gtrsim 0.02$ we find indeed that we do not reach a stationary state anymore. We observe that the time-dependent integration results in an intrinsically time-dependent dynamic of the condensate wave function, similar to the situation, which was found in one-dimensional waveguides with disorder potentials [19, 20]. In Fig. 5.25 we see that in the linear case the transmission converges to a final value, after an adiabatic increase of the source over a time scale of $t = 300\hbar/\mu$. In an intermediate regime ($g = 0.025$) we observe oscillations on a long time scale, which are damped in this case of the disorder realization. For strong nonlinearity we observe initial convergence, and when a critical interaction energy ($E_{nl} = g|\psi|^2\,\hbar^2/2m$) is reached time-dependent oscillations in the current start. Note that the critical strength for the nonlinearity depends on the disorder realization. Therefore we find a smooth transition from stationary scattering states to time-dependent scattering dynamics in the disorder average. This is presented in Fig. 5.26 in the lower panel, where the fraction of the disorder realizations that lead to a stationary scattering state is shown. In the upper panel the current in backscattering direction is shown. We see an increase in the backscattered intensity in direction $\theta = 0$. Deviations between numerical simulations and diagrammatic perturbation theory appear as soon as time-dependent processes start. This is expected, since the theory assumes a stationary solution (see Eq. 5.17).

In order to discuss the increased backscattered current we take a closer look to the angular resolved current, which is shown in Fig. 5.27. We find that the dip disappears and the overall shape of the current distribution changes quite drastically to a Gaussian shape. Until now we do not have a good explanation for this shape of the current distribution, therefore this needs further investigations.

Nevertheless we checked, whether this shape is related to coherent backscattering. To this end we calculated the angular resolved current in the case, where the direction of the incoming plane wave is tilted by an angle $\phi = -0.32$, as was done at the end of Sec. 5.3 in the stationary case (Fig. 5.11). In the case of coherent backscattering the

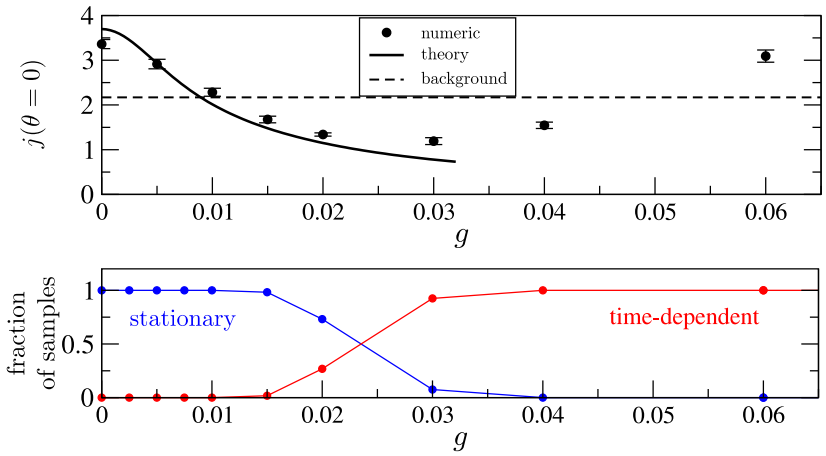

Figure 5.26: Upper graph: Comparison of the current scattered in exact backward direction ($\theta = 0$) as a function of the nonlinearity strength g. The dots correspond to the current extracted from the time-dependent integration of the Gross-Pitaevskii equation. The solid curves present the results from the diagrammatic approach. Lower graph: The blue line shows the fraction of the disorder realization which lead to a stationary scattering solution, whereas the red curve presents the time-dependent fraction. Parameters: $kL = 40$, $kW = 120$, $j_{in} = \hbar k^3/m$, $k = \sqrt{2m\mu}/\hbar$, Gauss correlated disorder potential with $k\sigma = 0.5$ and $V_0 = 0.614\mu$, $g(x)$ as shown in Fig. 5.7.

peak is observed in exactly backward direction, at $\phi = -0.32$, in contrast to specular reflection which is observed in this case at an angle $\phi = 0.32$. As already explained, the dip occurs in coherent backscattering direction, which verifies that the dip is an destructive interference effect (see Fig. 5.28). A different situation manifests in the

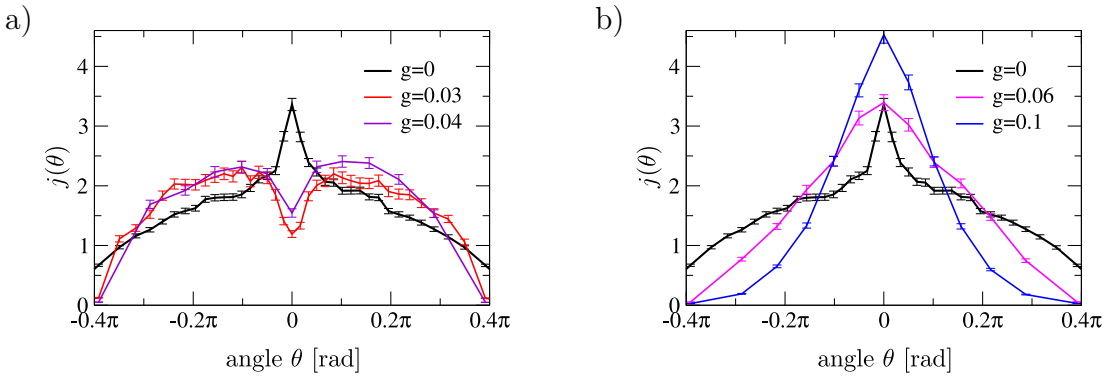

Figure 5.27: Angular resolved backscattered current. In the time-dependent regime the dip disappears. Parameters: $kL = 40$, $kW = 120$, $j_{in} = \hbar k^3/m$, $k = \sqrt{2m\mu}/\hbar$, Gauss correlated disorder potential with $k\sigma = 0.5$ and $V_0 = 0.614\mu$, $g(x)$ as shown in Fig. 5.7.

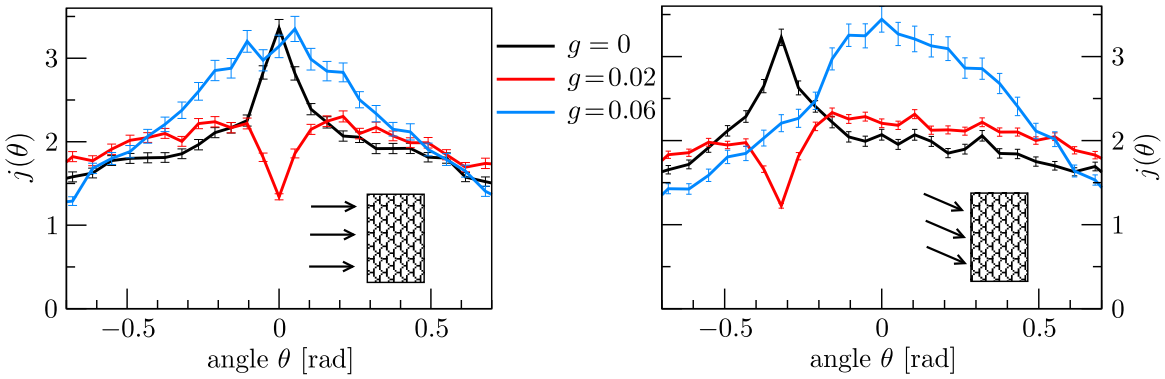

Figure 5.28: We compare the coherent backscattering in the case, where the incident wave enters the disorder region perpendicular (left graph) to the case where the incoming wave is tilted by an angle $\phi_{-6} \simeq -0.32$ (right graph). In the latter setup coherent backscattering is observed in retro-reflection. This is also observed in the weak nonlinear case ($g = 0.02$), which confirms, that both arise due to interference between time reversed paths. This is in contrast to specular reflection, where the peak appears at $\phi_{+6} \simeq +0.32$. In the time-dependent regime ($g = 0.06$) the center of the peak is at an positive angle, which shows that it is not related to coherent backscattering.

time-dependent regime, where the center of the reflected current is shifted to positive angles in the right graph of Fig. 5.28. This shows that we do not observe coherent interference effects. We actually expected this, because a constant phase difference between two scattering paths is a necessary condition for interference effects, which is destroyed in the time-dependent regime.

Finally it has to be discussed, whether the mean-field approximation is still valid in the time-dependent regime, or whether the condensate fraction is reduced and the thermal cloud is populated. In the limiting case of large density $|\Psi|^2 \to \infty$ but with constant $g|\Psi|^2 = const$ (i.e. $g \to 0$) the mean-field description is exact, and our results are valid. The case of a finite density has been investigated for one-dimensional systems [115], with a cumulant approach [116], which can account for the fact that atoms can scatter out of the condensate wave function. This can lead to a reduction of the condensate density, and can eventually also destroy the whole condensate. This has to be addressed especially in the time-dependent regime and needs further investigations. Adopting the approach [115] mentioned above for two-dimensional systems is numerically demanding, because it involves the time-dependent integration of two-point correlation functions for the non-condensed fraction, which are four-dimensional matrices for a two-dimensional system.

5.7 Intensity statistics of the wave functions

The last topic we address in this chapter is the subject of the statistical properties of the intensity of the wave functions. We show that we observe deviations from Rayleigh statistics [79] for the linear system ($g = 0$). The Rayleigh distribution is calculated by neglecting interferences. The discrepancy from this probability calculation is explained by crossing trajectories. These deviations have already been studied [117–119] and are in good agreement with our numerical calculations. But in the nonlinear regime we find quite significant differences. We begin with the description of the linear case and follow especially Ref. [117].

The probability distribution for the intensity $I(\mathbf{r}) = |\Psi(\mathbf{r})|^2$ is the probability for the occurrence of a specific intensity of the wave function at position $\mathbf{r}$ for a randomly chosen disorder realization. We assume for the remainder of the discussion that we are far inside the medium such that boundary effects can be neglected. In particular, the coherent mode $|\overline{\Psi(\mathbf{r})}|^2$ is already damped out. Otherwise the discussion has to be extended by the results from Ref. [120]. The Rayleigh distribution function is obtained from the following considerations: The amplitude Ψ of a wave at a given point is the sum over all amplitudes Ψ_α which arise from the scattering path α:

$$\Psi = \sum_\alpha \Psi_\alpha \; . \tag{5.39}$$

Next we calculate the nth moment of the intensity:

$$\overline{I^n} = \sum_{\substack{\alpha_1 \ldots \alpha_n \\ \beta_1 \ldots \beta_n}} \overline{\Psi_{\alpha_1} \ldots \Psi_{\alpha_n} \Psi^*_{\beta_1} \ldots \Psi^*_{\beta_n}} . \tag{5.40}$$

We now assume that all amplitudes Ψ_α acquire a different phase, and therefore only contributions arise for pairs of those wave functions with the same scattering path $\alpha = \beta$: $\overline{\Psi_\alpha \Psi^*_\beta} = \delta_{\alpha\beta}\, \overline{I}$. From combinatorial arguments we find that there are $n!$ such combinations, and we arrive finally at the relation for all moments:

$$\overline{I^n} = n!\, \overline{I}^n \; . \tag{5.41}$$

If all moments are known, the probability distribution can be calculated with the following relation [121]:

$$P(I) = \int_{-\infty}^{\infty} \frac{d\xi}{2\pi} \; \mathrm{e}^{i\xi I} \; \sum_{n=0}^{\infty} \frac{(-i\xi)^n}{n!} \, \overline{I^n} \; . \tag{5.42}$$

In the above case we recover the Rayleigh distribution

$$P(I) = \frac{1}{\overline{I}} \, \mathrm{e}^{-I/\overline{I}} \; . \tag{5.43}$$

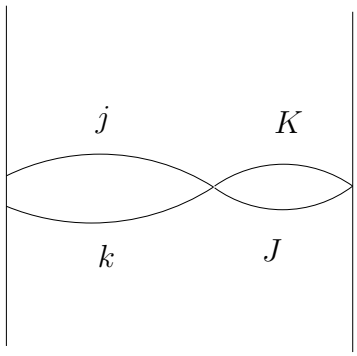

Figure 5.29: Scattering path for transmitted waves with crossing, which give rise to non-Rayleigh statistics.

In the following we illustrate that deviations from this Rayleigh law are found. Similarly to the discussion of weak localization and coherent backscattering deviations are expected in the case of crossed paths. To this end we consider the scattering path depicted in Fig. 5.29, where the paths to the left of the crossing are labelled (k, j) and to the right of the crossing (K, J). Taking these paths into account the amplitude results in: $\Psi = \Psi_{kK} + \Psi_{kJ} + \Psi_{jK} + \Psi_{jJ}$. Now we concentrate on the second moment of the intensity which involves terms of the following form $\overline{\Psi_{kK}\Psi^*_{kJ}\Psi_{jK}\Psi^*_{jJ}} \propto \overline{\Psi e^{i\Delta\phi}}$ with the corresponding phase difference $\Delta\phi = (\phi_k + \phi_K) - (\phi_k + \phi_J) - (\phi_j + \phi_K) + (\phi_j + \phi_J) = 0$. This shows that the second moment is enhanced by:

$$\overline{I^2} = 2\overline{I}^2 \; + \; 2\gamma\overline{I}^2 \; , \tag{5.44}$$

where γ is the probability for the crossing. The same arguments can be generalized to higher moments which yields [117]:

$$\begin{aligned} \overline{I^n} &= n!\,\overline{I}^n + 2\gamma \; \tbinom{n}{2}^2 \; (n-2)!\,\overline{I}^n & (5.45) \\ &\approx n! \; \left[1 + \frac{\gamma}{2}(n^2 - n)\right] \overline{I}^n \; . & (5.46) \end{aligned}$$

The last approximation is valid for a small probability γ for the occurrence of an intersection. Finally we can convert the approximation for the moments in Eq. 5.46 into a probability distribution with the help of Eq. 5.42. The probability distribution for the intensity of the wave function reads [117]:

$$P(I) = \frac{1}{\overline{I}} \; e^{-I/\overline{I}} \; \left[1 + \gamma\left(1 - 2\frac{I}{\overline{I}} + \frac{I^2}{2\overline{I}^2}\right)\right] \; . \tag{5.47}$$

Now we compare this last result with our numerical calculation of the wave function. We have chosen the following parameters for the simulation: A Gauss correlated disorder potential with a potential height of $V_0 = 0.4\mu$ and a correlation length of $k\sigma = 1.0$.

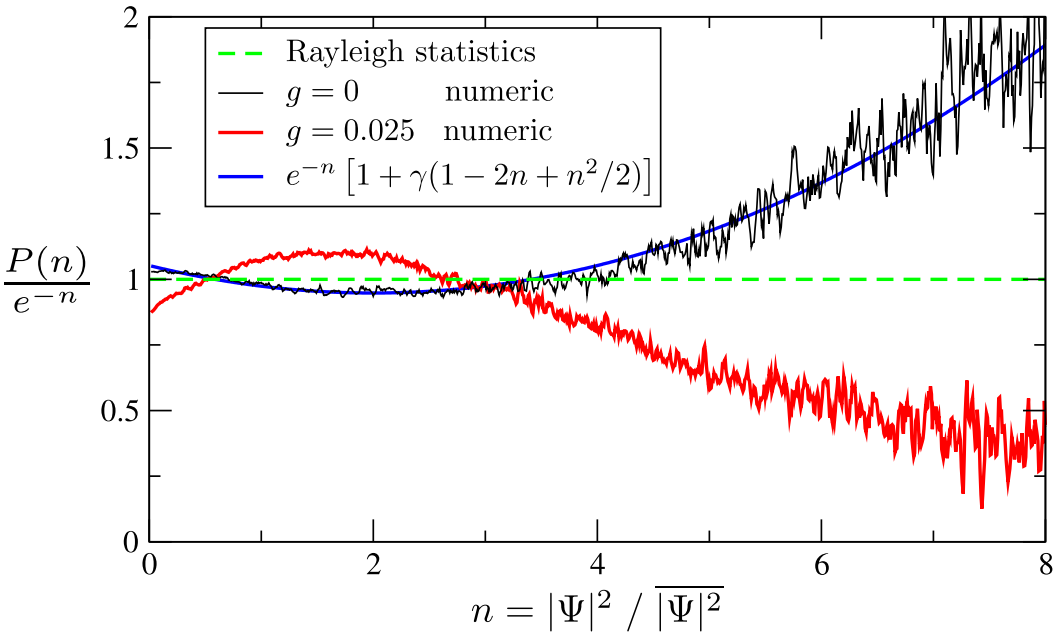

Figure 5.30: Probability distribution for the intensity of the wave function in the disorder potential. The dashed line shows the Rayleigh distribution e^{-n} with $n = |\Psi|^2/\overline{|\Psi|^2}$. We observe non-Rayleigh statistics in the linear regime (black curve), as predicted by theory [117]. The blue line shows a fit of the diagrammatic prediction to our numerical result with $\gamma = 0.053$. In the nonlinear case (red curve), with $g = 0.025$, where destructive interference in the coherent backscattering signal is observed, the curvature is reverted. Parameters: $kL = 40$, $kW = 120$, $j_{in} = \hbar k^3/m$, $k = \sqrt{2m\mu}/\hbar$, Gauss correlated disorder potential with $k\sigma = 1.0$ and $V_0 = 0.4\mu$, $g(x)$ as shown in Fig. 5.7. The statistical curve is extracted at a position $kx = 15$, resulting in a small contribution of the coherent mode.

This results in anisotropic scattering and we extract the mean free path following the methods from Chapt. 4, to $k\ell_s = 9.6$ for the scattering mean free path and $k\ell_{tr} = 13.4$ for the transport mean free path. We have chosen a length of $kL = 40$, a current of $j_{in} = \hbar k^3/m$, and in the nonlinear case a functional dependence of the nonlinearity as shown in Fig. 5.7. Finally we analyze the probability distribution at the position $kx = 15$ away from the left boundary. This is far enough inside the medium to neglect the coherent mode, which has also been disregarded in the diagrammatic derivation above. We need a large disorder average of $\sim 10^3$ disorder realizations for the numerically extracted probability distribution to be smooth. Additionally we have used all intensities along the y-direction at the fixed position $kx = 15$ to increase statistics. The result is shown in Fig. 5.30. The black line corresponds to the numerical results in the linear case. The dashed line is the Rayleigh distribution, and we see clear deviations. The blue line is a fit of the diagrammatic prediction (Eq. 5.47) to our numerical results,

and we see very good agreement. For the probability for crossing we extract a value of $\gamma = 0.053$. We believe that γ is related to the transport mean free path in the way $\gamma = \frac{2}{\pi k \ell_{tr}} \ln \frac{L}{\ell_{tr}}$, which is the same weak localization correction as given in Eq. 4.63, and leads to a transport mean free path of $k\ell_{tr} = 13.2$, which is in very good agreement with the extracted value of $k\ell_{tr} = 13.4$ with the method from Chapt. 4. Nevertheless this is still work in progress and is not confirmed yet.

However, this shows that this approach can result in an alternative way to extract the transport mean free path. Especially it would allow to investigate the dependence of the transport mean free path on the position. A transport property is extracted in this way from a local measurement.

Finally we consider the nonlinear case. In analogy to the linear case we have extracted the probability distribution for the nonlinear Gross-Pitaevskii equation. We have considered a nonlinearity strength of $g = 0.025$, which corresponds to destructive interference in the coherent backscattering signal. And indeed we observe clear deviation also in the probability distribution of the intensity for the wave function (red curve in Fig. 5.30). In addition it shows the same signatures as the nonlinear coherent backscattering effect. The curve changes from a positive curvature to a negative one.

Another starting point for the interpretation is to realize that in the case of repulsive interaction peak structures are broadened due to the interaction energy, especially high intensity peaks are affected stronger. This implies that repulsive interaction reduces the peak height and therefore the probability to observe high intensity values is lower as found in Fig. 5.30. Up to now we do not have a good understanding of this effect, calling for possible further investigations.

CHAPTER 6

Summary and perspectives

The aim of this work was to explore the field of coherent backscattering and transport in disorder potentials with matter waves, in particular with Bose-Einstein condensates. With this work we joined the theoretical research activities which were attracted as well as the experimental research by the incentive to realize Anderson localization with Bose-Einstein condensates, which was finally achieved in 2008 [29, 30]. The interests of these research activities were mainly focused on the properties of effectively one-dimensional systems. However, new effects arise in two or three spatial dimensions due to the scenario of weak localization. Consequently, we investigated two-dimensional systems with correlated disorder: On the one hand we studied transport properties which are characterized by the scattering- and transport mean free path, and on the other hand we opened the field to study coherent backscattering with matter waves in particular with a focus on the effects arising from atom-atom interaction. Furthermore we developed numerical methods to calculate time-dependent nonlinear scattering.

This work is based on the mean-field dynamics of the Bose-Einstein condensate described by the nonlinear Gross-Pitaevskii equation, which has already been successfully applied to many experimental situations. Therefore we gave a derivation of the Gross-Pitaevskii equation which describes the time-dependent macroscopic wave function of the condensate at the beginning of this work:
We started from the many body Hamiltonian for the atoms and then derived a formulation of the dynamics for a system which is confined to two dimensions by a transverse potential. Consecutively, we studied the experimental relevant case of potentials in the plane which change adiabatically in space, which allows to consider the ground state in transverse direction. We explained possibilities to create such potentials for the atoms, either with optical or with magnetic methods.

After preparing the fundamentals, we were confronted with the task to develop a numerical apparatus to describe the dynamics of scattering states within the nonlinear wave equation for two-dimensional geometries. In order to study open scattering systems we mimicked the reservoir by an inhomogeneous source term in the Gross-Pitaevskii equation. In the context of infinitely extended scattering states absorbing boundaries are of essential importance, because the numerical approach is limited to a finite region in space. To this end we designed boundary conditions which are capable to absorb two-dimensional waves. These new methods can be applied to a wide range of scattering potentials including time-dependent potentials.

We applied those methods to calculate the intensity pattern through a double slit and a multi slit geometry, where the results demonstrate the accuracy and possibilities of our numerical technique. Furthermore we studied an effectively one-dimensional double barrier potential, which can also be seen as a Fabry-Perot interferometer. We showed the relation between scattering states and quasi bound states. To this end we derived the transmission through the double barrier potential near a well-separated resonance only from the properties of the corresponding quasi bound state in the double barrier potential. We especially showed that the tilting of the Breit-Wigner resonance is due to the energy shift arising from the interaction energy of the quasi bound state.

Furthermore we addressed the problem of transport in two-dimensional disorder potentials for the linear Schrödinger equation. The relevant case for experiments are correlated disorder potentials, which we studied in detail. We considered on the one hand a disorder potential with a Gaussian correlation function and Gaussian statistics and on the other hand a speckle potential which is utilized in most experiments with disorder. We presented a diagrammatic theory which allows to calculate the scattering mean free path and the transport mean free path [84], the latter one in the diffusion approximation as well as with weak localization corrections, which arise due to the constructive interference of time reversed scattering paths.
In the case of the Gauss correlated disorder potential we presented analytical expressions for the scattering and transport mean free path within the Born approximation. For small correlation lengths of the Gauss correlated disorder potential we found good agreement in the scattering and the transport mean free path for weak scattering. In particular we observed the weak localization corrections. Nevertheless we discovered deviations in the scattering mean free path for stronger scattering and larger correlation lengths. These deviations can be attributed to the Born approximation since the self-consistent Born approximation shows already improved agreement with our numerical results. These deviations are of importance especially in the regime of strong localization, because the localization length is strongly affected by the scattering mean free path.
In the case of a speckle disorder potential we observed quite large deviations in the scattering and the transport mean free path between our numerical results and the

diagrammatic approach in the Born approximation. We expect that the Born approximation for the Gaussian disorder potential leads to better results compared to the speckle potential, since the next to leading order vanishes for the Gaussian case but not for the speckle potential. We restricted the discussion above to the linear case, since the atom-atom interaction modifies the scattering mean free path and transport mean free path only negligible. This is in comparison to the influences of the nonlinearity in the coherent backscattering scenario.

We finally studied coherent backscattering which arises due to constructive interference between time reversed scattering paths in great detail. We explained that this interference arises only in exactly backward direction of the incident current and consequently presented known results like the shape of the coherent backscattering peak, which were originally derived in the context of optics. Then we showed the applicability of coherent backscattering to Bose-Einstein condensates. Our main focus was to describe the influence of the atom-atom interaction onto the scenario of coherent backscattering. There we found the new phenomena that the coherent backscattering peak reverts to a dip in the angular resolved current, which implies a change from constructive to destructive interference between scattering paths. This occurs already at a quite small strength of the nonlinearity which corresponds to an interaction energy of $\sim 10^{-2}$ from the kinetic energy. We compared our numerical results for a Gauss correlated disorder potential with a diagrammatic theory developed just recently [59], where we gave a sketch of the principle ideas and derived an expression which accounts for the reduction of the coherent backscattering peak. We found good quantitative agreement between the diagrammatic theory and our numerical results. The small deviations there we could relate to current, respectively energy conservation, which is not fulfilled in the diagrammatic approach.
In addition we found that the coherent mode and the density distribution, which determines the scattering and transport mean free path, is only negligibly modified as predicted by diagrammatic theory. Furthermore, we investigated the experimental relevant situation, where the Bose-Einstein condensate is coupled via an adiabatic variation of the transverse confinement into the two-dimensional waveguide. This changes quantitatively the backscattered current and the necessary interaction strength to observe the destructive interference, but the qualitative behavior remains. We checked that the inversion of the coherent backscattering peak from constructive to destructive interference is also observed in the case of a disorder potential with longer correlation length, and particularly in the case of the experimental relevant case of a speckle disorder potential. The interpretation of the dip structure arising from coherent backscattering is confirmed by a simulation where the incident current enters with an angle, where the dip appears in exactly backward direction, in contrast to reflection, which we observe for stronger atom-atom interaction. In this regime the time-dependent integration of the Gross-Pitaevskii equation leads to a intrinsically time-dependent behavior.

Finally we started to investigate the statistical properties of the intensity, which show a Rayleigh distribution in first approximation. In the linear case the deviations from this Rayleigh distribution are explained due to weak localization effects arising from the interference of transmitted scattering paths with intersection. Those predictions are in good agreement with our numerical results. In the nonlinear case we find significant deviations, where the interpretation is still open. This question opens an interesting field to analyze the statistical properties of the scattering wave functions in particular in the presence of interaction, since we have already shown that modifications can be observed.

Our approach allows for a detailed study of the transport phenomena in two-dimensional systems, but since it is based on the Gross-Pitaevskii equation we are restricted to the mean-field regime. This implies that the interaction with the thermal cloud around the condensate and the depletion of the condensate is neglected, and consequently we are limited to temperatures of the Bose-Einstein condensate much lower than the critical condensation temperature. Additionally, excitations from the condensate can arise in the nonlinear regime where intrinsic time-dependent behavior occurs. These effects can be investigated with a cumulant approach introduced by T. Köhler and K. Burnett [116], which allows the corrections to the mean-field in the case of a finite number of atoms to be calculated in a systematic way. This has been investigated only in one-dimensional systems [115, 122].

Furthermore we hope that our work initiates experimental research on coherent backscattering within the nonlinear regime. Especially the group of G. Labeyrie and R. Kaiser in Nice is already working on the experimental realization of coherent backscattering with matter waves. From a theoretical perspective interesting effects may also be expected towards the regime of strong localization. We already started to explore Anderson localization for the linear system with the emphasis to understand finite size effects due to the limited spatial size of the condensate. The nonlinear case is still open and new effects may be discovered. We consider our approach as a good starting point for further theoretical research activities. For example it can be applied to the transport through two-dimensional billiard geometries, where the disorder is replaced by a billiard geometry, which displays chaotic dynamics in the classical regime.

In conclusion we have presented the transport of Bose-Einstein condensates in disorder potentials. We evaluated the scattering and transport mean free path for correlated disorder potentials numerically. Furthermore, we introduced the phenomenon of coherent backscattering to coherent matter waves and found a substantial modification in the interference effect. Our numerical results are in good agreement with the diagrammatic approach to nonlinear coherent backscattering. Finally we would appreciate if our theoretical predictions are confirmed by experimental investigation, and if our work inspires further research activities.

APPENDIX A

Equations for diagrammatic CBS

In chapter 5 we compared our numerical results to the diagrammatic theory for nonlinear coherent backscattering developed by T. Wellens and B. Grémaud [59, 112]. The theory was originally designed for nonlinear scattering events, but it applies as well to a nonlinear scattering medium. Here we give for reference the full set of equations for the calculation of the coherent backscattering peak as derived by T. Wellens.

The following equations are valid only for isotropic scattering with scattering mean free path $\ell = \ell_s = \ell_B$ and an arbitrary shape of the disorder region, especially $\frac{1}{\ell} = 0$ outside the disorder region. Furthermore they are valid for an arbitrary nonlinearity region with $\alpha(\mathbf{r}) = 2m|\psi_0|^2 g(\mathbf{r})/(\hbar k)^2$. The linear equations for the average intensity $I(\mathbf{r}) = \langle|\psi(\mathbf{r})|^2\rangle/|\psi_0|^2$ and ladder current density j_d in backward direction are given by:

$$I(\mathbf{r}) = e^{-\int_0^\infty dt/\ell(\mathbf{r}-t\mathbf{e_L})} + \int d\mathbf{r}' P(\mathbf{r},\mathbf{r}') \frac{I(\mathbf{r}')}{\ell(\mathbf{r}')} \qquad \text{and} \tag{A.1}$$

$$j_d = \int \frac{d\mathbf{r}}{A} I_c(\mathbf{r}) \frac{I(\mathbf{r})}{\ell(\mathbf{r})} \,, \tag{A.2}$$

where $\mathbf{e_L}$ is a unit vector parallel to the incident wave, A is the transverse width of the disorder sample, and $P(\mathbf{r},\mathbf{r}')$ is determined by:

$$P(\mathbf{r},\mathbf{r}') = \frac{e^{-|\mathbf{r}-\mathbf{r}'|\int_0^1 dt/\ell(\mathbf{r}-t\mathbf{r}+t\mathbf{r}')}}{2\pi|\mathbf{r}-\mathbf{r}'|} \,. \tag{A.3}$$

For the crossed intensity the following transport equations are obtained:

$$C_c(\mathbf{r}) = e^{ik\int_0^\infty dt n_c(\mathbf{r}-t\mathbf{e_L})}\Big(e^{-ik\int_0^\infty dt n^*(\mathbf{r}-t\mathbf{e_L})} \tag{A.4}$$
$$-ik\int_0^\infty ds\alpha^*(\mathbf{r}-s\mathbf{e_L})e^{-ik\int_0^s dt n^*(\mathbf{r}-t\mathbf{e_L})-ik\int_s^\infty dt n_c^*(\mathbf{r}-t\mathbf{e_L})}C_1(\mathbf{r}-s\mathbf{e_L})\Big)$$

$$C_1(\mathbf{r}) = \int d\mathbf{r}' P(\mathbf{r},\mathbf{r}')\Big(C_1(\mathbf{r}')+C_c(\mathbf{r}')\Big)\left(\frac{1}{\ell(\mathbf{r}')}-ik\alpha^*(\mathbf{r}')\hat{I}(\mathbf{r}',\mathbf{e}_{\mathbf{r}'-\mathbf{r}})\right) \tag{A.5}$$

$$C_2(\mathbf{r}) = C_p(\mathbf{r})+\int d\mathbf{r}'\frac{P(\mathbf{r},\mathbf{r}')}{\ell(\mathbf{r})}C_2(\mathbf{r}')+ik\alpha(\mathbf{r})e^{ik\int_0^\infty dt(n_c-n)(\mathbf{r}-t\mathbf{e_L})}\times$$
$$\times\int_0^\infty ds\left(C_o(\mathbf{r}+s\mathbf{e_L})+e^{-\int_{-s}^\infty dt/\ell(\mathbf{r}-t\mathbf{e_L})}\frac{I(\mathbf{r}+s\mathbf{e_L})}{\ell(\mathbf{r}+s\mathbf{e_L})}\right) \tag{A.6}$$

$$C_p(\mathbf{r}) = ik\alpha(\mathbf{r})\int d\mathbf{r}' P(\mathbf{r},\mathbf{r}')\Bigg[C_2(\mathbf{r}')+$$
$$+\Big(C_1(\mathbf{r}')+C_c(\mathbf{r}')\Big)\left(\frac{1}{\ell(\mathbf{r}')}-ik\alpha^*(\mathbf{r}')\hat{I}(\mathbf{r}',\mathbf{e}_{\mathbf{r}'-\mathbf{r}})\right)\Bigg]\hat{I}(\mathbf{r},\mathbf{e}_{\mathbf{r}-\mathbf{r}'}) \tag{A.7}$$

$$C_o(\mathbf{r}) = e^{ik\int_0^\infty dt(n-n_c^*)(\mathbf{r}-t\mathbf{e_L})}\left(\frac{C_1(\mathbf{r})}{\ell(\mathbf{r})}+C_p(\mathbf{r})+\int d\mathbf{r}'\frac{P(\mathbf{r},\mathbf{r}')}{\ell(\mathbf{r})}C_2(\mathbf{r}')\right)$$
$$-ike^{-\int_0^\infty dt/\ell(\mathbf{r}-t\mathbf{e_L})}\frac{I(\mathbf{r})}{\ell(\mathbf{r})}\int_0^\infty ds e^{ik\int_s^\infty dt(n^*-n_c^*)(\mathbf{r}-t\mathbf{e_L})}\times$$
$$\times\alpha^*(\mathbf{r}-s\mathbf{e_L})C_1(\mathbf{r}-s\mathbf{e_L})\,, \tag{A.8}$$

where $\mathbf{e}_{\mathbf{r}-\mathbf{r}'}$ is a unit vector given by $\mathbf{e}_{\mathbf{r}-\mathbf{r}'}=(\mathbf{r}-\mathbf{r}')/|\mathbf{r}-\mathbf{r}'|$. Additionally the following definitions have been used:

$$n(\mathbf{r}) = 1+\frac{i}{2k\ell(\mathbf{r})}+\alpha(\mathbf{r})I(\mathbf{r}) \tag{A.9}$$

$$n_c(\mathbf{r}) = n(\mathbf{r})-\alpha(\mathbf{r})\frac{e^{-\int_0^\infty ds/\ell(\mathbf{r}-s\mathbf{e_L})}}{2} \tag{A.10}$$

$$\hat{I}(\mathbf{r},\mathbf{e}) = \int_0^\infty d\rho e^{-\int_0^\rho ds/\ell(\mathbf{r}+s\mathbf{e})}\frac{I(\mathbf{r}+\rho\mathbf{e})}{\ell(\mathbf{r}+\rho\mathbf{e})} \tag{A.11}$$

Finally the current in backward direction arising from the nonlinear Cooperon is obtained:

$$j_c=\int\frac{d\mathbf{r}}{A}C_o(\mathbf{r})\,. \tag{A.12}$$

The total current j is the sum of the ladder and the cooperon contribution $j=j_d+j_c$, and the above transport equations were solved numerically.

Bibliography

[1] S. Bose, *Plancks Gesetz und Lichtquantenhypothese*, *Zeitschrift für Physik A Hadrons and Nuclei* **26**, 178–181 (1924).

[2] A. Einstein, *Quantentheorie des einatomigen idealen Gases: Zweite Abhandlung"*, *Sitzungsberichte der Preussischen Akademie der Wissenschaften* **1**, 3 (1925).

[3] A. Einstein, *Quantentheorie des einatomigen idealen Gases*, *Sitzungsberichte der Preussischen Akademie der Wissenschaften* **22**, 261 (1924).

[4] W. D. Phillips, *Nobel Lecture: Laser cooling and trapping of neutral atoms*, *Rev. Mod. Phys.* **70**, 721–741 (1998).

[5] W. Ketterle and N. V. Druten, *Evaporative Cooling of Trapped Atoms*, vol. 37 of *Advances In Atomic, Molecular, and Optical Physics*, pp. 181 – 236. Academic Press, 1996.

[6] K. B. Davis, M. O. Mewes, M. R. Andrews, N. J. van Druten, D. S. Durfee, D. M. Kurn, and W. Ketterle, *Bose-Einstein Condensation in a Gas of Sodium Atoms*, *Phys. Rev. Lett.* **75**, 3969–3973 (1995).

[7] M. H. Anderson, J. R. Ensher, M. R. Matthews, C. E. Wieman, and E. A. Cornell, *Observation of Bose-Einstein Condensation in a Dilute Atomic Vapor*, *Science* **269**, 198–201 (1995).

[8] C. C. Bradley, C. A. Sackett, J. J. Tollett, and R. G. Hulet, *Evidence of Bose-Einstein Condensation in an Atomic Gas with Attractive Interactions*, *Phys. Rev. Lett.* **75**, 1687–1690 (1995).

[9] M. Lewenstein, A. Sanpera, V. Ahufinger, B. Damski, A. Sen, and U. Sen, *Ultracold atomic gases in optical lattices: mimicking condensed matter physics and beyond*, *Advances in Physics* **56**, 243–379 (2007).

[10] M. Greiner, O. Mandel, T. Esslinger, T. W. Hansch, and I. Bloch, *Quantum phase transition from a superfluid to a Mott insulator in a gas of ultracold atoms*, *Nature* **415**, 39–44 (2002).

[11] M. Greiner, C. A. Regal, and D. S. Jin, *Emergence of a molecular Bose-Einstein condensate from a Fermi gas*, *Nature* **426**, 537–540 (2003).

[12] C. A. Regal, C. Ticknor, J. L. Bohn, and D. S. Jin, *Creation of ultracold molecules from a Fermi gas of atoms*, *Nature* **424**, 47–50 (2003).

[13] T. Bourdel, L. Khaykovich, J. Cubizolles, J. Zhang, F. Chevy, M. Teichmann, L. Tarruell, S. J. J. M. F. Kokkelmans, and C. Salomon, *Experimental Study of the BEC-BCS Crossover Region in Lithium 6*, *Phys. Rev. Lett.* **93**, 050401 (2004).

[14] S. Inouye, M. R. Andrews, J. Stenger, H.-J. Miesner, D. M. Stamper-Kurn, and W. Ketterle, *Observation of Feshbach resonances in a Bose-Einstein condensate*, *Nature* **392**, 151–154 (1998).

[15] W. Guerin, J.-F. Riou, J. P. Gaebler, V. Josse, P. Bouyer, and A. Aspect, *Guided Quasicontinuous Atom Laser*, *Phys. Rev. Lett.* **97**, 200402 (2006).

[16] J. McKeever, A. Boca, A. D. Boozer, J. R. Buck, and H. J. Kimble, *Experimental realization of a one-atom laser in the regime of strong coupling*, *Nature* **425**, 268–271 (2003).

[17] I. Bloch, T. W. Hänsch, and T. Esslinger, *Atom Laser with a cw Output Coupler*, *Phys. Rev. Lett.* **82**, 3008–3011 (1999).

[18] W. Hänsel, P. Hommelhoff, T. W. Hänsch, and J. Reichel, *Bose-Einstein condensation on a microelectronic chip*, *Nature* **413**, 498–501 (2001).

[19] T. Paul, P. Leboeuf, N. Pavloff, K. Richter, and P. Schlagheck, *Nonlinear transport of Bose-Einstein condensates through waveguides with disorder*, *Phys. Rev. A* **72**, 063621 (2005).

[20] T. Paul, P. Schlagheck, P. Leboeuf, and N. Pavloff, *Superfluidity versus Anderson Localization in a Dilute Bose Gas*, *Phys. Rev. Lett.* **98**, 210602 (2007).

[21] J. Fortágh, H. Ott, S. Kraft, A. Günther, and C. Zimmermann, *Surface effects in magnetic microtraps*, *Phys. Rev. A* **66**, 041604 (2002).

[22] T. Schumm, J. Estève, C. Figl, J.-B. Trebbia, C. Aussibal, H. Nguyen, D. Mailly, I. Bouchoule, C.I. Westbrook, and A. Aspect, *Atom chips in the real world: the effects of wire corrugation*, *The European Physical Journal D* **32**, 171–180 (2005).

[23] J. Estève, C. Aussibal, T. S. und C. Figl, D. Mailly, I. Bouchoule, C. I. Westbrook, , and A. Aspect, *Role of wire imperfections in micromagnetic traps for atoms*, *Phys. Rev. A* **70**, 043629 (2004).

[24] P. W. Anderson, *Absence of diffusion in certain random lattices*, *Phys. Rev.* **109**, 1492–1505 (1958).

[25] B. Kramer and A. MacKinnon, *Localization: theory and experiment*, *Rep. Prog. Phys.* **56**, 1469–1564 (1993).

[26] T. Schulte, S. Drenkelforth, J. Kruse, W. Ertmer, J. Arlt, K. Sacha, J. Zakrzewski, and M. Lewenstein, *Routes Towards Anderson-Like Localization of Bose-Einstein Condensates in Disordered Optical Lattices*, *Phys. Rev. Lett.* **95**, 170411 (2005).

[27] C. Fort, L. Fallani, V. Guarrera, J. E. Lye, M. Modugno, D. S. Wiersma, and M. Inguscio, *Effect of Optical Disorder and Single Defects on the Expansion of a Bose-Einstein Condensate in a One-Dimensional Waveguide*, *Phys. Rev. Lett.* **95**, 170410 (2005).

[28] D. Clément, A. F. Varón, M. Hugbart, J. A. Retter, P. Bouyer, L. Sanchez-Palencia, D. M. Gangardt, G. V. Shlyapnikov, and A. Aspect, *Suppression of Transport of an Interacting Elongated Bose-Einstein Condensate in a Random Potential*, *Phys. Rev. Lett.* **95**, 170409 (2005).

[29] J. Billy, V. Josse, Z. Zuo, A. Bernard, B. Hambrecht, P. Lugan, D. Clement, L. Sanchez-Palencia, P. Bouyer, and A. Aspect, *Direct observation of Anderson localization of matter waves in a controlled disorder*, *Nature* **453**, 891–894 (2008).

[30] G. Roati, C. D'Errico, L. Fallani, M. Fattori, C. Fort, M. Zaccanti, G. Modugno, M. Modugno, and M. Inguscio, *Anderson localization of a non-interacting Bose-Einstein condensate*, *Nature* **453**, 895–898 (2008).

[31] J. E. Lye, L. Fallani, M. Modugno, D. S. Wiersma, C. Fort, and M. Inguscio, *Bose-Einstein Condensate in a Random Potential*, *Phys. Rev. Lett.* **95**, 070401 (2005).

[32] L. Sanchez-Palencia, D. Clément, P. Lugan, P. Bouyer, G. V. Shlyapnikov, and A. Aspect, *Anderson Localization of Expanding Bose-Einstein Condensates in Random Potentials*, *Phys. Rev. Lett.* **98**, 210401 (2007).

[33] P. Lugan, D. Clément, P. Bouyer, A. Aspect, and L. Sanchez-Palencia, *Anderson Localization of Bogolyubov Quasiparticles in Interacting Bose-Einstein Condensates*, *Phys. Rev. Lett.* **99**, 180402 (2007).

[34] N. Bilas and N. Pavloff, *Anderson localization of elementary excitations in a one-dimensional Bose-Einstein condensate*, *Eur. Phys. J. D* **40**, 387–397 (2006).

[35] Y. P. Chen, J. Hitchcock, D. Dries, M. Junker, C. Welford, and R. G. Hulet, *Phase coherence and superfluid-insulator transition in a disordered Bose-Einstein condensate*, *Phys. Rev. A* **77**, 033632 (2008).

[36] J. E. Lye, L. Fallani, C. Fort, V. Guarrera, M. Modugno, D. S. Wiersma, and M. Inguscio, *Effect of interactions on the localization of a Bose-Einstein condensate in a quasiperiodic lattice*, *Phys. Rev. A* **75**, 061603 (2007).

[37] L. Fallani, J. E. Lye, V. Guarrera, C. Fort, and M. Inguscio, *Ultracold Atoms in a Disordered Crystal of Light: Towards a Bose Glass*, *Phys. Rev. Lett.* **98**, 130404 (2007).

[38] B. Damski, J. Zakrzewski, L. Santos, P. Zoller, and M. Lewenstein, *Atomic Bose and Anderson Glasses in Optical Lattices*, *Phys. Rev. Lett.* **91**, 080403 (2003).

[39] D. S. Wiersma, P. Bartolini, A. Lagendijk, and R. Righini, *Localization of light in a disordered medium*, *Nature* **390**, 671–673 (1997).

[40] F. Scheffold, R. Lenke, R. Tweer, and G. Maret, *Localization or classical diffusion of light?*, *Nature* **398**, 206–207 (1999).

[41] C. M. Aegerter, M. Störzer, S. Fiebig, W. Bührer, and G. Maret, *Observation of Anderson localization of light in three dimensions*, *J. Opt. Soc. Am. A* **24**, A23–A27 (2007).

[42] M. Störzer, P. Gross, C. M. Aegerter, and G. Maret, *Observation of the Critical Regime Near Anderson Localization of Light*, *Phys. Rev. Lett.* **96**, 063904 (2006).

[43] C. Aegerter and G. Maret, *Coherent Backscattering and Anderson Localization of Light.*, *Progress in Optics Letters* **52**, (2009).

[44] M. P. van Albada and A. Lagendijk, *Observation of Weak Localization of Light in a Random Medium*, *Phys. Rev. Lett.* **55**, 2692–2695 (1985).

[45] P.-E. Wolf and G. Maret, *Weak Localization and Coherent Backscattering of Photons in Disordered Media*, *Phys. Rev. Lett.* **55**, 2696–2699 (1985).

[46] D. S. Wiersma, M. P. van Albada, B. A. van Tiggelen, and A. Lagendijk, *Experimental Evidence for Recurrent Multiple Scattering Events of Light in Disordered Media*, *Phys. Rev. Lett.* **74**, 4193–4196 (1995).

[47] G. Muller, *Seelinger analyzed observations*, *Pub. Obs. Potsdam* **8**, 193 (1893).

[48] B. W. Hapke, R. M. Nelson, and W. D. Smythe, *The Opposition Effect of the Moon: The Contribution of Coherent Backscatter*, *Science* **260**, 509–511 (1993).

[49] B. Hapke and D. Blewett, *Coherent backscatter model for the unusual radar reflectivity of icy satellites*, *Nature* **352**, 46–47 (1991).

[50] A. Tourin, A. Derode, P. Roux, B. A. van Tiggelen, and M. Fink, *Time-Dependent Coherent Backscattering of Acoustic Waves*, *Phys. Rev. Lett.* **79**, 3637–3639 (1997).

[51] M. Fink, D. Cassereau, A. Derode, C. Prada, P. Roux, M. Tanter, J.-L. Thomas, and F. Wu, *Time-reversed acoustics*, *Rep. Prog. Phys.* **63**, 1933–1995 (2000).

[52] G. Labeyrie, D. Delande, R. Kaiser, and C. Miniatura, *Light Transport in Cold Atoms and Thermal Decoherence*, *Phys. Rev. Lett.* **97**, 013004 (2006).

[53] G. Labeyrie, F. de Tomasi, J.-C. Bernard, C. A. Müller, C. Miniatura, and R. Kaiser, *Coherent Backscattering of Light by Cold Atoms*, *Phys. Rev. Lett.* **83**, 5266–5269 (1999).

[54] G. Labeyrie, D. Delande, C. A. Müller, C. Miniatura, and R. Kaiser, *Coherent backscattering of light by cold atoms: Theory meets experiment*, *EPL* **61**, 327–333 (2003).

[55] T. Jonckheere, C. A. Müller, R. Kaiser, C. Miniatura, and D. Delande, *Multiple Scattering of Light by Atoms in the Weak Localization Regime*, *Phys. Rev. Lett.* **85**, 4269–4272 (2000).

[56] T. Wellens, B. Grémaud, D. Delande, and C. Miniatura, *Coherent backscattering of light with nonlinear atomic scatterers*, *Phys. Rev. A* **73**, 013802 (2006).

[57] T. Chanelière, D. Wilkowski, Y. Bidel, R. Kaiser, and C. Miniatura, *Saturation-induced coherence loss in coherent backscattering of light*, *Phys. Rev. E* **70**, 036602 (2004).

[58] V. Shatokhin, C. A. Müller, and A. Buchleitner, *Coherent Inelastic Backscattering of Intense Laser Light by Cold Atoms*, *Physical Review Letters* **94**, 043603 (2005).

[59] T. Wellens and B. Grémaud, *Nonlinear Coherent Transport of Waves in Disordered Media*, *Phys. Rev. Lett.* **100**, 033902 (2008).

[60] F. Dalfovo, S. Giorgini, L. P. Pitaevskii, and S. Stringari, *Theory of Bose-Einstein condensation in trapped gases*, *Rev. Mod. Phys.* **71**, 463–512 (1999).

[61] C. J. Pethick and H. Smith, *Bose-Einstein Condensation in Dilute Gases*. Cambridge University Press, 2002.

[62] L. Pitaevskii and S. Stringari, *Bose-Einstein Condensation*. Oxford University Press, Oxford, 2003.

[63] Y. Castin and R. Dum, *Low-temperature Bose-Einstein condensates in time-dependent traps: Beyond the $U(1)$ symmetry-breaking approach*, *Phys. Rev. A* **57**, 3008–3021 (1998).

[64] P. Leboeuf and N. Pavloff, *Bose-Einstein beams: Coherent propagation through a guide*, *Phys. Rev. A* **64**, 033602 (2001).

[65] T. Paul, *Transport von Bose-Einstein Kondensaten in mesoskopischen Strukturen*. PhD thesis, Universität Regensburg, 2006.

[66] V. Milner, J. L. Hanssen, W. C. Campbell, and M. G. Raizen, *Optical Billiards for Atoms*, *Phys. Rev. Lett.* **86**, 1514–1517 (2001).

[67] F. Schwabl, *Quantenmechanik QM 1*. Springer New York, 2007.

[68] W. H. Wing, *On neutral particle trapping in quasistatic electromagnetic fields*, *Progress in Quantum Electronics* **8**, 181 – 199 (1984).

[69] T. Paul, K. Richter, and P. Schlagheck, *Nonlinear Resonant Transport of Bose-Einstein Condensates*, *Phys. Rev. Lett.* **94**, 020404 (2005).

[70] W. Press, S. Teukolsky, W. Vetterling, and B. Flannery, *Numerical Recipes in C++: The Art of Scientific Computing Second Edition*. Cambridge University Press, New York, 2002.

[71] W. A. Ames, *Numerical Methods for Partial Differential Equations*. Academic Press, New York, 1977.

[72] T. Shibata, *Absorbing boundary conditions for the finite-difference time-domain calculation of the one-dimensional Schrödinger equation*, *Phys. Rev. B* **43**, 6760–6763 (1991).

[73] T. Paul, M. Hartung, K. Richter, and P. Schlagheck, *Nonlinear transport of Bose-Einstein condensates through mesoscopic waveguides*, *Phys. Rev. A* **76**, 063605 (2007).

[74] S. A. Gredeskul and Y. S. Kivshar, *Propagation and scattering of nonlinear waves in disordered systems*, *Phys. Rep.* **216**, 1–61 (1992).

[75] P. S. Sandro Wimberger and R. Mannella, *Tunnelling rates for the nonlinear Wannier-Stark problem*, *J. Phys. B* **39**, 729–740 (2006).

[76] P. Schlagheck and S. Wimberger, *Nonexponential decay of Bose-Einstein condensates: a numerical study based on the complex scaling method*, *Appl. Phys. B: Lasers Opt.* **86**, 385–390 (2007).

[77] L. D. Carr, M. J. Holland, and B. A. Malomed, *Macroscopic quantum tunnelling of Bose-Einstein condensates in a finite potential well*, *J. Phys. B* **38**, 3217–3231 (2005).

[78] P. Schlagheck and T. Paul, *Complex-scaling approach to the decay of Bose-Einstein condensates*, *Phys. Rev. A* **73**, 023619 (2006).

[79] J. W. Goodman, *Laser Speckle and Related Phenomena*, ch. Statistical properties of laser speckle patterns, p. 9. Springer-Verlag, 1975.

[80] R. Kuhn, *Coherent Transport of Matter Waves in Disordered Optical Potentials*. PhD thesis, Universität Bayreuth, 2007.

[81] R. C. Kuhn, C. Miniatura, D. Delande, O. Sigwarth, and C. A. Müller, *Localization of Matter Waves in Two-Dimensional Disordered Optical Potentials*, *Phys. Rev. Lett.* **95**, 250403 (2005).

[82] P. Horak, J.-Y. Courtois, and G. Grynberg, *Atom cooling and trapping by disorder*, *Phys. Rev. A* **58**, 3953–3962 (1998).

[83] J. M. Huntley, *Speckle photography fringe analysis: assessment of current algorithms*, *Appl. Opt.* **28**, 4316 (1989).

[84] R. C. Kuhn, O. Sigwarth, C. Miniatura, D. Delande, and C. A. Müller, *Coherent matter wave transport in speckle potentials*, *New J. Phys.* **9**, 161 (2007).

[85] A. Fetter and J. D. Walecka, *Quantum Theory of Many-Particle Systems.* Dover Pubn Inc, 2003.

[86] J. Rammer, *Quantum transport theory.* Westview Press, 1998.

[87] E. Akkermans and G. Montambaux, *Mesoscopic Physics of Electrons and Photons.* Cambridge University Press, 2007.

[88] E. Akkermans, G. Montambaux, J.-L. Pichard, , and J. Zinn-Justin, eds., *Mesoscopic Quantum Physics: proceedings of the Les Houches Summer School Session LXI.* Elsevier Science B. V., 1996.

[89] C. A. Müller, *private communication*, 2008.

[90] C. Gaul and P. Schlagheck, *private communication*, 2008.

[91] D. Vollhardt and P. Wölfle, *Diagrammatic, self-consistent treatment of the Anderson localization problem in $d \leq 2$ dimensions*, *Phys. Rev. B* **22**, 4666–4679 (1980).

[92] D. Vollhardt and P. Wölfle, *Electronic phase transitions*, ch. Self-consistent theory of Anderson localization, p. 1. Elsevier Science B. V., 1992.

[93] H. van de Hulst, *Multiple Light Scattering.* Academic Press, 1980.

[94] I. Freund, M. Rosenbluh, R. Berkovits, and M. Kaveh, *Coherent Backscattering of Light in a Quasi-Two-Dimensional System*, *Phys. Rev. Lett.* **61**, 1214–1217 (1988).

[95] L. P. Gor'kov, A. I. Larkin, and D. E. Khmel'nitskii, *Particle conductivity in a two-dimensional random potential*, *JETP Letters* **30**, 228–232 (1979).

[96] G. Bergmann, *Weak localization in thin films a time-of-flight experiment with conduction electrons*, *Phys. Rep.* **107**, 1–58 (1984).

[97] B. L. Altshuler, D. Khmel'nitzkii, A. I. Larkin, and P. A. Lee, *Magnetoresistance and Hall effect in a disordered two-dimensional electron gas*, *Phys. Rev. B* **22**, 5142–5153 (1980).

[98] E. Akkermans, P. E. Wolf, and R. Maynard, *Coherent Backscattering of Light by Disordered Media: Analysis of the Peak Line Shape*, *Phys. Rev. Lett.* **56**, 1471–1474 (1986).

[99] E. Akkermans and G. Montambaux, *Coherent multiple scattering in disordered media*, *arXiv* **cond-mat**, 0104013 (2001).

[100] E. Akkermans, P. Wolf, R. Maynard, and G. Maret, *Theoretical study of the coherent backscattering of light by disordered media*, *J. Phys. France* **49**, 77–98 (1988).

[101] R. Berkovits and M. Kaveh, *Weak localisation of photons in a disordered two-dimensional medium*, *Journal of Physics C: Solid State Physics* **20**, L181–L185 (1987).

[102] D. S. Wiersma, *Light in strongly scattering and amplifying random media*. PhD thesis, FOM-Institute for Atomic and Molecular Physics, Amsterdam, 1995.

[103] L. Margerin, M. Campillo, and B. A. van Tiggelen, *Coherent backscattering of acoustic waves in the near field*, *Geophysical Journal International* **145**, 593–603 (2001).

[104] P. Wolf, G. Maret, E. Akkermans, and R. Maynard, *Optical Coherent Backscattering by Random Media*, *J. Phys. France* **49**, 63 (1988).

[105] D. M. Zumbühl, J. B. Miller, C. M. Marcus, K. Campman, and A. C. Gossard, *Spin-Orbit Coupling, Antilocalization, and Parallel Magnetic Fields in Quantum Dots*, *Phys. Rev. Lett.* **89**, 276803 (2002).

[106] T. Wellens, *Diffusion and weak localization in disordered nonlinear media*, *unpublished* (2006).

[107] M. Hartung, T. Wellens, C. A. Müller, K. Richter, and P. Schlagheck, *Coherent Backscattering of Bose-Einstein Condensates in Two-Dimensional Disorder Potentials*, *Phys. Rev. Lett.* **101**, 020603 (2008).

[108] S. E. Skipetrov and R. Maynard, *Instabilities of Waves in Nonlinear Disordered Media*, *Phys. Rev. Lett.* **85**, 736–739 (2000).

[109] B. Spivak and A. Zyuzin, *Mesoscopic Sensitivity of Speckles in Disordered Nonlinear Media to Changes of the Scattering Potential*, *Phys. Rev. Lett.* **84**, 1970–1973 (2000).

[110] N. M. Lawandy, R. M. Balachandran, A. S. L. Gomes, and E. Sauvain, *Laser action in strongly scattering media*, *Nature* **368**, 436–438 (1994).

[111] T. Wellens and B. Grémaud, *Observation of coherent backscattering 'factor of three' in a numerical experiment*, *J. Phys. B* **39**, 4719–4731 (2006).

[112] T. Wellens, *BECBS - complete equations*, *private communication* (2008).

[113] S. Hikami, *Anderson localization in a nonlinear-σ-model representation*, *Phys. Rev. B* **24**, 2671–2679 (1981).

[114] S. Fiebig, C. M. Aegerter, W. Buhrer, M. Storzer, E. Akkermans, G. Montambaux, and G. Maret, *Conservation of energy in coherent backscattering of light*, *arXiv* **cond-mat**, 0706.0381 (2007).

[115] T. Ernst, "Many body effects in the transport of Bose-Einstein Condensates." Diplomarbeit, 2006.

[116] T. Köhler and K. Burnett, *Microscopic quantum dynamics approach to the dilute condensed Bose gas*, *Phys. Rev. A* **65**, 033601 (2002).

[117] N. Shnerb and M. Kaveh, *Non-Rayleigh statistics of waves in random systems*, *Phys. Rev. B* **43**, 1279–1282 (1991).

[118] M. C. W. van Rossum and T. M. Nieuwenhuizen, *Multiple scattering of classical waves: microscopy, mesoscopy, and diffusion*, *Rev. Mod. Phys.* **71**, 313–371 (1999).

[119] T. M. Nieuwenhuizen and M. C. W. van Rossum, *Intensity Distributions of Waves Transmitted through a Multiple Scattering Medium*, *Phys. Rev. Lett.* **74**, 2674–2677 (1995).

[120] E. Kogan and M. Kaveh, *Statistics of waves propagating in a random medium*, *Foundations of Physics* **26**, 679–690 (1996).

[121] E. Kogan, M. Kaveh, R. Baumgartner, and R. Berkovits, *Statistics of waves propagating in a random medium*, *Phys. Rev. B* **48**, 9404–9410 (1993).

[122] T. Ernst, T. Paul, and P. Schlagheck, *Transport of Bose-Einstein condensates beyond the Gross-Pitaevskii approach*, *in preparation*.

Wissenschaftliche Publikationen und Beiträge

Publikationen in Journalen

1. *Coherent Backscattering of Bose-Einstein Condensates in Two-Dimensional Disorder Potentials.*
M. Hartung, T. Wellens, C. A. Müller, K. Richter, and P. Schlagheck
Phys. Rev. Lett. **101**, 020603 (2008)

2. *Nonlinear transport of Bose-Einstein condensates through mesoscopic waveguides.*
T. Paul, M. Hartung, K. Richter, and P. Schlagheck
Phys. Rev. A **76**, 063605 (2007)

Beiträge zu Konferenzen

3. *Transport and decay of Bose-Einstein-Condensates in atomic quantum dot potentials.* (Posterpräsentation)
M. Hartung, T. Paul, K. Richter, and P. Schlagheck
DPG Frühjahrstagung, März 2006, Frankfurt

4. *Transport and decay of Bose-Einstein-Condensates in atomic quantum dot potentials.* (Posterpräsentation)
M. Hartung, T. Paul, K. Richter, and P. Schlagheck
At the Interface of Cold Atoms and Statistical Physics
Workshop, September 2006, Günzburg

5. *Transport of Bose-Einstein condensates through two-dimensional disorder potentials.*
(Vortrag)
M. Hartung, K. Richter, and P. Schlagheck
DPG Frühjahrstagung, März 2007, Düsseldorf

6. *Transport of Bose-Einstein condensates through two-dimensional disorder potentials.*
(Posterpräsentation)
M. Hartung, K. Richter, and P. Schlagheck
Quantum Gases
Workshop, Juli 2007, Paris

7. *Transport of Bose-Einstein condensates through two-dimensional disorder potentials.* (Vortrag)
M. Hartung, K. Richter, and P. Schlagheck
BECBS 07: Bose-Einstein Condensates and Coherent Backscattering
Workshop, September 2007, Thurnau

8. *Transport of Bose-Einstein condensates through two-dimensional disorder potentials.* (Vortrag)
M. Hartung, K. Richter, and P. Schlagheck
DPG Frühjahrstagung, März 2008, Darmstadt

9. *Coherent Backscattering of Bose-Einstein Condensates in Two-Dimensional Disorder Potentials.* (Vortrag)
M. Hartung, K. Richter, and P. Schlagheck
Scattering Systems with Complex Dynamics
Workshop, Oktober 2008, Regensburg

Acknowledgments

Mit den folgenden Worten möchte ich mich bei allen bedanken, die mich im Laufe der letzten Jahre begleitet haben und mir dabei den Rückhalt und das Vertrauen gegeben haben, das man braucht, um neue Konzepte auszuprobieren und um vieles in der Physik zu lernen, um die Ergebnisse in dieser Arbeit zu erhalten.
Zuallererst möchte ich mich natürlich bei PD Dr. Peter Schlagheck und Prof. Dr. Klaus Richter für die Betreuung der Promotion bedanken. In seiner kompetenten Weise lernte mir PD Dr. Peter Schlagheck wesentliche Techniken und gab mir viel Hintergrundwissen über kalte Atome weiter. Mit seinem Enthusiasmus spornte er mich während der ganzen Zeit an. Zusätzlich stand er mir in allen organisatorischen und finanziellen Fragen zur Seite, und half mir, einen Aufenthalt an der Université Pierre et Marie Curie in Paris zu verwirklichen. Neben diesem ist auf jeden Fall noch zu erwähnen, dass er immer Zeit für alle meine Fragen und Anliegen hatte. Weiterhin möchte ich mich bei Prof. Dr. Klaus Richter dafür bedanken, dass er es mir ermöglichte, diese Promotion an seinem Lehrstuhl durchzuführen und dass er mich in in jeder Hinsicht unterstützt hat.
Des weiteren will ich alle jetzigen und ehemaligen Mitglieder der Arbeitsgruppe Bose-Einstein condensate erwähnen, die - neben PD Dr. Peter Schlagheck - aus Dr. Tobias Paul, Timo Hartmann, Thomas Ernst und Boris Nowak besteht. Es war immer möglich, in einer freundlichen Atmosphäre und einer effektiven Weise mit einer Tasse Espresso und einem Stift Probleme zu lösen.
Nicht weniger fruchtbar waren die Diskussionen, die wir mit Physikern von externen Instituten führten. Als erstes will ich dazu Dr. Thomas Wellens und Prof. Dr. Cord Müller erwähnen, die analytische Berechnungen durchführten, die mit meinen Ergebnissen in Einklang waren, und wenn nicht, konnten die Schwierigkeiten doch ausgeräumt und erklärt werden. Des weiteren war es sehr interessant, mit Dr. Dominique Delande und Dr. Benoît Grémaud zu arbeiten, bei denen ich mich außerdem für die Möglichkeit

bedanken möchte, dass ich während eines Aufenthaltes an ihrem Institut an der Université Pierre et Marie Curie in Paris arbeiten durfte.
Unser Büro ist der Ort, an dem ich in den letzten Jahren viel Zeit verbracht habe. Da es nicht leicht ist, einen Raum mit denselben Personen täglich zu teilen, soll dies ein Kompliment an meine Kollegen im "Sysadmin-Büro" Dr. Michael Wimmer, Matthias Scheid und Timo Hartmann sein für die kollegiale Atmosphäre, die sowohl von Arbeit und Physik geprägt war, als auch viel Spaß und Diskussionen über das Leben beinhaltete. Für die gute Zusammenarbeit in allen EDV Fragen möchte ich mich auch bei Dr. Fritz Wünsch und bei Rudi Holzer bedanken.
Nicht zu vergessen ist natürlich Angela Reißer, die immer sehr hilfsbereit ist und den Überblick nicht verliert. Sie ist an erster Stelle dafür verantwortlich, dass der Zusammenhalt am Lehrstuhl in dieser Weise funktioniert und dass in der täglichen Runde sowohl physikalische als auch Alltagsrätsel diskutiert werden können.
Natürlich möchte ich mich besonders bei weiteren theoretischen Physikern für das Lösen von Alltagsproblemen mit Hilfe von vielen Tassen Kaffee bedanken: Dr. Christian Hagen, Dr. Dieter Hierl, Dr. Andreas Lassl und besonders Dr. Nikolaus Warkentin wurden Freunde, mit denen man die Physik als auch wichtige Probleme im Zusammenhang mit Computern diskutieren konnte. Letzterer verdient besonderen Dank für die Freundschaft, die sich seit dem gemeinsamen Studienbeginn aufbaute.
Zum Schluß möchte ich mich besonders bei meiner Mutter und bei meinen Brüdern bedanken, die mir durch ihre verlässliche Unterstützung während des gesamten Studiums mir stets den Rücken frei hielten. Ganz besonders möchte ich mich auch bei Mirjam bedanken, für all die ermutigenden Worte in den letzten Jahren. Vielen Dank, dass du mir auch in schwierigen Zeiten viel Kraft und Liebe gibst.

Für die finanzielle Unterstützung in den letzten Jahren möchte ich mich beim Graduiertenkolleg GRK 638, bei der DFG Forschergruppe 760, als auch bei der Universität Bayern e. V. bedanken.